# A PLASMA-WALL INTERACTION MODEL FOR THE EROSION OF MATERIALS UNDER ION BOMBARDMENT

A Dissertation
Presented to
The Academic Faculty

By

Hernán Javier Logarzo

In Partial Fulfillment
of the Requirements for the Degree
Doctor of Philosophy in the
School of Engineering
Department of Aerospace

Georgia Institute of Technology

May 2022

© Hernán Javier Logarzo 2022

# A PLASMA-WALL INTERACTION MODEL FOR THE EROSION OF MATERIALS UNDER ION BOMBARDMENT

Thesis committee:

Professor Julián J. Rímoli, Advisor
School of Aerospace Engineering
*Georgia Institute of Technology*

Professor George A. Kardomateas
School of Aerospace Engineering
*Georgia Institute of Technology*

Professor Mitchell L. R. Walker
School of Aerospace Engineering
*Georgia Institute of Technology*

Professor Claudio V. Di Leo
School of Aerospace Engineering
*Georgia Institute of Technology*

Dr. Michael R. Tupek
Principal engineer
*Computational Mechanics and Generative Design, PTC*

Date approved: April 7, 2022

To my wonderful wife Giselda and
my lovely children Bruno and Oriana for making it so fun to complete this thesis :)

# ACKNOWLEDGMENTS

I would like to express special thanks to my advisor and mentor, Prof. Julián Rímoli. Thank you for giving me the opportunity to join your group. From our very first phone conversation in which you told me about the research plan, the tremendous help during onboarding and throughout these years, I appreciate everything you have done for me. Your expertise in the field of solid mechanics and your passion for coding helped me thrive and grow in your group. Thank you for allowing me to be part of the STEM summer camps where we showed high-school students that engineering is fun, and for giving me the chance to be a teaching assistant in solid mechanics. I am glad that I got the chance to work side by side with you on a project for which we left our mark at the Georgia Institute of Technology: the Koan sculpture placed on campus. Similarly, I would like to thank Dr. Eduardo Dvorkin for introducing me to the foundations of computational mechanics and to my undergraduate mentors, Prof. Ana Scarabino, Prof. Martin Idiart and Dr. Marcos Actis from Universidad Nacional de La Plata for their constant mentorship.

I would also like to express my gratitude to the members of my thesis committee, Prof. Di Leo, Prof. Kardomateas, Prof. Walker and Dr. Tupek for their insight, guidance and participation in my examination. Their ideas and suggestions are reflected in the outcome of this work.

I am thankful for my friends at Gatech. From JB who helped me adapt to life in a new country during my first semester, to Amir, Daniel, Donald, Julie, and Mohit for making the lab a great place to work. Thank you guys for the support in those moments of uncertainty and anxiety, and thank you for those nights of extremely weird board games or dinners. Special thanks go to my buddies Aarohi and Ruthvik C for walking this path side-by-side, for being great friends and supportive; also to Kip for helping me while learning Python and for teaching me some American culture. Being with y'all these years showed me new cultures, new ideas, new points of view for which I will always be grateful. Similarly, I would like to thank my Argentinean “friendmily” for making it easier not to miss home.

I want to thank my family: my parents, Silvia and Osvaldo, and sister, Vini. To my parents, the love and values you gave me led me to accomplish my goals. I appreciate your understanding, support, and encouragement to pursue this adventure so far from home. Thank you, dad, for teaching me the beauty of airplanes since I was a toddler that definitely planted a seed to pursue aeronautical engineering. Thank you, mom, for trying to make me a medical doctor (which you almost succeeded), and thank you both for giving me wings and showing me that everything can be achieved.

Last and more important, I wanted to thank my wife Giselda for her unconditional love and incredible support over the last eleven years of my life. I would definitely not be here without you. Thank you for everything you did, so I could focus on studying and working towards this achievement. You have always provided me with emotional balance and were the one down to earth to make the tough calls, so I believe that this work also belongs to you. Needless to say, I am deeply grateful for the family we have formed with our little monsters, Bruno and Oriana, who became our most beautiful and precious gift. To my kids, you are too young now to understand, but being your dad is the most joyful job I would ever have. Y’all are simply the best.

## TABLE OF CONTENTS

**Acknowledgments** . . . . . . . . . . . . . . . . . . . . . . . . . . . . . iv

**List of Tables** . . . . . . . . . . . . . . . . . . . . . . . . . . . . . . ix

**List of Figures** . . . . . . . . . . . . . . . . . . . . . . . . . . . . . x

**Summary** . . . . . . . . . . . . . . . . . . . . . . . . . . . . . . . . . xv

**Chapter 1: Introduction** . . . . . . . . . . . . . . . . . . . . . . . . . 1

1.1 Hall effect thrusters . . . . . . . . . . . . . . . . . . . . . . . . 1

1.2 Motivation and State-of-the-Art . . . . . . . . . . . . . . . . . . . 2

1.3 Scope and Organization . . . . . . . . . . . . . . . . . . . . . . . 6

**Chapter 2: Plasma-wall interaction model** . . . . . . . . . . . . . . . . 8

2.1 Overview of the probability-based model . . . . . . . . . . . . . . . 8

2.2 Plasma-surface interaction . . . . . . . . . . . . . . . . . . . . . 10

2.2.1 Data from Plasma full simulation . . . . . . . . . . . . . . . . 10

2.2.2 Geometric parameters . . . . . . . . . . . . . . . . . . . . . . 12

2.2.3 Mesh independent erosion rate . . . . . . . . . . . . . . . . . . 22

2.2.4 Element removal criterion . . . . . . . . . . . . . . . . . . . . 24

2.3 Finite Element Model . . . . . . . . . . . . . . . . . . . . . . . . 32

2.3.1 Thermal model . . . . . . . . . . . . . . . . . . . . . . . . . . 32
2.3.2 Mechanical model . . . . . . . . . . . . . . . . . . . . . . . . 35
2.3.3 Power deposition - Heat flux to the wall . . . . . . . . . . . . . . . 37
2.3.4 Coupling of the Thermo-elastic model . . . . . . . . . . . . . . . . 39

**Chapter 3: Material Models . . . . . . . . . . . . . . . . . . . . . . . . 41**

3.1 Introduction . . . . . . . . . . . . . . . . . . . . . . . . . . . . 41
3.2 Elastic material model . . . . . . . . . . . . . . . . . . . . . . . . 41
3.3 Deshpande-Evans damage material model . . . . . . . . . . . . . . . . 42
3.4 Discussion - Scope and limitations of the elastic and DE constitutive models 48
3.5 Data-driven material model . . . . . . . . . . . . . . . . . . . . . . 54
3.5.1 Homogenizing inelastic behavior via Machine Learning . . . . . . . 55
3.5.2 Training the machine learning model . . . . . . . . . . . . . . . . . 64
3.5.3 SCL implementation into a FE solver . . . . . . . . . . . . . . . . 68
3.5.4 Summary of the homogenization technique with ML . . . . . . . . 70

**Chapter 4: Results . . . . . . . . . . . . . . . . . . . . . . . . . . . . 71**

4.1 Application to boron nitride . . . . . . . . . . . . . . . . . . . . . 71
4.1.1 Setup . . . . . . . . . . . . . . . . . . . . . . . . . . . . . . . 72
4.1.2 Results of the erosion process simulations . . . . . . . . . . . . . 76
4.2 Application to fused silica . . . . . . . . . . . . . . . . . . . . . . 83
4.2.1 Setup . . . . . . . . . . . . . . . . . . . . . . . . . . . . . . . 84
4.2.2 Results of the erosion process simulations . . . . . . . . . . . . . 92
4.3 Summary of results . . . . . . . . . . . . . . . . . . . . . . . . . 99

**Chapter 5: Conclusions** . . . . . . . . . . . . . . . . . . . . . . . . . . . . . . 103

5.1 Summary and conclusions . . . . . . . . . . . . . . . . . . . . . . . . . . 103

5.2 Contributions . . . . . . . . . . . . . . . . . . . . . . . . . . . . . . . 105

5.3 Future work . . . . . . . . . . . . . . . . . . . . . . . . . . . . . . . 106

**Appendices** . . . . . . . . . . . . . . . . . . . . . . . . . . . . . . . . 108

**Chapter A: Strain energy density at failure** . . . . . . . . . . . . . . . . . . . . 109

**Chapter B: Microcracks coefficients** . . . . . . . . . . . . . . . . . . . . . . 113

**References** . . . . . . . . . . . . . . . . . . . . . . . . . . . . . . . . 115

# LIST OF TABLES

2.1 Regimes definition as a function of the size factor $h$. . . . . . . . . . . . . . . 17

2.2 Sputtering yield constants used in this chapter, [21]. . . . . . . . . . . . . . . 27

2.3 Integration points for Gaussian quadrature rule in power density calculation. 38

3.1 Alumina properties. . . . . . . . . . . . . . . . . . . . . . . . . . . . . 49

4.1 General parameters for the erosion process simulation. . . . . . . . . . . . 73

4.2 Sputtering yield constants used for fused silica in this chapter, [21, 12]. . . . 84

4.3 Fused silica properties [65, 66]. . . . . . . . . . . . . . . . . . . . . . . . 85

# LIST OF FIGURES

1.1 Hall effect thruster schematics. The electrons (yellow) emitted from the cathode collide with the neutrons (white) due to the magnetic field (B) and form ions (blue) that are accelerated and expelled from the discharge chamber by the electric field (E) generating thrust [1, 2]. . . . . . . . . . . . . 2

1.2 Erosion ridges in the ceramic walls after being exposed to plasma for long periods of time. . . . . . . . . . . . . . . . . . . . . . . . . . . . 3

2.1 Overview and flowchart of the plasma-wall interaction model . . . . . . . . 9

2.2 Ions current density and Energy Distribution Function obtained at the trenches and peaks [29] . . . . . . . . . . . . . . . . . . . . . . . . . . . 11

2.3 Visibility factor definition (a) surface and ion beam normal vectors, (b) orientation of impacting ions. . . . . . . . . . . . . . . . . . . . . . . . 13

2.4 Size factor parameters, Debye length $\lambda_D$, wavelength $L$, and amplitude $A$. . 15

2.5 Filtering of the surface profile from FE mesh for FFT to obtain the dominant wavelength $L$ and amplitude $A$ per each erosion step.(a) The transition of the surface profile from the raw FE mesh to a smoother curve for FFT processing, (b) FFT and criteria to define the dominant length $L$ and amplitude $A$ from the moving averaging. . . . . . . . . . . . . . . . . . . . . . . 16

2.6 Interpolation surface . . . . . . . . . . . . . . . . . . . . . . . . . . . 18

2.7 Sampling of ion energy $E_F$ and $E_G$ for the references bounds at the “front” and “groove”, respectively; (a) sampling from an ion energy probability distribution from its cumulative distribution, (b) the recovered ion energy distribution after sampling 200 times. . . . . . . . . . . . . . . . . . . . . . . 19

2.8 Calibration of the size factor. Geometry and fitted curve in the upper subfigure and FFT of the fitted curve in the lower subfigure. . . . . . . . . . . 20

2.9 Calibration of random variables $a_1$ and $a_2$. (a) The visibility factor is evaluated at the center point of the groove, $v^*$, and the possible functions and fitting parameters to determine the variables. (b) The corresponding ion energy distributions obtained with the calibrated interpolating function of Equation 2.10. . . . . . . . . . . . . . . . . . . . . . . . . . . . . . . . 21

2.10 Schematics for the erosion rate estimation. . . . . . . . . . . . . . . . . . . 23

2.11 Schematics for the joint probability function definition. $J_0(P)$ and $J_1(P)$ are the bounds of the joint probability function when the strain energy ratio is $D = 0$ and $D = 1$. For a given value of strain energy ratio $D$ and power to wall $P$, the joint probability distribution $J(P, D)$ is obtained from an exponential interpolation. . . . . . . . . . . . . . . . . . . . . . . . . . . 25

2.12 Probability function when strain energy ratio is $D_0$, $J_0(P)$ normalized with the element size as a function of the power from the ions $P$ against the wall. 29

2.13 (a) Joint probability distribution for three different meshes, M1, M2, and M4. (b) Joint probability distribution for M1 and three different time increments. . . . . . . . . . . . . . . . . . . . . . . . . . . . . . . . . . . 32

2.14 Diagram for the Finite Element Model of the thermo-mechanical problem. . 34

2.15 Power deposition on frontier elements for FE analysis. . . . . . . . . . . . 39

2.16 Flowchart of the quasi-static analysis for thermo-mechanical problems. . . . 39

3.1 Wing microcracks distribution in a cracked solid [34]. . . . . . . . . . . . . 43

3.2 RVE of the microstructure with the cohesive element path for crack growth, the cracks location and the FE mesh. . . . . . . . . . . . . . . . . . . . . 50

3.3 Bi-linear traction separation law. . . . . . . . . . . . . . . . . . . . . . . . 51

3.4 Comparison of equivalent stresses from numerical homogenization of the RVE and the inelastic ceramic constitutive law defined in section 3.3 for (a) uniaxial stress case, (b) uniaxial strain case and (c) pure shear case. . . . . . 52

3.5 (a) Macro-strains for a Gaussian Process. The figure to the left shows a case without shear strain ($\epsilon_{12} = 0$), whereas the full strain history is shown to the right. (b) Effective equivalent stress as a function of the load increment for the no shear case (left) and full history (right). The three models are (1) an elastic material model, (2) the FE of the RVE of the microstructure, and (3) the inelastic constitutive law from section 3.3. . . . . . . . . . . . . . . 53

3.6 Overview of the proposed approach to build a generic data-driven material model. . . . . . . . . . . . . . . . . . . . . . . . . . . . . . . . . . 58

3.7 Generation of strain histories (sequences) for the training set. . . . . . . . . 61

3.8 Joint distribution for principal strains, as in [28]. . . . . . . . . . . . . . . . 62

3.9 Machine learning model schematics. The input layer corresponds to three nodes, one for each strain component, $\epsilon_{11}, \epsilon_{22}, \epsilon_{12}$; the hidden layers are LSTM layers, and the output layer has three units, one for each stress output, $\sigma_{11}, \sigma_{22}, \sigma_{12}$. . . . . . . . . . . . . . . . . . . . . . . . . . . 65

3.10 Transfer learning concept. (a) Schematics for the MSE calculation, (b) Trainable parameters (1) using only MSE, (2) using the combined loss. . . . 67

3.11 SCL implementation in a quasi-static boundary value problem. (a) diagram of possible solutions during the iterative process, (b) flowchart of the overall solution scheme with SCL implementation. . . . . . . . . . . . . . . . . 69

4.1 Schematics for the thermal and mechanical boundary conditions of the thermo-elastic model. . . . . . . . . . . . . . . . . . . . . . . . . . . 72

4.2 Ion energy distribution $E_F$ and $E_G$ for reference bounds to use in the erosion process simulation. . . . . . . . . . . . . . . . . . . . . . . . . . 74

4.3 Time increment bounds for the probabilistic approach. . . . . . . . . . . . 75

4.4 Joint probability distribution for the case study. . . . . . . . . . . . . . . . 76

4.5 Surface evolution for the sputtering (top), the elastic (center) and the inelastic (bottom) models at (a) approx. 20 mW/mm$^2$, (b) 35 mW/mm$^2$ and (c) 50 mW/mm$^2$ . . . . . . . . . . . . . . . . . . . . . . . . . . . 77

4.6 Wavelength, roughness and peak-to-peak at (a) approx. 20 mW/mm$^2$, (b) 35 mW/mm$^2$ and (c) 50 mW/mm$^2$ . . . . . . . . . . . . . . . . . . . . 79

4.7 Estimated erosion rate for boron nitride as a function of the heat flow to the wall at each power level. . . . . . . . . . . . . . . . . . . . . . . . . 81

4.8 Estimated (a) stresses and (b) temperatures as a function of the heat flow to the wall at each power level. . . . . . . . . . . . . . . . . . . . . . . 82

4.9 (a) Roughness and (b) peak to valley values, as a function of the resulting mean stress of the specimen $\sigma$ for the sputtering (blue circles), the elastic (orange triangles), and inelastic (green squares) models. . . . . . . . . . . . 82

4.10 Surface features as a function of the mean stress of the specimen, $\sigma$. . . . . 83

4.11 RVE of the fused silica microstructure with the cohesive element path for crack growth, the cracks location and the FE mesh. . . . . . . . . . . . . . 86

4.12 Distribution of principal strains for the fused silica RVE. . . . . . . . . . . 86

4.13 Evaluation of several architectures with unseen cases. . . . . . . . . . . . . 87

4.14 Comparison between real (blue) and predicted (orange) behavior of the microstructure for test (unseen) cases for strain history labeled 1030. . . . . . 88

4.15 Comparison between real (blue) and predicted (orange) behavior of the microstructure for test (unseen) cases for strain history labeled 1079. . . . . . 89

4.16 Comparison between real (blue) and predicted (orange) behavior of the microstructure for test (unseen) cases for strain history labeled 1102. . . . . . 90

4.17 Comparison between real (blue) and predicted (orange) behavior of the microstructure for test (unseen) cases for strain history labeled 1103 . . . . . . 91

4.18 Temperature (K) and stress (S, MPa) fields for the erosion process at approximately 36 mW/mm$^2$. . . . . . . . . . . . . . . . . . . . . . . . . . . 93

4.19 Temperature (K) and stress (S, MPa) fields for the erosion process at approximately 50 mW/mm$^2$. . . . . . . . . . . . . . . . . . . . . . . . . . . 94

4.20 Temperature (K) and stress (S, MPa) fields for the erosion process at approximately 90 mW/mm$^2$. . . . . . . . . . . . . . . . . . . . . . . . . . . 95

4.21 Erosion rate for fused silica as a function of applied power. . . . . . . . . 97

4.22 Estimated (a) stresses and (b) temperatures as a function of the heat flow to the wall at each power level for fused silica. . . . . . . . . . . . . . . . . 97

4.23 (a) Roughness and (b) peak-to-valley values, as a function of the heat flow to the wall at each power level for fused silica. . . . . . . . . . . . . . . . . 98

4.24 Roughness and strain energy density evolution for the sputtering, elastic, and data-driven model for three power levels. . . . . . . . . . . . . . . . . 100

4.25 Schematics of the unstable erosion process. . . . . . . . . . . . . . . . . . . 101

4.26 Evolution and comparison of the recession of the wall for the sputtering case (blue) and the microstructure-based material (orange) where the erosion ridges would limit the lifetime of a device for (a) low, (b) medium, and (c) high powers. . . . . . . . . . . . . . . . . . . . . . . . . . . . . . . . 102

A.1 Schematics for the thermal and mechanical boundary conditions of the thermo-elastic model. . . . . . . . . . . . . . . . . . . . . . . . . . . . . 109

# SUMMARY

Understanding the evolution and behavior of materials exposed to plasma is critical for the design of future electric propulsion devices. As ions are ejected from the device generating thrust, they also impact the ceramic walls. This induces wall erosion, ultimately exposing the magnetic circuit leading to malfunction and failure of the device. This problem is only going to be amplified as the field moves towards high power density devices. There are several models that try to predict this effect by accounting for material sputtering. However, they cannot predict the millimeter-scale surface features that develop after prolonged exposure. In this work, we address this issue by introducing a plasma-material interaction model able to capture the evolution of surface features at the macroscopic scale on materials exposed to plasma over a long period of time. The model is based on (i) data from plasma dynamics simulations, (ii) a probability model of erosion, (iii) geometric effects to account for shadowing effects and feature size and (iv) a continuum finite element model for the thermo-mechanical response of the dielectric walls that uses machine learning to account for the complex response of the material.

Results show that the model is able to reproduce not only the mean erosion rate but also the macroscopic anomalous ridges that appear after prolonged exposure. Furthermore, it highlights the need to account for complex thermo-mechanical material behavior to be able to explain such features.

# CHAPTER 1

# INTRODUCTION

## 1.1 Hall effect thrusters

The Hall effect thrusters (HET) consist of a cylindrical ceramic channel with an anode, a magnetic circuit that generates a magnetic field, and a cathode (usually located outside the channel). An external power produces an electric field. The interaction between the magnetic and electric field forces provoke the electrons emitted from the cathode to collide with a neutral propellant (in general xenon) which is fed through the anode. This process produces ions which are then accelerated through the channel by the electric field, as shown schematically in Figure 1.1 [1, 2]. The insulating walls, as illustrated in Figure 1.1, are manufactured from dielectric materials such as boron nitride (BN), or borosil (BN-$SiO_2$). These materials are usually chosen because of the low sputtering yield (susceptibility of erosion), high strength, thermal properties, and low secondary electron emission to guarantee proper functioning of the thruster [1, 3].

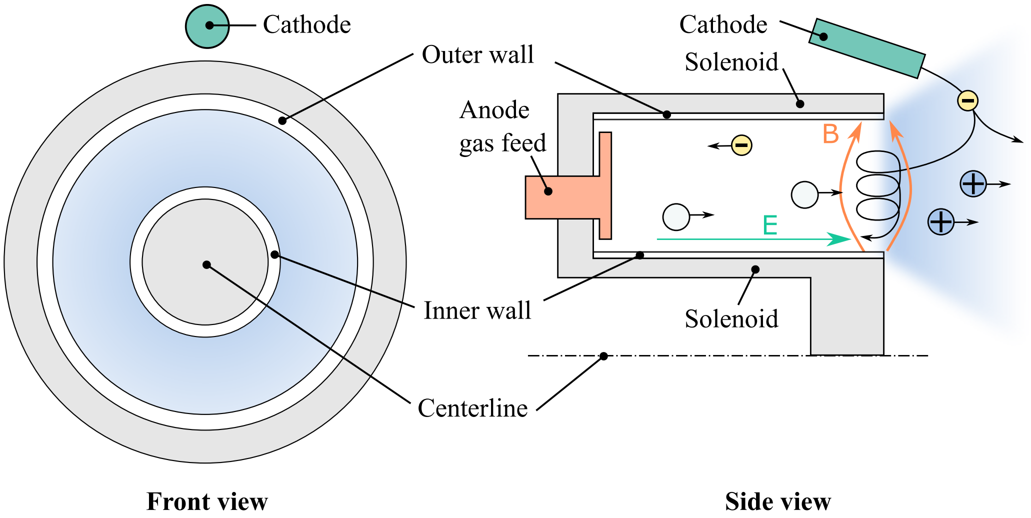

Figure 1.1: Hall effect thruster schematics. The electrons (yellow) emitted from the cathode collide with the neutrons (white) due to the magnetic field (B) and form ions (blue) that are accelerated and expelled from the discharge chamber by the electric field (E) generating thrust [1, 2].

Understanding the evolution and behavior of materials exposed to plasma is critical for the design of future electric propulsion devices. As the ions are ejected from the device generating thrust, they also impact the ceramic walls. This induces wall erosion, ultimately exposing the magnetic circuit leading to malfunction and failure of the device. This phenomenon has been the limiting factor in the HET lifetime. Up to date, the only reliable assessment to quantify the lifetime of the devices is to submit a fully operational thruster to qualification tests [4, 5, 6, 7] which represents high costs during the development of new devices. Hence, it is necessary to have fundamental models with predicting capabilities in order to reduce developing iterations and costs.

## 1.2 Motivation and State-of-the-Art

Throughout the years, many models have been developed to account for the erosion of material under ion bombardment. The sputtering yield is the main characteristic to understand this process [8, 9]. These models motivated many experiments that have been conducted to understand the nature of these mechanisms [10]. Up to date, the erosion of material is usually measured by several means. For example, mass loss measurements, collection of sputtered material using a quartz crystal microbalance (QCM), or empirically using a stationary plasma thruster (SPT)-type laboratory HET where the erosion rate is studied for different materials exposed to plasma [11, 12, 13], to name a few. The material used in these measurements includes boron nitride (BN), quartz, Kapton among others, since they are widely used in HET. On the other hand, numerical simulations using HPHall-2 [14] have been conducted to estimate the erosion process of the SPT-100 Hall thruster [15] using the same sputtering mechanisms. These methods provide a good estimate of the overall average erosion. However, certain features that develop after very long periods of life testing are still not well understood. Probably the most important is the appearance of grooves (peaks and valleys) that form during qualification tests, as observed in the Russian SPT-100, the BPT-4000, and PPS-1350G devices [4, 5, 6, 7]. It is usually defined as "anomalous erosion" which is characterized by periodic patterns [16]. Figure 1.2 shows schematically the erosion ridges that form after plasma exposure on a HET thruster.

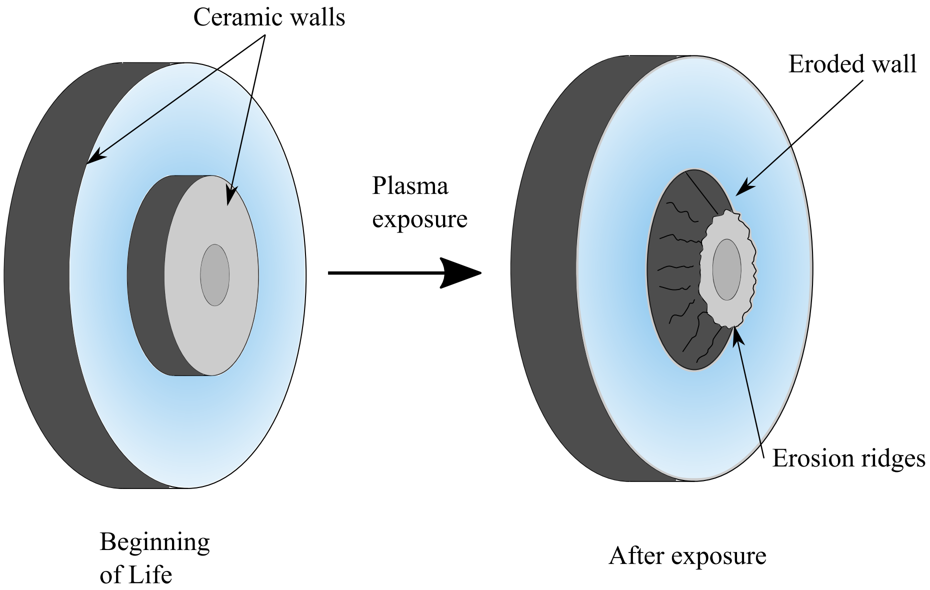

Figure 1.2: Erosion ridges in the ceramic walls after being exposed to plasma for long periods of time.

On a different line of investigation, several research efforts have been conducted to demonstrate that the incident ion power density to the wall (heat flux) is proportional to the local erosion rate [17]. Hence, different efforts have been made to measure or quantify the energy flux from the discharge plasma to the walls. For instance, the use of thermal imaging and empirical thermal models to characterize the evolution of the wall temperature where the power lost to walls was found to be between 0.1 and 2 W/cm$^2$ in different devices using boron nitride and quartz (BN-SiO$_2$) [18]. Martinez *et al.* [19] conducted an experimental investigation on a 4.5-kW T-140 HET by using thermocouples to understand the influence of global parameters (such as discharge power, voltage, current, and mass flow) upon the wall temperatures, power lost to walls, and radiation to the environment. They concluded that up to 13% of the discharge power was lost to the walls. In this case, the wall material is M26-grade boron nitride.

In order to isolate the effect of different factors that are involved in the erosion process, recent research tends to create controlled experiments. One factor is the material composition or microstructure. Burton *et al.* [20] studied how the different constituents of the microstructure affect the sputtering and control the erosion process. The authors analyzed the microstructure of the wall material (M26 grade of BN) of the U.S. AirForce Research Laboratory/University of Michigan (AFRL/UM) P5 thruster after being operated for about 2,000 hours. They found three main regions depending on the erosion pattern. Each region was analyzed, and several striations and microcracks were found in the high and middle eroded areas. Through a Finite Element (FE) model, the authors concluded that the creation of microcracks was due to anisotropic thermal expansion of the constituents of the ceramic that generated stress concentration. Also, they suggested that these microcracks could favor BN grain detachment exposing silica (quartz) which has a different sputtering rate, thus, explaining the erosion patterns. Following this work, Schinder *et al.* [21] incorporated shadowing effects, a heterogeneous material model, and a 3D domain to compare with the experimental results of the P5 thruster. The authors found that atomic sputtering does not predict well in highly eroded regions due to limitations regarding (a) the lack of material model, (b) the amount of data in the low discharge voltages, and (c) the 2D axisymmetric space. They concluded that the ejection of material is a plausible mechanism to explain the overall creation of surface features such as ridges. As a continuation of the work in [20], Brown *et al.* [22] studied the role of the microcracks in wall erosion. They created a thermal cycle similar to what the ceramic walls are exposed to and compared the erosion rate and patterns of these specimens against control (no thermal cycling) samples, but they did not find a clear connection with the erosion process. In addition, Schinder *et al.* [23] studied the erosion process under mechanical stress using a simplified thermal model based on the work by Martinez *et al.* [19] that accounts for thermal stresses in the wall materials given the high temperatures attained during operation. They conducted a series of experiments with different specimens under mechanical compressive stress to find a correlation between the abnormal ridges found after several hours of operation. The study was based on the analysis of surface-roughness due to stress during chemical etching, where it had been found a correlation between the strain energy density of the surface and the formation of patterns [24].

Considering that the state-of-the-art numerical methodologies developed to capture the erosion ridges are computationally expensive, several simplifications are made [21]. For example, only a single ion bombardment incident angle can be simulated at a time, the specimen under study is limited to a surface of a few hundreds of microns and the simulation for only a few hours time span. Thus, erosion depth of only some hundreds of microns is attained. On the other hand, experimentally based research conducted to find the relation between mechanical stresses is also restricted to a few hours considering the limitations of the laboratory setup [23]. Therefore, the formation and development of the anomalous ridges and their relation to material behavior such as stresses or microcracks, as pointed in [20], cannot be captured as they are found after long exposures. Moreover, the mathematical models that investigate the evolution of periodic patterns are focused on the etching process by ion bombardment. Thus, only covering the nano or micro-scales and for small perturbations [9, 25, 26]. A comprehensive review work by Brown *et al.* [2] presents the efforts in understanding the erosion process in HET as well as several concepts to reduce it. In addition, the review work by Chan *et al.* provides a thorough description of the mathematical models in the nanoscale [27].

## 1.3 Scope and Organization

The goal of this work is to contribute to a better understanding of the erosion process at the macro-scale and for long time exposure by focusing on creating a plasma-wall interaction model enhanced by microstructure mechanical behavior that leverages the state-of-the-art sputtering models to date and material modeling. Based on previous studies, the formation of erosion ridges cannot be reproduced with the sputtering models alone. Hence, the hypothesis of this work is that the formation of features is related to an instability the happens in the material and it is related to the strain energy of the surface.

The plasma-wall interaction model is presented in chapter 2 where the key concepts and analytical formulations are described. The proposed model comprises data from plasma dynamics simulations and a detailed finite element (FE) model of a ceramic microstructure. The interaction between the ion energy deposited and the wall material is based on (i) data from plasma dynamics simulations, (ii) the probability of wall surface to erosion, (iii) geometric effects to account for shadowing effects and feature size, and (iv) a continuum FE model of the dielectric walls. The interaction model is described in section 2.2 and thermoelastic continuum model is discussed in section 2.3. The motivation to use a probabilistic approach relies on the fact that the ion energy (thus the power) to the wall is stochastic. Therefore, the general trends of the results are shown by analyzing the statistics from several simulations.

The need to understand the microstructure behavior and the capability to reproduce it with surrogate models opens the door for the homogenization of a microstructure behavior. Homogenizing the constitutive response of materials with nonlinear and history-dependent behavior at the microscale is particularly challenging. In this case, the only option is generally to homogenize numerically via concurrent multiscale models (CMMs), as pointed out in [28]. Unfortunately, these methods are not practical as their computational cost becomes prohibitive for engineering-scale applications. In chapter 3, an alternative formulation to CMMs that leverage state-of-the-art micromechanical modeling and advanced machine learning (ML) techniques is presented. The resulting homogenized constitutive law with this methodology is named *Smart Constitutive Laws* (SCLs).

The results of the plasma-wall interaction model are presented in chapter 4 with a case study for boron nitride in section 4.1 where a simple elastic and inelastic material behavior are considered. Then, in the second part of the chapter (section 4.2), a fused silica microstructure is homogenized using the technique developed in chapter 3 and the resulting material behavior is implemented in the plasma-wall interaction model.

Finally, in chapter 5 we summarize the main findings and provide concluding remarks. Throughout the manuscript, we use the indicial notation (unless otherwise noted for simplicity) where the summation is performed over repeated indices.

# CHAPTER 2

# PLASMA-WALL INTERACTION MODEL

## 2.1 Overview of the probability-based model

Consider a material exposed to ionized gas, *i.e.*, plasma, for which the erosion rate and evolution of surface patterns need to be estimated. The model presented in this work predicts this evolution by combining data obtained from a high fidelity plasma dynamics simulation with a Finite Element (FE) model of the ceramic walls that accounts for the material behavior and an erosion probability distribution for each point of the surface of the material. For a given state of the exposed wall surface, the procedure to estimate its evolution involves three main stages: the *preprocessing*, the *FE simulation* and *surface update*. The overall flowchart of the plasma-wall interaction model is depicted in Figure 2.1.

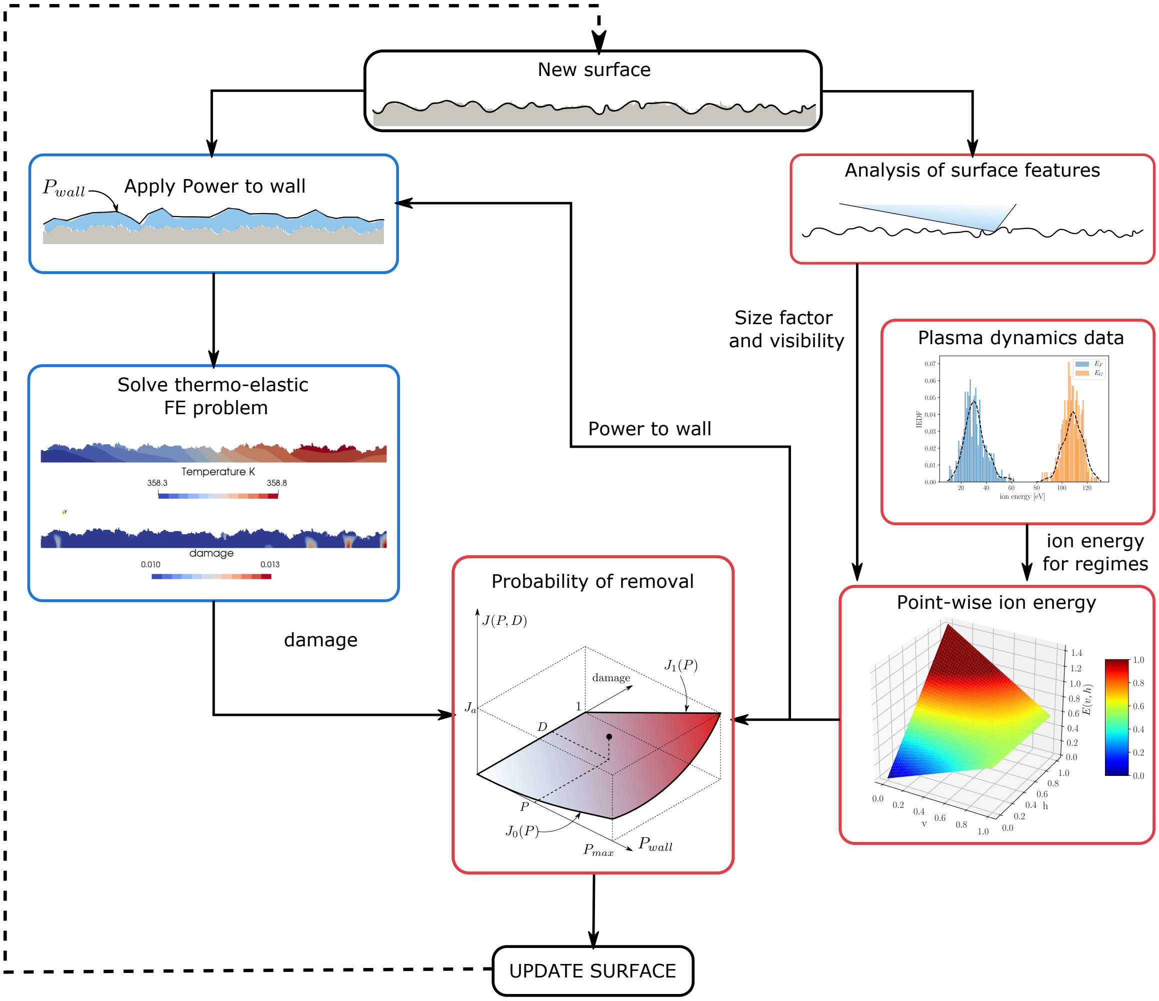
New surface
$P_{wall}$
Apply Power to wall
Analysis of surface features
Size factor
and visibility
Plasma dynamics data
IEDF
ion energy [eV]
$E_I$
$E_{II}$
Solve thermo-elastic
FE problem
Temperature K
358.3
358.8
damage
0.010
0.013
Power to wall
ion energy
for regimes
damage
Probability of removal
$J(P, D)$
damage
$J_1(P)$
$J_a$
1
$D$
$P$
$J_0(P)$
$P_{max}$
$P_{wall}$
Point-wise ion energy
$E(v, h)$
v
h
UPDATE SURFACE

Figure 2.1: Overview and flowchart of the plasma-wall interaction model

In the preprocessing stage, an analysis of the surface features, *e.g.* dominant wavelength and shadowing effects, is performed with the aid of two novel parameters, namely the *visibility* and *size* factors, respectively.

These parameters are combined with the ion energy distribution from a high fidelity plasma simulation [29] to define a *point-wise ion energy interpolation function* as schematically shown in the right-hand side of Figure 2.1. From this function, the power to wall the $P_{wall}$ can be calculated from the ions impacting the material. These geometric parameters are described in subsection 2.2.2.

In the FE simulation stage, the heat transfer problem is solved using the heat flux from the ions ($P_{wall}$) and radiation boundary conditions. Secondly, the mechanical problem is solved for the stresses and strain energy density considering the thermal strains obtained from the heat transfer analysis as depicted in the left-hand side of Figure 2.1. The models for the thermal and mechanical FE simulations are described in detail in section 2.3.

In the surface update stage, the strain energy is combined with the power from the ions at each point of the surface, and a probability of removal $J(P, D)$ is calculated as explained in subsection 2.2.4. This probability is used to determine the likelihood of each element on the surface to be removed, which is then used to “update the surface” as shown in Figure 2.1.

## 2.2 Plasma-surface interaction

Ideally, one would couple a full plasma-dynamics model with the FE of the ceramic wall. In this way, the surface of the wall would be the boundary condition for the plasma simulation, for which the ion energy distribution would be obtained. The ion energy would then be transformed into heat flux to solve the thermo-mechanical model of the ceramic wall. After the wall is eroded, (considering the heat flux and its current strain energy), it would change the boundary conditions for the plasma simulation leading to a complete new ion energy deposition. However, performing this multi-physics analysis is computationally expensive. Therefore, one of the goals of the method is to be able to interpolate known ion energy data from certain boundary conditions to each surface point as it evolves in time. In this section, we develop all the parameters that we use to perform this task.

### 2.2.1 Data from Plasma full simulation

In the plasma side, the power to the wall due to ions, $P_{wall}$, is calculated as the product of the ions current $j_{ion}$ and energy distribution $E_{ion}$,

$$P_{wall} = j_{\text{ion}} E_{\text{ion}} \tag{2.1}$$

As pointed out in the introduction, recent studies showed that the ion energy distribution on the wall is higher in the valleys of the evolving eroded surface than the values at the peaks when these features are in the same order of magnitude as the Debye length [29]. A similar concept had been studied in the early 80s, where it had been found that valleys would erode faster given the amount of energy deposition in contrast to peaks [9, 25]. However, it was applied to small perturbations in the nano-scale. In work by Schweigert *et al.* [29], the authors observed the energy distribution and current density of the ions at a simplified surface topology consisting of a regular pattern of step-like functions as shown in Figure 2.2.

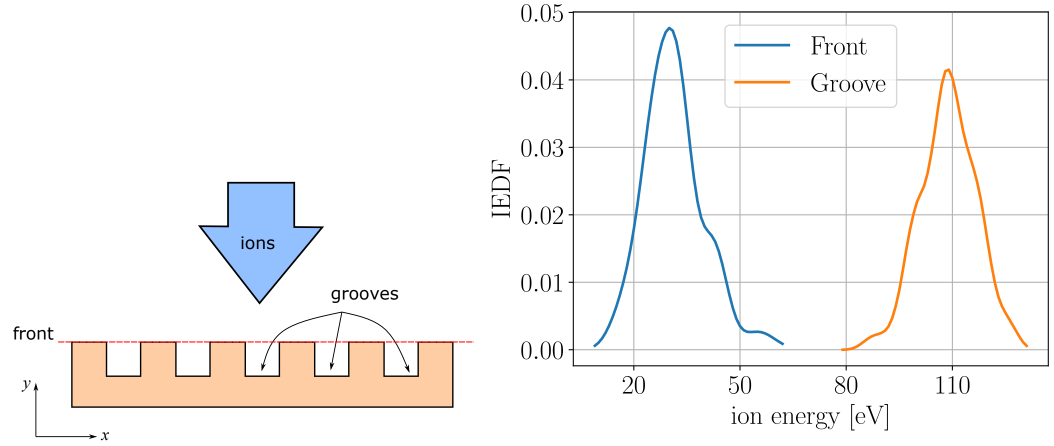

(a) Grooved specimen

(b) Ion energy distribution

Figure 2.2: Ions current density and Energy Distribution Function obtained at the trenches and peaks [29]

As it can be seen from the figure, there is more energy deposited at the grooves of the specimen than at the front line of it. This, naturally produces more heat flux to these zones leading to a greater temperature gradient and ultimately, stress concentrations.

Two considerations are worth noticing here. First, as it can be seen from Equation 2.1, the power is a random variable that depends on the random ion energy $E_{\text{ion}}$. Second, this equation is applied point-wise at each integration point on the surface. In other words, the power distribution at a given erosion step varies at each point of the surface.

### 2.2.2 Geometric parameters

The information of the ion energy distribution is used to create different regimes considering the surface topology as it evolves during the erosion process with two parameters: (1) the *visibility factor*, and (2) the *size factor*. The former accounts for shadowing effects that determine how much energy each point of the surface receives, and the latter is a non-dimensional parameter that compares how the overall features, *e.g.*, the dominant wavelength and amplitude of the surface's profile, compare to the Debye length of the plasma. Thus, at each stage of the erosion process, the model estimates how much energy is exerted at each surface point, considering an *interpolation scheme* of the ion energies from Figure 2.2. In this section, the two parameters and the interpolation scheme are discussed in more detail.

*Visibility factor*

At a given stage in the erosion process, let us define the normal vector to the surface at point $S_i$ as $\mathbf{n}$, and the ray vector between the $j$-th ion point, $\mathbf{I_j}$, and $\mathbf{S_i}$ as $\mathbf{n_1}$, as shown in Figure 2.3(a). Firstly, $\mathbf{n}$ is projected onto $\mathbf{n_1}$,

$$P(\theta) = \mathbf{n} \cdot \mathbf{n_1} = \mathbf{n} \cdot \frac{\mathbf{I_j} - \mathbf{S_i}}{||\mathbf{I_j} - \mathbf{S_i}||_2} = \mathbf{n} \cdot (\cos\theta \mathbf{e_1} + \sin\theta \mathbf{e_2}) \tag{2.2}$$

where $P(\theta)$ represents the projection of the $j$-th ion source, $\mathbf{I_j}$, onto the $i$-th surface point, $\mathbf{S_i}$.

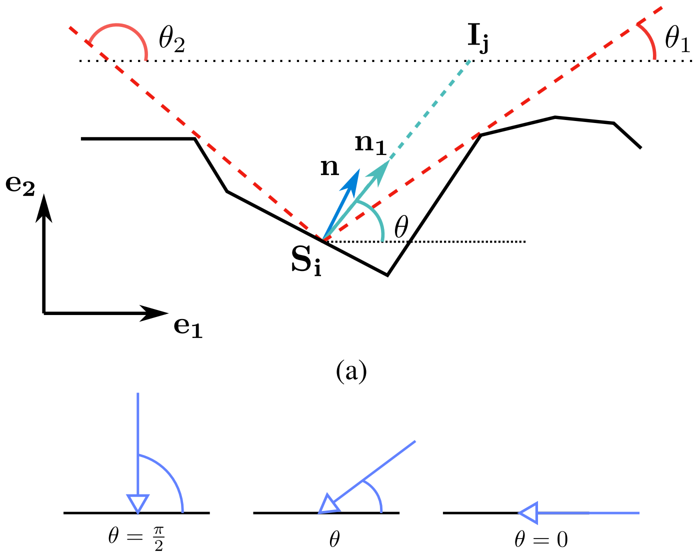

(a)

(b)

Figure 2.3: Visibility factor definition (a) surface and ion beam normal vectors, (b) orientation of impacting ions.

The visibility factor not only accounts for the shadowing with other features (by integrating Equation 2.2 from $\theta_1$ to $\theta_2$) but also the relative orientation of the incoming ions. In this work, it is assumed that ions impacting a flat surface with angles close to $\pi/2$ will produce a greater energy deposition and, therefore, this scenario is more susceptible to erosion than ions impacting with a shallow angle (close to 0) as in Figure 2.3(b) based on [21]. Nevertheless, this does not represent a restriction, and this assumption can be adjusted upon newer data. Thus, Equation 2.2 is modified to account for this behavior by adding a weighting parameter $w = w(\theta)$:

$$P(\theta) = \mathbf{n} \cdot w(\cos\theta\mathbf{e_1} + \sin\theta\mathbf{e_2}) \tag{2.3}$$

where $w$ is maximizing the effect of the visibility factor when the ions have a normal direction to the horizontal line, $\theta = \pi/2$; and minimizes it when they have a parallel direction to the horizontal line $\theta = 0$. Mathematically speaking,

$$\begin{cases} \theta = \pi/2 & \rightarrow w = 1 \\ \theta = 0 & \rightarrow w = 0 \end{cases} \tag{2.4}$$

From all possible functions that can be used to define $w$, a sine function is a smooth function that meets the requirements expressed by Equation 2.4:

$$w(\theta) = \sin\theta \tag{2.5}$$

Replacing Equation 2.5 in Equation 2.3,

$$P(\theta) = \mathbf{n} \cdot (\cos\theta \sin\theta \mathbf{e_1} + \sin^2\theta \mathbf{e_2}) \tag{2.6}$$

To obtain the contribution over the entire range $\theta_1 \leq \theta \leq \theta_2$ (see Figure 2.3), Equation 2.6 is integrated and normalized with respect to the maximum value it can take, considering that $\mathbf{n}$ does not depend on the angle of the ions and that the maximum value is when a horizontal flat surface ($\mathbf{n} = \mathbf{e_2}$) and the full range of view ($0 \leq \theta \leq \pi$) are considered,

$$v_i = \frac{\mathbf{n} \cdot \int_{\theta_1}^{\theta_2} \mathbf{P_w}(\theta)\, d\theta}{\mathbf{e_2} \cdot \int_0^{\pi} \mathbf{P_w}\, d\theta} = \frac{\mathbf{n} \cdot \int_{\theta_1}^{\theta_2} \mathbf{P_w}(\theta)\, d\theta}{\pi/2} = \frac{2}{\pi}\mathbf{n} \cdot \int_{\theta_1}^{\theta_2} \mathbf{P_w}\, d\theta \tag{2.7}$$

where $\mathbf{P_w} = (\cos\theta \mathbf{e_1} + \sin\theta \mathbf{e_2})$.

*Size factor*

The size factor relates the characteristic dimensions of the current surface's features such as dominant wavelength $L$, and corresponding amplitude $A$, with the Debye length of the plasma $\lambda_D$, by obtaining a ratio of areas defined as,

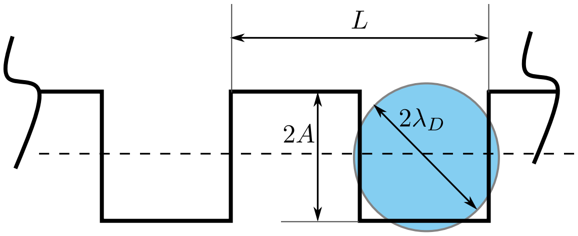

Figure 2.4: Size factor parameters, Debye length $\lambda_D$, wavelength $L$, and amplitude $A$.

$$\begin{aligned} A_S &= (2A)(L/2) = AL \\ A_{\lambda_D} &= \pi \lambda_D^2 \end{aligned} \tag{2.8}$$

where $A_S$ represents the rectangular area produced by the dominant wavelength $L$ and amplitude $A$ of a square signal and $A_{\lambda_D}$ represents a circular area of the Debye length of the plasma. An equivalent Debye length $\bar{\lambda}_D$ is defined such that it has the same area as the fictitious area $A_S$ as shown in Figure 2.4,

$$\bar{\lambda}_D = \left( \frac{LA}{\pi} \right)^{\frac{1}{2}}$$

Finally, the *size factor* $h$ is defined as the ratio of the equivalent Debye length for the current surface profile to the Debye length of the plasma,

$$h = h_s \frac{\bar{\lambda}_D}{\lambda_D} = h_s \frac{\left( \frac{LA}{\pi} \right)^{\frac{1}{2}}}{\lambda_D} \tag{2.9}$$

where $h_s$ is a proportionality constant that compensates the fact that the square signal decomposes in several frequencies (as opposed to a sine wave), and it will be used to calibrate the size factor with the experiments in subsubsection 2.2.2. The upper bound of this parameter $h = 1$ is chosen when the equivalent Debye length obtained from the features of the surface resembles the Debye length of the plasma.

As it can be seen from Equation 2.9, as the surface evolves due to the erosion process, so do the dominant length and amplitude, leading to a progressive variation of the size factor in each step. For this purpose, a Fast Fourier Transformation (FFT) is used to obtain these features. Before processing the FFT, a spline interpolation from the Python module *Scipy* [30] is used to smoothen the raw surface profile from the FE mesh in order to capture the main features as depicted in Figure 2.5(a) and its inset. Once the profile is smoothened, the dominant wavelength and amplitude are obtained from the FFT, as shown in Figure 2.5(b) with an "x" marker. Finally, the size factor is then calculated using Equation 2.9.

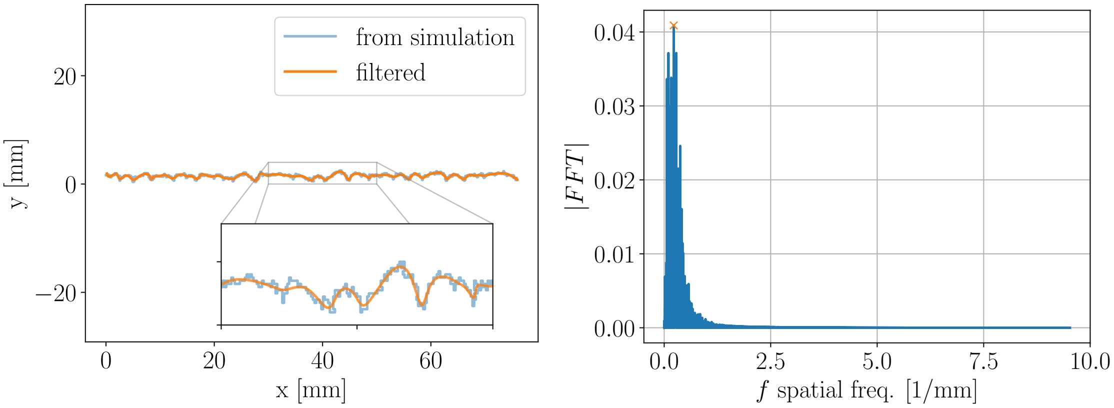

(a) Smoothed profile

(b) FFT of smoothed profile

Figure 2.5: Filtering of the surface profile from FE mesh for FFT to obtain the dominant wavelength $L$ and amplitude $A$ per each erosion step.(a) The transition of the surface profile from the raw FE mesh to a smoother curve for FFT processing, (b) FFT and criteria to define the dominant length $L$ and amplitude $A$ from the moving averaging.

The size factor $h$ controls the transition between a ***Flat regime*** and a ***Rippled regime*** defined as follows:

**Flat regime.** For $h \to 0$, the surface features are not well-developed and they "look" flat for the ions.

**Rippled regime.** For $h \geq 1$, the surface features are comparable with the Debye Length. This is important since, according to [29], once the features' size is of the order of $O(\lambda_D)$ the concentration of electrons is such that it allows greater energy deposition at the grooves than at the peaks of the surfaces.

**Transition regime.** For values of the size factor $0 < h < 1$, interpolation is carried out as detailed in subsubsection 2.2.2.

*Interpolation functions and Regimes*

At the beginning of the erosion process, the Debye length is compared against a "flat" surface. However, as the erosion process takes place, the Debye length is compared with a "rippled" surface leading to a completely different energy deposition to the wall. Thereby, with this interpolation scheme, there is a smooth transition between these regimes driven by the plasma-wall interaction, as shown in Table 2.1. The limiting values of the energy can be readily obtained from Figure 2.7(b). As mentioned in the previous section, $E_F$ and $E_G$ provide the reference values to interpolate the ion energy as a function of the visibility and size factor as described by Equation 2.10.

Table 2.1: Regimes definition as a function of the size factor $h$.

| Regime | Case | Maximum | Minimum |
|---|---|---|---|
| Flat | $h \to 0$ | $E_F$ | 0 |
| Rippled | $h \geq 1$ | $E_G$ | $E_F$ |
| Transition | $0 < h < 1$ | Interpolation | |

Then, the ion energy at a given erosion step is $E_{ion} = E(v,h)E_G$ where $E(v,h)$ is the point-wise normalized ion energy with respect to the energy measured at the "groove" $E_G$ given by,

$$E(v,h) = \begin{cases} E_0(v) = \frac{E_F}{E_G}v & h \simeq 0 \\ E_h(v,h) = (1-h)E_0(v) + hE_1(v) & 0 < h < 1 \\ E_1(v) = a_1 v + a_2 & \geq 1 \end{cases} \tag{2.10}$$

where $v$ is the point-wise *visibility factor*, $h$ is the global *size factor* as a function of the current dominant wavelength $L$ and amplitude $A$ of the surface and $E_F$,$E_G$ are the point-wise ion energy references at the "front" and "groove" surfaces, respectively. The variables $a_1$ and $a_2$ are used to calibrate the interpolating function with the experiments, as it will be discussed in subsubsection 2.2.2. Equation 2.10 establishes that when $h = 0$ the energy deposited is governed by the *visibility factor* and reaches its maximum of $E_F$ as $v \to 1$, *i.e.*, at this regime, the energy is purely driven by shadowing effects. On the other hand, once the scale of the features is in the same order of magnitude as $\lambda_D$, *i.e.*, as $h \to 1$, places with less visibility (according to Equation 2.7) to the ions (such as grooves), will actually receive more energy and reaching its reference value $E_G$ as the visibility approaches a value $v^*$ obtained from the calibration, as it is discussed in subsubsection 2.2.2. Figure 2.6 shows a graphical representation of Equation 2.10.

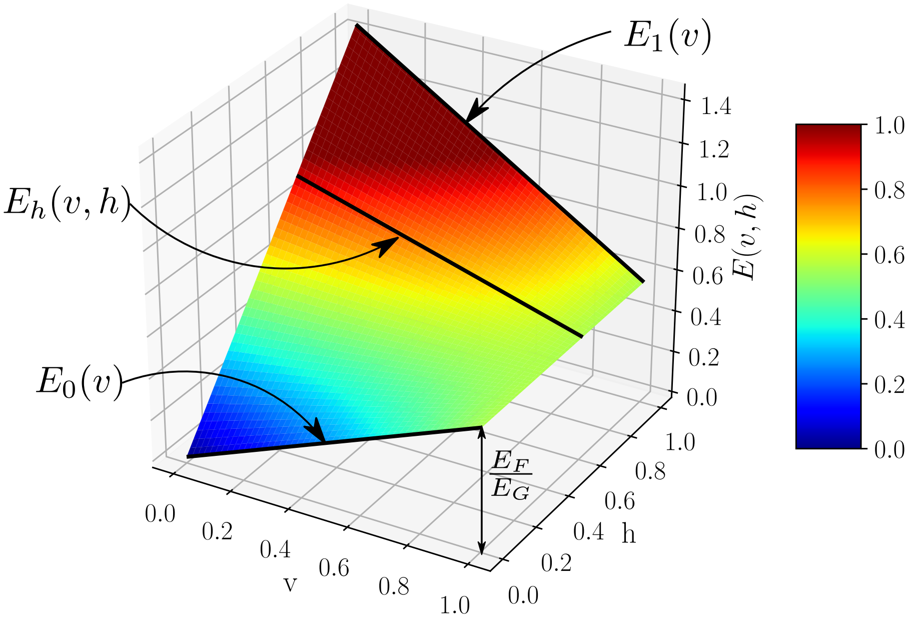

Figure 2.6: Interpolation surface

Before continuing to the calibration section, it should be noted that Equation 2.10 is applied at each integration point of the surface ($S_i$ as defined in Figure 2.3). In addition, **because the ions impact the surface with a certain probability density function as illustrated in Figure 2.2, the surface points $S_i$ do not have the same reference bounds**

$E_F$ **and** $E_G$ **for the interpolation scheme.** The reference bounds $E_F$, $E_G$ from the ion energy probability distributions at the "front" and "groove" respectively for surface point $S_i$, are obtained using the *inverse transformation method* [31] since these distributions do not resemble any well-known probability functions. Figure 2.7(a) shows this process schematically. A representative sample with the desired probability is attained as follows. First, the cumulative distributions of each region (front and groove) are obtained as shown in red dashed lines in the picture; then, a uniformly distributed sampling is mapped to the cumulative distribution and retrieved the value of the ion energy associated to it. Figure 2.7(b) shows the obtained distribution after performing this process over 200 times. It can be seen that the reference ion energies $E_F$ and $E_G$ gathered through this process is in good agreement with the input distribution. Thereby, the interpolation functions are also stochastic provided that the ratios $E_F/E_G$, $a_1$, and $a_2$ are random variables and change from one surface point to another.

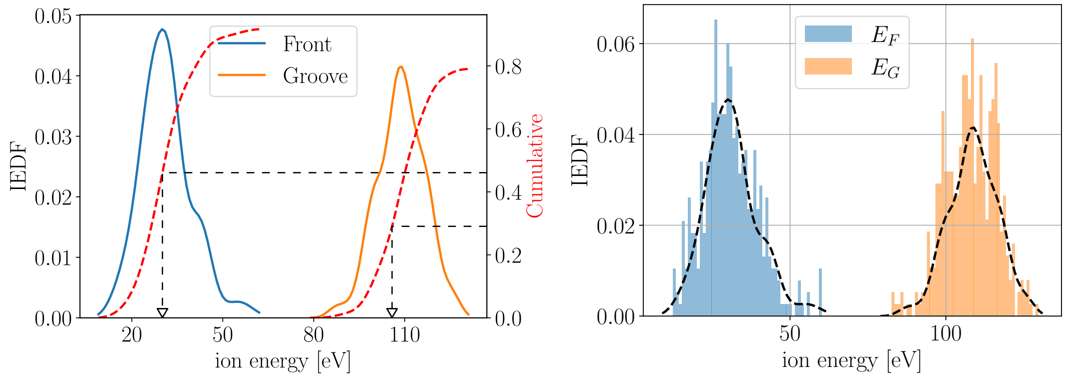

(a) (b)

Figure 2.7: Sampling of ion energy $E_F$ and $E_G$ for the references bounds at the "front" and "groove", respectively; (a) sampling from an ion energy probability distribution from its cumulative distribution, (b) the recovered ion energy distribution after sampling 200 times.

*Calibration of geometric parameters*

This section shows how the *size factor* and the interpolating scheme are calibrated based on the ion energy data from Figure 2.7.

The size factor $h$ is a geometrical parameter that only depends on the dominant wavelength of the current surface stage, and the Debye length that is assumed constant. The geometry of the surface is a regular pattern of grooves of 5 mm depth and width, as shown in Figure 2.8(a). The profile dominant wavelength $L$ and amplitude $A$ are obtained with the FFT as discussed in subsubsection 2.2.2. Considering Equation 2.9, and that $h = 1$ for the geometry features from [29], the scaling factor $h_s$ is

$$h_s = \frac{\lambda_D}{(AL/\pi)^{(1/2)}} \approx 2.1 \tag{2.11}$$

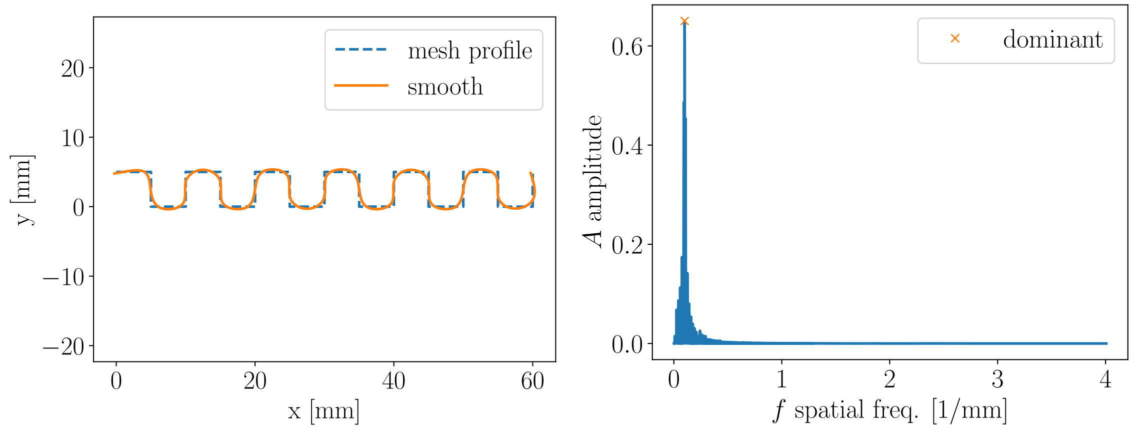

(a) (b)

Figure 2.8: Calibration of the size factor. Geometry and fitted curve in the upper subfigure and FFT of the fitted curve in the lower subfigure.

As previously discussed in subsubsection 2.2.2, the random variables $a_1$ and $a_2$ are used to calibrate the interpolating scheme in the *rippled regime*, $h \geq 1$, *i.e.*, when the surface has the same equivalent features like the geometry shown in Figure 2.8(a). It is worth noticing here that the visibility factor calculated at the central point of one of the grooves is approximately $v^* = 0.5$, as shown in the inset of Figure 2.9(a). Therefore, the first condition is that (a) the normalized ion energy is 1 when $v = v^*$, $E(v^*, h \geq 1) = 1$. The second condition is given by the assumption that (b) at the front, *i.e.*, when the visibility is $v = 1$, the ion energy is $E_F$, thus, the normalized ion energy is $E(v = 1, h \geq 1) = \frac{E_F}{E_G}$.

Lastly, in this work, a linear function is chosen since it is the simplest function that can meet the criteria (a) and (b) among all possible functions, as shown in Figure 2.9(a). It should be noted that this does not represent any restriction if a more complex function is selected as new data becomes available. Given these conditions, the variables $a_1$ and $a_2$ are:

$$a_1 = \frac{1 - \frac{E_F}{E_G}}{v^* - 1} \tag{2.12}$$

$$a_2 = \frac{\frac{E_F}{E_G} v^* - 1}{v^* - 1} \tag{2.13}$$

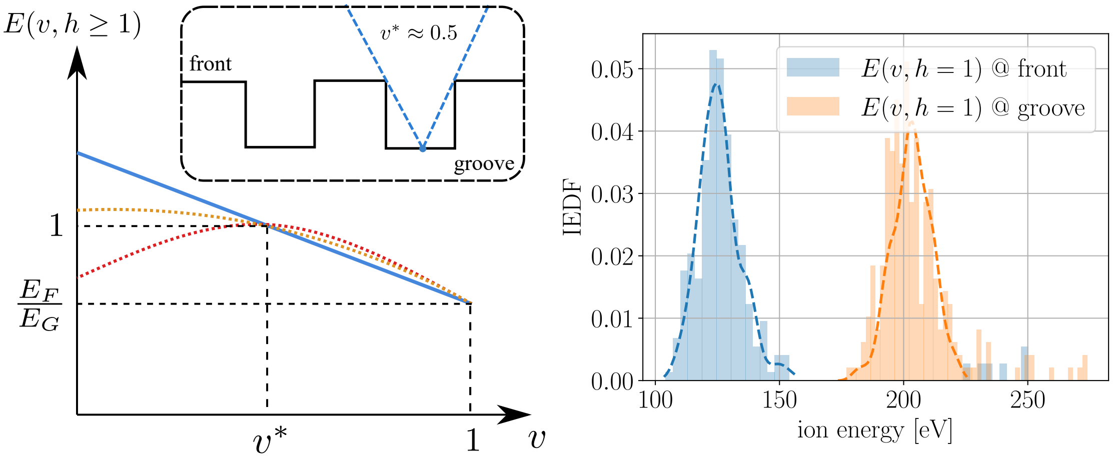

(a) (b)

Figure 2.9: Calibration of random variables $a_1$ and $a_2$. (a) The visibility factor is evaluated at the center point of the groove, $v^*$, and the possible functions and fitting parameters to determine the variables. (b) The corresponding ion energy distributions obtained with the calibrated interpolating function of Equation 2.10.

As shown in Figure 2.9(b), the reference's ion energy distributions (at the groove and front) obtained with this sampling method are close to the desired energy distributions once Equation 2.10 is calibrated.

### 2.2.3 Mesh independent erosion rate

The erosion rate is a measure to estimate of how fast the walls are being eroded from the operation of the device and thus, is valuable information for the design engineers to define or predict the lifetime of the thrusters. Because the model in this work is based on element-removal, *i.e.*, the erosion is simulated by actively removing elements of the surface profile at each step rather than modifying the position of the nodes, the erosion rate is defined as follows. First, the discretization is through square elements with height $y_e$ and width $x_e$. A *local erosion rate* for each element is then defined as,

$$\dot{y}_e = \frac{y_e}{\Delta t} \tag{2.14}$$

where $\Delta t$ is the time increment for the erosion step. Let us also define an *equivalent erosion rate* given by,

$$\bar{y} = \frac{\sum_{e=1}^{k} \dot{y}_e}{N} \tag{2.15}$$

In this work, all elements have the same height $y_e$, thus the same local erosion rate $\dot{y}_e$ and the summation in the numerator is $\sum_{e=1}^{k} = \dot{y}_e = k\dot{y}_e$. Plugging Equation 2.14 in Equation 2.15, it can be re-written as

$$\bar{y} = \frac{k\dot{y}_e}{N} = \frac{ky_e}{N\Delta t} \tag{2.16}$$

where $k$ is the number of elements removed in the current iteration, and $N$ is the total number of elements in the frontier. This erosion rate produces a recession of $\bar{y}$ for the current iteration, as shown in Figure 2.10. It can be easily verified that when all elements of the frontier are removed, $k = N$, the equivalent erosion rate is equal to $\dot{y}_e$, which corresponds to a recession of $\bar{y} = y_e$.

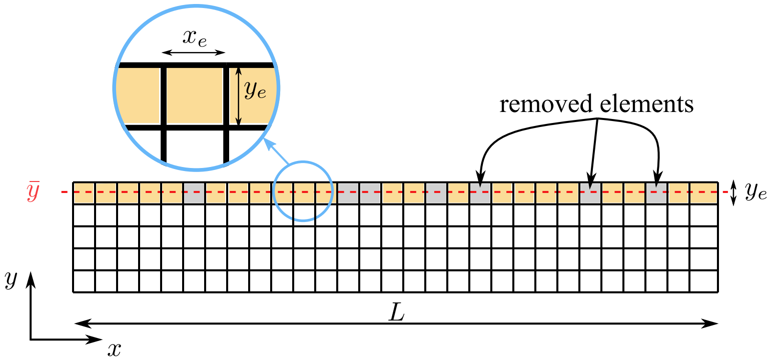

Figure 2.10: Schematics for the erosion rate estimation.

In light of Equation 2.16, this methodology is mesh dependent because the mean erosion rate is proportional to the ratio of removed and frontier elements, $k/N$, *i.e.*, if the element size $y_e$ changes, $k/N$ should also change accordingly. In order to attain this, the mean erosion rate $\dot{\bar{y}}$ (Equation 2.16, at any time during the simulation) should be constant. Therefore, the following relation should hold:

$$\dot{\bar{y}} = \frac{k^{(1)} y_e^{(1)}}{N^{(1)} \Delta t} = \frac{k^{(2)} y_e^{(2)}}{N^{(2)} \Delta t} = \cdots = \frac{k^{(n)} y_e^{(n)}}{N^{(n)} \Delta t} \tag{2.17}$$

where the superscript indicates a different mesh. Neglecting the time increment since it does not depend on the mesh, and considering that the total number of elements for mesh $j$ in the $x$ direction is $N^{(j)} = L/x_e^{(j)}$ as shown in Figure 2.10,

$$L_c = \frac{k^{(j)} y_e^{(j)}}{N^{(j)}} = \frac{k^{(j)} y_e^{(j)} x_e^{(j)}}{L} \tag{2.18}$$

where $L_c$ is an *invariant characteristic length* that is defined in the following section. Therefore, once $L_c$ is obtained, the number of removed elements (in average) is defined for a given mesh size $x_e^{(j)}, y_e^{(j)}$. For example, if mesh 1 (M1) has element size $x_1, y_1$ and mesh 2 (M2) has element size $x_2 = 2x_1, y_2 = 2x_2$; the number of elements to be removed in mesh 1 is obtained from Equation 2.18,

$$k_1 = \frac{L_c L}{x_1 y_1}$$

and the number of elements to be removed in mesh 2:

$$k_2 = \frac{L_c L}{x_2 y_2} = \frac{L_c L}{2x_1 2y_1} = \frac{L_c L}{4x_1 y_1} = \frac{k_1}{4}$$

Which agrees with the fact that coarser meshes should (in average) remove fewer elements in order to produce the same mean erosion rate as finer meshes.

### 2.2.4 Element removal criterion

Finally, the criteria to decide whether an element of the frontier is removed or not is determined by a function that depends on the current power to the wall at the given element (as a heat flux) and its current strain energy as calculated from the material model discussed in subsection 2.3.2. Figure 2.11 shows that for a given value of power $P$ and strain energy ratio $D$ for the element, the probability $J(P, D)$ for that element to be removed is obtained from the surface that results from an interpolation of two functions. The first corresponds to $J_0(P)$ that depends only on the power when the strain energy ratio is $D_0 = 0$, and the second corresponds to the upper limit of $J_1(P)$ when the material reaches its maximum strain energy ratio ($D = 1$). Naturally, there is no erosion if the power to wall is zero $P = 0$, $J(P = 0, D) = 0$. The surface of Figure 2.11 can be represented as,

$$J(P, D) = \begin{cases} J_0(P) & D = D_0 \\ J_1(P) & D \geq 1 \\ f\left(J_0(P), J_1(P), D\right) & D_0 < D < 1 \end{cases} \tag{2.19}$$

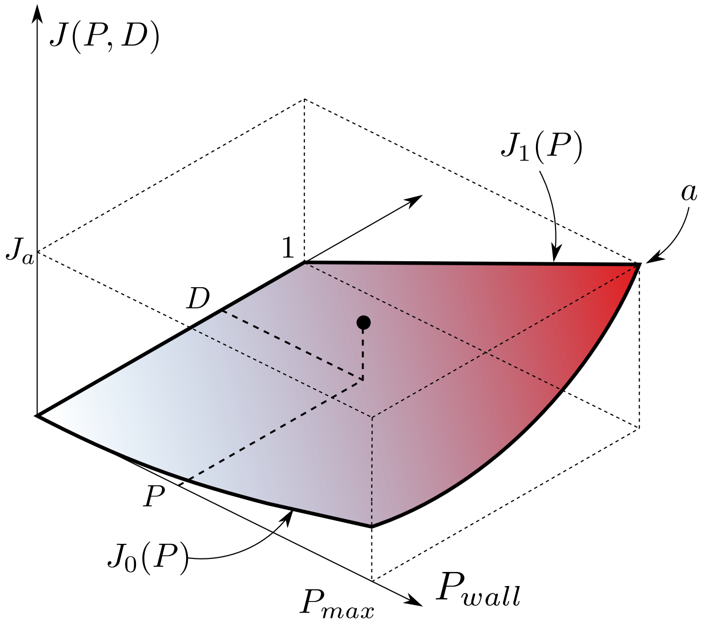

Figure 2.11: Schematics for the joint probability function definition. $J_0(P)$ and $J_1(P)$ are the bounds of the joint probability function when the strain energy ratio is $D = 0$ and $D = 1$. For a given value of strain energy ratio $D$ and power to wall $P$, the joint probability distribution $J(P, D)$ is obtained from an exponential interpolation.

The erosion process is as follows. During the step in which the surface is updated based on the power to the wall and the strain energy ratio of the frontier elements, a random number drawn from a uniform distribution $r \in U(0, 1)$ is compared with the probability obtained from Equation 2.19. If the sampled random number is smaller than the probability for a given element, that element is removed, and the process continues until all elements in the surface are considered. This process is schematically shown in algorithm 1. The definitions of $J_0(P)$ and $J_1(P)$ are discussed in the following subsections.

**Algorithm 1:** Remove elements based on the probability function.

```
for element ∈ frontier elements do
    Get the power applied to element, $P_{wall}$ ;
    Get the current strain energy ratio $D$ ;
    Calculate the probability of being removed from Equation 2.19 ;
    Sample a random number $r$ with uniform distribution, $r \in U(0,1)$ ;
    if $r \leq J(P,D)$ then
        remove this element ;
    end
end
```

*Definition of $J_0(P)$ - Purely sputtering model*

As it was mentioned in the previous paragraph, the $J_0(P)$ bound depends on the power only; thus, it does not account for any material properties. Therefore, it is chosen such that the equivalent erosion rate $\bar{y}$ is equal to the erosion rate achieved by the state-of-the-art models. In this work, Yamamura's sputtering yield model [10] is employed as a function of the ion energy $E_{\text{ion}}$ and the ions' incident angle $\theta$ given by:

$$Y(E_{\text{ion}},\theta) = k(B_0 + B_1\theta + B_2\theta^2 + B_3\theta^3)\sqrt{E_{\text{ion}}}\left(1 - \sqrt{\frac{E_{th}}{E_{\text{ion}}}}\right)^{2.5} \tag{2.20}$$

where the coefficients are obtained from [21] as shown in Table 2.2.

Table 2.2: Sputtering yield constants used in this chapter, [21].

| Parameter | Value |
|---|---|
| $E_{th}$, eV | 18.3 |
| $B_0$ | 1.18 |
| $B_1$ | 1.94E-02 |
| $B_2$ | 1.22E-04 |
| $B_3$ | -2.22E-06 |
| $k$ | 2.28E-03 |

The erosion rate from the sputtering yield is simply $\dot{y}_{\text{sy}} = Y(E_{\text{ion}})j_{\text{ion}}$ where $j_{\text{ion}}$ is the ion current density to the wall. Thus, the equivalent erosion rate from the model is[1],

$$\bar{\dot{y}} = \dot{y}_{\text{sy}} = Y(E_{\text{ion}})j_{\text{ion}} \tag{2.21}$$

and using the definition of Equation 2.15,

$$\frac{\sum_{e=1}^{k} \dot{y}_e}{N} = \dot{y}_{\text{sy}} \tag{2.22}$$

Since all elements have the same height $y_e$, the above expression becomes,

$$\frac{k\dot{y}_e}{N} = \dot{y}_{\text{sy}} \tag{2.23}$$

Finally, the number $k$ of elements to be removed to preserve the equality is obtained,

$$k = \frac{N}{\dot{y}_e}\dot{y}_{\text{sy}} \tag{2.24}$$

---

[1] sputtering yield dependency with the angle is dropped to simplify the notation. However, it still varies according to the ions' incidence.

where $Y$ is the sputtering Yield in $mm^3/C$, $j_{\text{ion}}$ is the current density in $A/mm^2$, thus the erosion rate $\dot{y}_{\text{sy}}$ is in $mm/s$. In this case, the invariant characteristic length $L_c$ can be obtained considering Equation 2.18 and Equation 2.24,

$$L_c^{(\text{sy})} = \dot{y}_{\text{sy}} \Delta t \tag{2.25}$$

which corresponds to the average erosion depth due a pure sputtering model and is independent of the mesh.

Equation 2.24 indicates that in order to preserve an erosion rate equivalent to the one obtained by purely sputtering yield (when the strain energy ratio is $D_0$), $k$ elements should (in average) be removed from the frontier. The process of removing $k$ elements out of $N$ with certain probability $p$ can be described by the Binomial distribution, $P(X = k) = \binom{N}{k} p^k (1-p)^{N-k}$, with $k = 0, 1, \cdots, N$. The value of this probability can be estimated using Maximum Likelihood Estimation (MLE) as [32]

$$p \approx \frac{k}{N} \tag{2.26}$$

In this work, the probability depends on the power $p = J_0(P)$, and in light of Equation 2.18, Equation 2.26 can be rewritten as

$$J_0(P) = \frac{L_c}{y_e} = \frac{\dot{y}_{\text{sy}}(P)\Delta t}{y_e} \tag{2.27}$$

It should be noted here that since the sputtering yield is a function of the ion energy, so is the number of elements to be removed $k$. Thus, the curve $J_0(P)$ is obtained as described in algorithm 2 considering that the power is defined with Equation 2.1 as the product of the ion current and ion energy. Figure 2.12 shows the values of $J_0(P)$ for three different element sizes (M1, M2 and M4), wherein each case, the element size is doubled from its predecessor. There are multiple observations that can be made from the figure. First, it can be seen that coarser meshes have a smaller probability of element removal to maintain the same erosion rate in each case. Second, there is a limiting element size in which the probability is one. Finally, there is a range of the normalized power to wall up to around $\approx 0.15$, in which the probability is zero. This corresponds to the ion energy threshold $E_{th}$ (18.3 eV from Table 2.2) for which the sputtering yield is also zero (thus no erosion is expected for energies below that value).

---

**Algorithm 2:** Process to determine the function $f_0(P)$ at strain energy ratio $D_0$.

```
for $E_{ion}$ in range($E_{min}, E_{max}$) do
    Calculate the power $P = E_{\text{ion}} j_{\text{ion}}$;
    Calculate the sputtering yield $Y(E_{\text{ion}})$ with Equation 2.20;
    Calculate the erosion rate due sputtering with $\dot{y}_{\text{sy}} = Y(E_{\text{ion}}) j_{\text{ion}}$;
    Calculate the probability $J_0(P)$ with Equation 2.26;
end
```

---

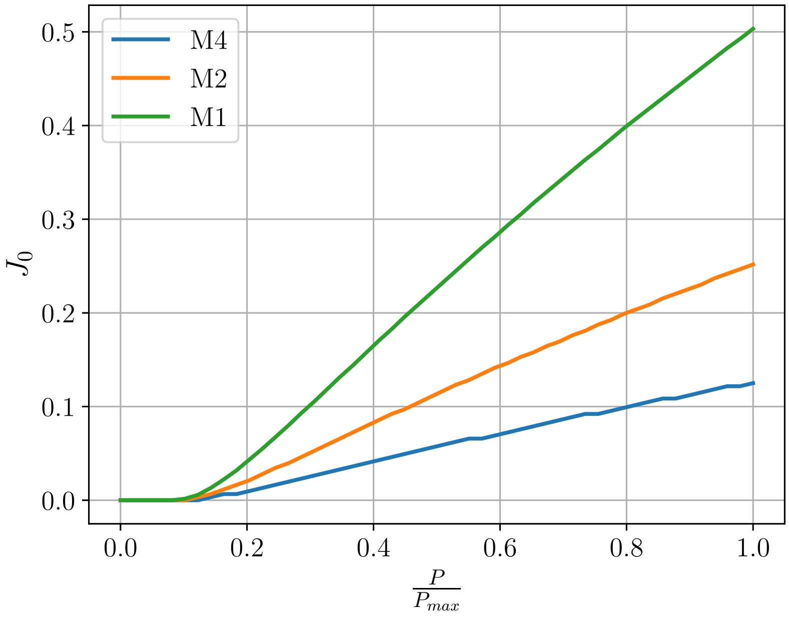

Figure 2.12: Probability function when strain energy ratio is $D_0$, $J_0(P)$ normalized with the element size as a function of the power from the ions $P$ against the wall.

*Definition of $J_1(P)$ - Damaged material*

The $J_1(P)$ bound depends on material failure criteria. For simplicity, this work uses simple failure criteria for ceramics based on the maximum normal stress criterion in which the material is considered to have failed when any of the principal stresses reaches either the tensile $\sigma_U$ or compressive $\sigma_C$ strength of the material,

$$\begin{aligned} \sigma_{1,2,3} &\geq \sigma_U \qquad \text{tension} \\ |\sigma_{1,2,3}| &\geq \sigma_C \qquad \text{compression} \end{aligned} \tag{2.28}$$

The strain energy ratio parameter $D$ is represented by the ratio of the current point-wise strain energy density at each surface point $w$ with the maximum strain energy density $w_{\text{max}}$ given by

$$D = w/w_{\text{max}} \tag{2.29}$$

where $w_{\text{max}}$ depends on the failure criteria and boundary conditions of the problem.

Because a failure criterion is defined for $J_1(P)$ bound, it is assumed that the material integration point fails if the RVE (Representative Volume Element) of the microstructure meets the failure criteria. Therefore, the characteristic length is considered equal to the size of RVE,

$$L_c = y_{\text{RVE}} \tag{2.30}$$

Recalling Equation 2.18 and Equation 2.26 the maximum probability given at point $a$ in Figure 2.11 is

$$J_a = \frac{L_c}{y_e} = \frac{y_{\text{RVE}}}{y_e} \tag{2.31}$$

Finally, the $J_1(P)$ is obtained using a simple linear function, as shown in Figure 2.11,

$$J_1(P) = \frac{P}{P_{max}} J_a = \frac{P}{P_{max}} \frac{y_{\text{RVE}}}{y_e} \tag{2.32}$$

As stated in Equation 2.19 once the $J_0(P), J_1(P)$ bounds are defined, the interpolation for any given value of the strain energy ratio $D$ and power $P$ is calculated with an exponential function of the form

$$f(P, D) = A(P)B(P)^D \tag{2.33}$$

where $A(P)$ and $B(P)$ are obtained using the following constraints:

$$\begin{aligned} f(P, 0) = A(P) &= J_0(P) \\ f(P, 1) = A(P)B(P) &= J_1(P) \end{aligned} \tag{2.34}$$

Hence Equation 2.33 becomes,

$$f(P, D) = J_0 \left(\frac{J_1}{J_0}\right)^D \tag{2.35}$$

Plugging Equation 2.27 and Equation 2.32 into Equation 2.35 the interpolation function becomes,

$$f(P, D) = \left(\frac{\dot{y}_{\text{sy}}(P)\Delta t}{y_e}\right)^{1-D} \left(\frac{P}{P_{max}} \frac{y_{\text{RVE}}}{y_e}\right)^D \tag{2.36}$$

Figure 2.13(a) shows the joint probability distribution for three meshes (M1, M2, M4) and a fixed time increment, and Figure 2.13(b) shows the joint probability distribution for mesh M1 and three time increments given by $\Delta t_1$, $\Delta t_2 = 2\Delta t_1$ and $\Delta t_3 = 3\Delta t_3$.

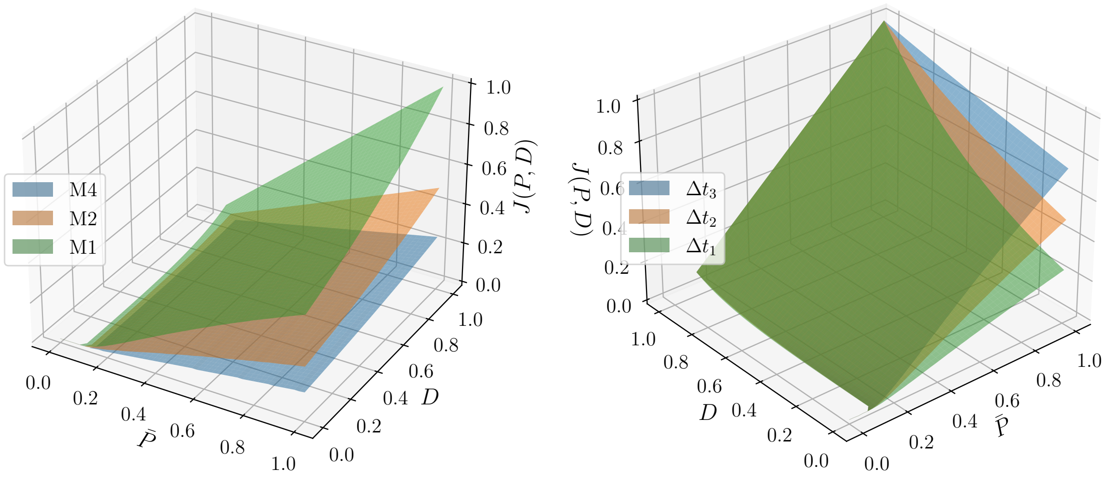

(a) (b)

Figure 2.13: (a) Joint probability distribution for three different meshes, M1, M2, and M4. (b) Joint probability distribution for M1 and three different time increments.

In this way, the joint probability distribution provides the same rates of erosion regardless of mesh or time increment selection.

## 2.3 Finite Element Model

### 2.3.1 Thermal model

Consider a body $\Omega$ with boundary $\partial S$ subjected to heat transfer as shown in Figure 2.14. In addition, consider that the material follows the Fourier law of heat conduction[2],

$$\mathbf{q} = -\mathbf{D} \cdot \nabla T \qquad \text{or} \qquad q_i = -D_i \frac{\partial T}{\partial x_i} \tag{2.37}$$

where $\mathbf{q}$ is the heat flux, $T$ is the temperature field, and $\mathbf{D}$ is the thermal conductivity tensor. The heat transfer problem consists of finding the temperatures $T$ to satisfy the heat flow equilibrium in the body,

---

[2] No summation over $i$

$$\nabla\left(\mathbf{D}\cdot\nabla T\right) = -\left(\rho C_P \frac{\partial T}{\partial t}\right) \tag{2.38}$$

subject to the boundary conditions,

$$D_n \frac{\partial T}{\partial \mathbf{n}} = -P_{wall} \qquad \text{on } \partial S_q \tag{2.39a}$$
$$D_n \frac{\partial T}{\partial \mathbf{n}} = 0 \qquad \text{on } \partial S_{left} \cup \partial S_{right} \tag{2.39b}$$
$$D_n \frac{\partial T}{\partial \mathbf{n}} = q^R \qquad \text{on } \partial S_{bottom} \tag{2.39c}$$

where $\rho$ is the material density, $C_p$ is the heat capacity, and $\mathbf{n}$ indicates the normal vector of the surface where the heat flux is applied. The radiation boundary conditions $q^R$ is defined as,

$$q^R = \sigma\psi\left(T_{ref}^4 - T_S^4\right)$$

which when factorized, becomes,

$$q^R = \kappa\left(T_{ref} - T_S\right) \tag{2.40}$$

with

$$\kappa = \sigma\psi(T_{ref}^2 + T_S^2)(T_{ref} + T_S)$$

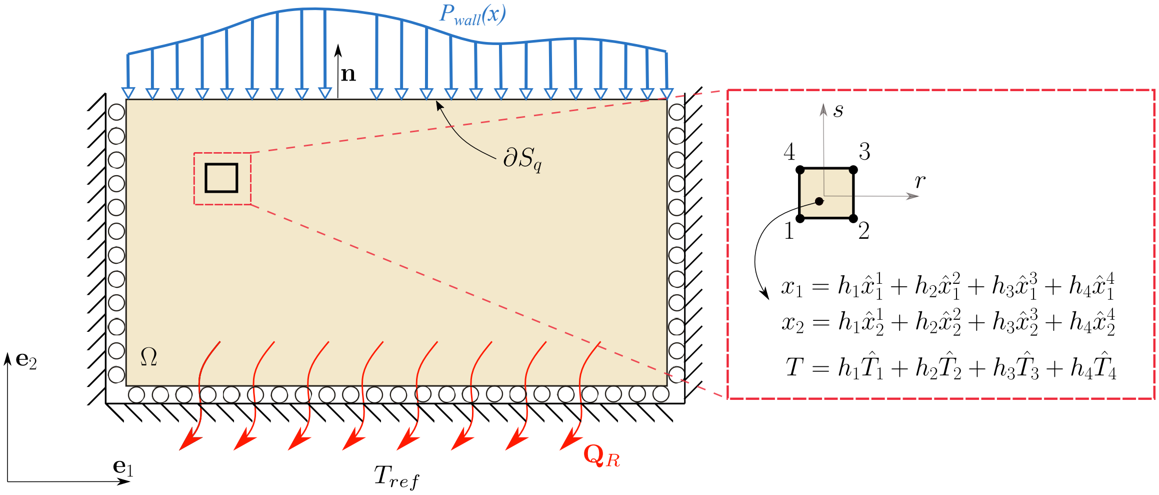
$P_{wall}(x)$
$\mathbf{n}$
$\partial S_q$
$s$
4
3
$r$
1
2
$x_1 = h_1\hat{x}_1^1 + h_2\hat{x}_1^2 + h_3\hat{x}_1^3 + h_4\hat{x}_1^4$
$x_2 = h_1\hat{x}_2^1 + h_2\hat{x}_2^2 + h_3\hat{x}_2^3 + h_4\hat{x}_2^4$
$T = h_1\hat{T}_1 + h_2\hat{T}_2 + h_3\hat{T}_3 + h_4\hat{T}_4$
$\mathbf{e}_2$
$\Omega$
$\mathbf{e}_1$
$T_{ref}$
$\mathbf{Q}_R$

Figure 2.14: Diagram for the Finite Element Model of the thermo-mechanical problem.

The domain $\Omega$ is subdivided into elements $\Omega_e$ so that the union of all elements comprises the total domain, $\Omega = \cup\Omega_e$. For each element, the interpolation of the position $\mathbf{x}$ and the temperatures $T$ is performed with the same *isoparametric interpolation functions*, $h_i(r, s)$ evaluated at the nodes, $i = 1, ..., 4$ using natural coordinates $r, s$ [33], as shown in the inset of Figure 2.14 with,

$$x_I = h_i \hat{x}_I^i \tag{2.41}$$

and

$$T = h_i \hat{T}_i = \mathbf{H}\hat{\mathbf{T}} \tag{2.42}$$

and their derivatives as,

$$\frac{\partial T}{\partial x_j} = \frac{\partial h_i}{\partial x_j}\hat{T}_i = B_{ji}\hat{T}_i = \mathbf{B}\hat{\mathbf{T}} \tag{2.43}$$

where $\mathbf{H}$ and $\mathbf{B}$ are a rectangular matrix with thermal interpolation functions and their derivatives, respectively, and $\hat{T}_i$ is the nodal temperatures in the element at the $i$-th node. Applying the discretization of the temperatures and their derivatives, Equation 2.38 can be written as [33],

$$\mathbf{C}\dot{\mathbf{T}} + (\mathbf{K} + \mathbf{K_R})\mathbf{T} = \mathbf{Q_S} + \mathbf{Q_R} \tag{2.44}$$

with,

$$\begin{array}{lllllll}
\mathbf{K} & = & \sum_{el}\mathbf{K}^{el} & & \mathbf{K}^{el} & = & \int_{\Omega^{el}}\mathbf{B}^T k\mathbf{B}\,d\Omega^{el} \\
\mathbf{K_R} & = & \sum_{el}\mathbf{K_R}^{el} & & \mathbf{K_R}^{el} & = & \int_{S_R^{el}}\mathbf{H_S}^T\kappa\mathbf{H_S}\,dS^{el} \\
\mathbf{C} & = & \sum_{el}\mathbf{C}^{el} & & \mathbf{C}^{el} & = & \int_{\Omega^{el}}\mathbf{H}^T\rho C_p\mathbf{H}\,d\Omega^{el} \\
\mathbf{Q_S} & = & \sum_{el}\mathbf{Q_S}^{el} & & \mathbf{Q_S}^{el} & = & \int_{S_q^{el}}\mathbf{H_S}^T P_{wall}^{el}\,dS^{el} \\
\mathbf{Q_R} & = & \sum_{el}\mathbf{Q_R}^{el} & & \mathbf{Q_R}^{el} & = & \int_{S_R^{el}}\mathbf{H_S}^T\kappa T_{ref}\,dS^{el}
\end{array} \tag{2.45}$$

Here, $\sum_{el}[\bullet]$ indicates ensemble over the elements of the elemental matrix $[\bullet]$ and $\mathbf{H}_S$ means that the interpolation functions $\mathbf{H}$ are evaluated at the boundary $S$.

Equation 2.44 is integrated using a $\alpha$-method and central difference for the derivatives [33],

$$\begin{array}{rcl}
{}^{t+\Delta t}\dot{T} & \approx & \frac{{}^{t+\Delta t}T-{}^{t}T}{\Delta t} \\
{}^{t+\alpha\Delta t}T & \approx & \alpha^{t+\Delta t}T+(1-\alpha)^{t}T
\end{array} \tag{2.46}$$

Plugging Equation 2.46 into Equation 2.44, we obtain,

$$\begin{array}{c}
\left[\frac{1}{\Delta t}\mathbf{C}+\alpha\left(\mathbf{K}+\mathbf{K_R}\right)\right]{}^{t+\Delta t}T-\alpha^{t+\Delta t}\left(\mathbf{Q_S}+\mathbf{Q_R}\right)= \\
\left[\frac{1}{\Delta t}\mathbf{C}+(1-\alpha)\left(\mathbf{K}+\mathbf{K_R}\right)\right]{}^{t}T+(1-\alpha)^{t}\left(\mathbf{Q_S}+\mathbf{Q_R}\right)
\end{array} \tag{2.47}$$

A full Newton-Raphson scheme is used to solve Equation 2.47 due to nonlinear radiation terms, $\mathbf{K_R}(T)$ and $\mathbf{Q_R}(T)$ with an Implicit solver, $\alpha = 1$, leading to a compact form of Equation 2.47,

$$\left[\frac{1}{\Delta t}\mathbf{C}+\left(\mathbf{K}+\mathbf{K_R}\right)\right]{}^{t+\Delta t}T={}^{t+\Delta t}\left(\mathbf{Q_S}+\mathbf{Q_R}\right)+\frac{1}{\Delta t}\mathbf{C}^{t}T \tag{2.48}$$

### 2.3.2 Mechanical model

*Equilibrium equations*

Similarly, as in the thermal model, consider the same body $\Omega$ with boundary $\partial\Omega$ as depicted in Figure 2.14. In this case, the mechanical boundary value problem consists of finding the displacements $u_i$, the strains $\epsilon_{ij}$, and the stresses $\sigma_{ij}$ to satisfy the governing equations:

$$\frac{\partial \sigma_{ij}}{\partial x_j} = 0 \qquad \text{in } \Omega \tag{2.49}$$

$$\sigma_{ij} = \underline{\underline{\sigma}}\left(\epsilon^m_{kl}, \eta\right) \qquad \text{in } \Omega \tag{2.50}$$

$$\epsilon^m_{kl} = \frac{1}{2}\left(\frac{\partial u_k}{\partial x_l} + \frac{\partial u_l}{\partial x_k}\right) \qquad \text{in } \Omega \tag{2.51}$$

subjected to the boundary conditions,

$$u_1 = 0 \qquad \text{on } \partial S_{left} \cup \partial S_{right} \tag{2.52a}$$

$$u_2 = 0 \qquad \text{on } \partial S_{bottom} \tag{2.52b}$$

$$\sigma_{ij} n_j = 0 \qquad \text{on } \partial S_q \tag{2.52c}$$

where, $\sigma_{ij}$ is the Cauchy stress tensor, $\underline{\underline{\sigma}}\left(\epsilon^m_{kl}, \eta\right)$ indicates that it depends on the mechanical part of the infinitesimal strain tensor $\epsilon^m_{kl}$, and the internal state of the material $\eta$, and $u_1$, $u_2$ are the horizontal and vertical components of the displacement vector $u$, respectively. It should be noted here that since the stress waves travel much faster than the overall erosion process, the dynamic effects are neglected in Equation 2.49. Equation 2.49 - Equation 2.52 are discretized with the same discretization of finite elements $\Omega_e$ as in the thermal model [33] (but in this case, with displacement Degree of Freedom (DOF)) and re-written in the following general form

$$\mathbf{K}\mathbf{U} = \mathbf{R} \tag{2.53}$$

$$\begin{array}{lllllll} \mathbf{K} & = & \sum_{el} \mathbf{K}^{el} & \qquad & \mathbf{K}^{el} & = & \int_{\Omega^{el}} \mathbf{B}^T \mathbb{C} \mathbf{B} \, d\Omega^{el} \\ \mathbf{R} & = & \sum_{el} \mathbf{R}^{el} & \qquad & \mathbf{R}^{el} & = & \int_{\partial \Omega^{el}_t} \mathbf{H_S}^T \mathbf{t}^* \, d\partial\Omega^{el} \end{array} \tag{2.54}$$

where, $\mathbf{K}$ is the stiffness matrix, $\mathbb{C}$ is the constitutive tensor, and $\mathbf{t}^*$, is the surface traction vector. The displacements and their derivatives are interpolated with the same isoparametric functions used in the thermal model,

$$u_k = h_i \hat{u}_i^k = \mathbf{H}\hat{\mathbf{u}} \tag{2.55}$$

and,

$$\frac{\partial u_k}{\partial x_j} = \frac{\partial (h_i \hat{u}_i^k)}{\partial x_j} = \frac{\partial h_i}{\partial x_j} \hat{u}_i^k = B_{ji} \hat{u}_i^k = \mathbf{B}\hat{\mathbf{u}} \tag{2.56}$$

It is worth noticing here that for the mechanical problem, there are two DOF per node: displacement in $x$ and $y$ direction; represented as the $k$ index in Equation 2.55 and Equation 2.56. Hence, the interpolation matrices $\mathbf{H}$,$\mathbf{B}$ for the material model are slightly different that the ones derived for the thermal model.

One of the key ingredients to obtain the stress state of the material, $\sigma_{ij}$ in Equation 2.50, is the constitutive law, $\mathbb{C}$ that is used to calculate the stiffness matrix $\mathbf{K}^{el}$. Many models developed to account for the plasma-wall interaction assume a linear elastic behavior of the material as in [21]. In this work, a more realistic constitutive model is considered. It accounts for the micro-cracks developed as the process evolves as explained in the following section. Because of the nonlinearities in the constitutive law, a full Newton-Raphson scheme to solve Equation 2.53.

### 2.3.3 Power deposition - Heat flux to the wall

This section shows how the power to the wall is applied to the elements' edges (since our model is 2D) to be accounted for in the FE simulation. Consider a portion of the mesh with power density $P(x)$ (power per unit length) to the frontier elements as shown in Figure 2.15(a). The total power applied to any element is calculated as the area under the curve within the limiting points $a$ and $b$ as,

$$P_{total}^{(el)} = \int_a^b P(x)dx \tag{2.57}$$

Equation 2.57 can be approximated numerically using the trapezoid rule, Simpson, Gaussian quadrature, *etc*. In this work, the Gaussian quadrature rule is used. For this method, the function is evaluated at sampling points $P(x_i)$ with weights $w_i$ where $x_i$ are obtained using natural coordinates that map the domain $x \in [a, b]$ to $x' \in [-1, 1]$ from a local coordinate system as illustrated in Figure 2.15(b) [33],

$$x_i = \frac{b-a}{2} x'_i + \frac{a+b}{2} \tag{2.58}$$

and due to this change of variables, $dx = (b-a)/2dx'$. By using Equation 2.58 and noting that $L_e = b - a$ is the element's width (see Figure 2.15(b)), Equation 2.57 can be re-written as,

$$P^{(el)}_{total} = \int_a^b P(x)dx = \frac{b-a}{2} \int_{-1}^{1} P\left(\frac{b-a}{2}x' + \frac{a+b}{2}\right) dx' \approx \frac{L_e}{2} \sum_i^n w_i P(x_i) \tag{2.59}$$

Finally, recall that Equation 2.59 provides the total power exerted on the element $el$ in mW. Consequently, the equivalent power density (power per unit length) to be applied in the FE model in Equation 2.45 is obtained as,

$$P^{el}_{wall} = P_{eq} = \frac{P^{(el)}_{total}}{L_e} = \frac{1}{2} \sum_i^n w_i P(x_i) \tag{2.60}$$

as it can be seen with the shaded area in Figure 2.15(c). Lastly, Table 2.3 shows the position and weights of the $n = 2$ sampling points used in this work.

Table 2.3: Integration points for Gaussian quadrature rule in power density calculation.

| Sampling points | weights |
|---|---|
| $x'_1 = -\frac{1}{\sqrt{3}}$ | $w_1 = 1$ |
| $x'_2 = \frac{1}{\sqrt{3}}$ | $w_2 = 1$ |

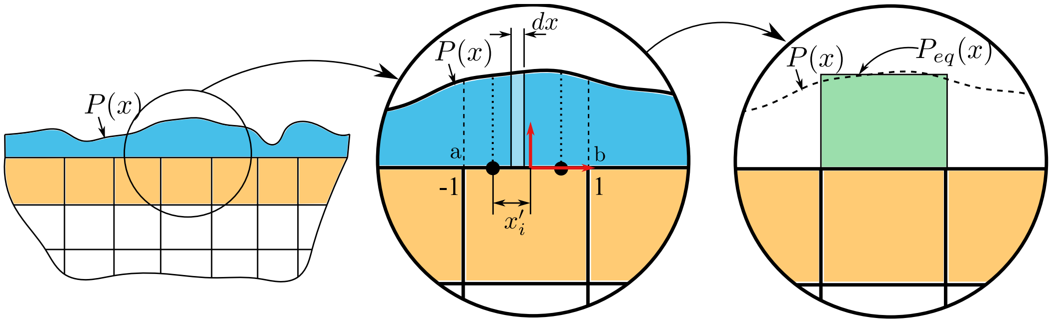
$P(x)$
$dx$
$P(x)$
a
b
-1
1
$x'_i$
$P(x)$
$P_{eq}(x)$

(a) (b) (c)

Figure 2.15: Power deposition on frontier elements for FE analysis.

### 2.3.4 Coupling of the Thermo-elastic model

The models described in subsection 2.3.1 and subsection 2.3.2 are solved as shown Figure 2.16.

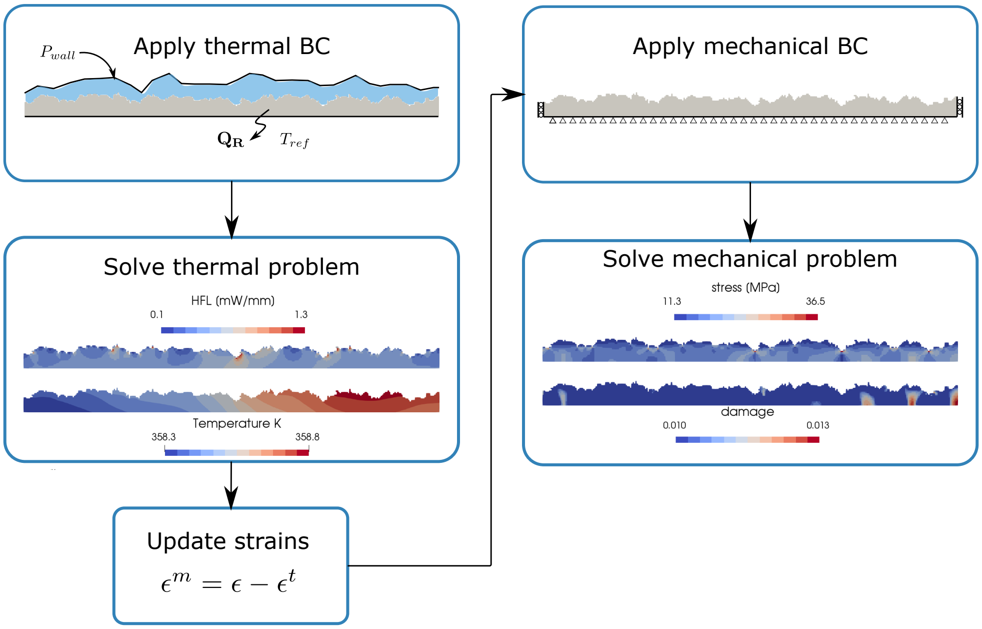
Apply thermal BC
$P_{wall}$
$\mathbf{Q_R}$
$T_{ref}$
Solve thermal problem
HFL (mW/mm)
0.1
1.3
Temperature K
358.3
358.8
Update strains
$\epsilon^m = \epsilon - \epsilon^t$
Apply mechanical BC
Solve mechanical problem
stress (MPa)
11.3
36.5
damage
0.010
0.013

Figure 2.16: Flowchart of the quasi-static analysis for thermo-mechanical problems.

At any time of the simulation $t$, the temperature field given by $T$ is calculated from the thermal problem as described in subsection 2.3.1. Due to this field, the body will tend to expand equally in all directions generating thermal strains $\epsilon^t_{kl} = \alpha_T \Delta T$ where $\alpha_T$ is the coefficient of thermal expansion. Recalling that the total strain tensor is given by,

$$\epsilon_{kl} = \epsilon_{kl}^{m} + \epsilon_{kl}^{t} \tag{2.61}$$

we calculate the mechanical part of the elastic strains $\epsilon_{kl}^{m}$, and we apply the mechanical boundary conditions given by Equation 2.52. Finally, we solve the mechanical problem described in subsection 2.3.2 to obtain the stresses in Equation 2.50.

# CHAPTER 3

# MATERIAL MODELS

## 3.1 Introduction

This chapter presents the material models used to solve the mechanical problem of the plasma-wall interaction model. In other words, these models are used to compute the stresses given by Equation 2.50 after the thermal problem is solved for the temperature field.

In section 3.2 we present a simple elastic material model that is governed by Hooke's Law of linear elasticity. This is followed by a Deshpande-Evans (DE) material behavior that is derived from the micromechanical behavior of ceramics in section 3.3. Next, the limitations of using an elastic or DE material behavior are presented by comparing the results with respect to a full FE model of a microstructure. Finally, section 3.5 presents a novel method to homogenize inelastic and history-dependent microstructures via Machine Learning (ML) that overcomes these limitations. We call the resulting material behavior the *Smart Constitutive Law* (SCL). In this formulation, there are no assumptions neither about the effective constitutive response of the microstructure nor the type of deformation it will be subjected to. This makes the integration of the SCLs into any standard FE solver identical to that of any traditional constitutive model. The details of the formulation are described in section 3.5.

## 3.2 Elastic material model

In this section, we assume an isotropic linear elastic material. Following Hooke's Law, the constitutive behavior is characterized by two constants, (i) the Young's modulus $E$ and (ii) the Poisson's ratio $\nu$. In this case the stress from Equation 2.50 becomes,

$$\sigma_{ij} = \lambda\epsilon_{kk}\delta_{ij} + 2G\epsilon_{ij}^{m} \tag{3.1}$$

with $\lambda = \frac{E\nu}{(1+\nu)(1-2\nu)}$ and $G = \frac{E}{2(1+\nu)}$, where $\epsilon_{kk}$ is the volumetric strain and $\delta_{ij}$, the Kronecker delta. Finally, the strain energy density is given by Equation 3.2,

$$w = w_0 = \frac{1}{2}\sigma_{ij}\epsilon_{ij}^{m} \tag{3.2}$$

### 3.3 Deshpande-Evans damage material model

In this section, we present a constitutive model derived to account for the inelastic deformation and micro-crack developing of ceramics that incorporates the microstructure behavior. The model was derived by Deshpande and Evans, and the complete and thorough derivation can be found in [34] since it is out of the scope of this work. Nevertheless, this section provides a summary of the approach. The model is based on an earlier approach to characterize the deformation of rocks [35]. Later enhancements include lattice plasticity to address the behavior post-failure of the specimen and the extension for a more general stress state and new crack growth law [36, 37]. For this case, the stresses from Equation 2.50 are calculated as

$$\sigma_{ij} = \mathbb{C}_{ijkl}\epsilon_{kl}^{m} \tag{3.3}$$

where $\mathbb{C}_{ijkl}$ is the fourth-order elasticity tensor and is calculated based on different *regimes* that depend on the interaction between the microcracks in the solid, as shown in Figure 3.1. A *damage* scalar parameter $D$ is defined to account for the crack sizes and orientation as

$$D = \frac{4}{3}\pi(l + \alpha a)^{3} f \tag{3.4}$$

where $l$ is the current crack size, $f$ the crack density per volume, $\alpha = \cos(\psi)$ and $\psi$ the orientation of the cracks. The model was derived assuming the most damaging crack orientation. Henceforth, the crack orientation is $\psi = 45°$. The *stress intensity factor* $K_I$ is obtained based on the local triaxiality of the stresses [34]. The triaxiality is defined as,

$$\Psi = \frac{\sigma_m}{\sigma_e} \tag{3.5}$$

where $\sigma_m = \sigma_{ii}/3$ is the hydrostatic stress, $\sigma_e = \sqrt{\frac{3}{2}\hat{\sigma}_{ij}\hat{\sigma}_{ij}}$ is the von Mises stress as a function of the deviatoric stress tensor $\hat{\sigma}_{ij} = \sigma_{ij} - \sigma_m\delta_{ij}$.

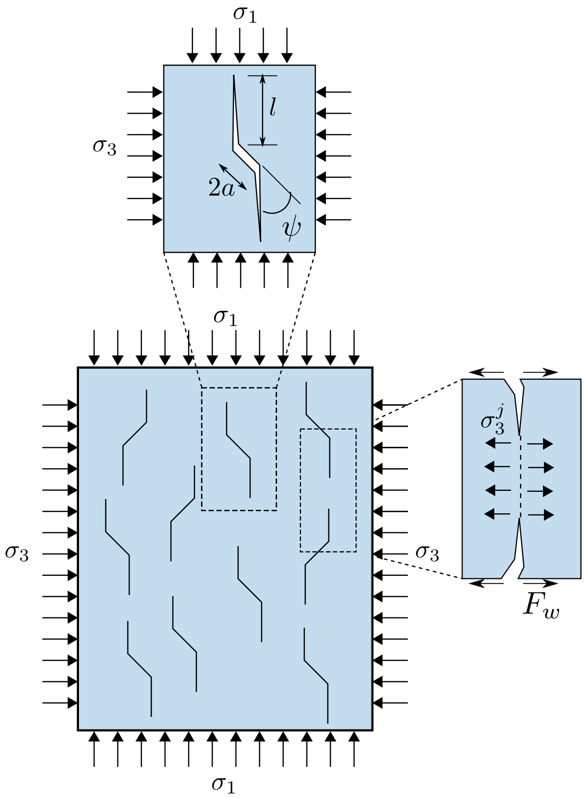

Figure 3.1: Wing microcracks distribution in a cracked solid [34].

As the solid is damaged, the size of the crack evolves with a *crack growth law* as a function of the $K_I$ and how rapid the load is applied. The crack growth rate is given by,

$$\dot{l} = \min\left[\dot{l}_0\left(\frac{K_I}{K_{IC}}\right)^m, \sqrt{\frac{G}{\rho_0}}\right] \tag{3.6}$$

and the evolution of the crack size is

$$l(t + \Delta t) = l(t) + \dot{l}\Delta t \tag{3.7}$$

where $K_{IC}$ is the mode I fracture toughness; $\dot{l}_0$ is a reference crack growth rate at $K_I = K_{IC}$; $m$ is a rate sensitivity exponent and $\Delta t$, the time increment. The shear wave speed $\sqrt{\frac{G}{\rho_0}}$ provides an upper bound of how fast the crack can grow, where $G$ and $\rho_0$ are the shear modulus and density of the uncracked solid. Finally, the *effective elasticity tensor* is calculated following an energy-based approach [38, 39], where the elastic strains $\epsilon_{ij}^{(e)}$ and the stresses $\sigma_{ij}$ are related through the strain energy density $w$ as

$$\epsilon_{ij}^{(e)} = \frac{\partial w}{\partial \sigma_{ij}} = T_1\delta_{ij} + T_2\sigma_{ij} \tag{3.8}$$

and the compliance tensor with

$$M_{ijkl} = \frac{\partial^2 w}{\partial \sigma_{ij}\partial \sigma_{kl}} \tag{3.9}$$

where $T_1$ and $T_2$ are constants that depend on the damage and the regime. Hence, the elasticity tensor is calculated as the inverse of the compliance tensor $M_{ijkl}$,

$$\mathbb{C}_{ijkl} = M_{ijkl}^{-1} \tag{3.10}$$

Although the model also accounts for plastic deformation, this work focuses on a simplified version in which the plasticity model is not used.

As mentioned above, the behavior is divided into three regimes as a function of the triaxiality (Equation 3.5) according to the following conditions,

$$\Psi < -\frac{B}{A} \qquad \text{Regime I} \tag{3.11a}$$

$$-\frac{B}{A} \leq \Psi < \frac{AB}{C^2 - F^2} \qquad \text{Regime II} \tag{3.11b}$$

$$\frac{AB}{C^2 - F^2} \leq \Psi \qquad \text{Regime III} \tag{3.11c}$$

where $A$, $B$, $C$ and $F$ are nonlinear functions of damage and friction defined in Appendix B.

**Regime I.** In this regime, there the cracks are closed. Hence, the stress intensity factor is $K_I = 0$, and the crack no longer propagates. Thus, the material exhibits elastic behavior. In this case, the strain energy is,

$$w = w_0 = \frac{1}{2\kappa}\sigma_m^2 + \frac{1}{6G}\sigma_e^2 \tag{3.12}$$

and the elastic strains are well known as,

$$\epsilon_{ij}^{(e)} = -\frac{3\nu}{2G(1+\nu)}\sigma_m\delta_{ij} + \frac{1}{2G}\sigma_{ij} \tag{3.13}$$

in which,

$$\begin{aligned} T_1 &= T_0^{(1)} = -\frac{3\nu}{2G(1+\nu)}\sigma_m \\ T_2 &= T_0^{(2)} = \frac{1}{2G} \end{aligned} \tag{3.14}$$

The elasticity tensor is,

$$C_{ijkl} = \frac{2G\nu}{1-2\nu}\delta_{ij}\delta_{kl} + 2G\delta_{ik}\delta_{jl} \tag{3.15}$$

Note that plugging Equation 3.15 in Equation 3.3 gives the same results as the elastic behavior of Equation 3.1.

**Regime II.** In this regime, the cracks are closed, and the loading is sufficient to cause relative sliding of the crack faces. Thus, the stress intensity factor is defined as

$$K_I = (A\sigma_m + B\sigma_e)\sqrt{\pi a} \tag{3.16}$$

where $a$ is the initial crack size (See Figure 3.1). The strain energy density is:

$$w = w_0 + \frac{\pi D_0}{4\alpha^3 G(1+\nu)}(A\sigma_m + B\sigma_e)^2 \tag{3.17}$$

where $D_0 = 4/3\pi(\alpha a)^3 f$ is the initial damage parameter assumed for the material. The first term corresponds to the strain energy as if the cracks were sealed, Equation 3.12, and the second term changes in strain energy density due to the cracks. Following Equation 3.8 the derivatives of the strain energy density defined in Equation 3.17 to obtain the elastic strains are,

$$\epsilon_{ij}^{(e)} = \frac{\partial w}{\partial \sigma_{ij}} = T_1\delta_{ij} + T_2\sigma_{ij}$$

where the nonlinear constants are obtained as

$$T_1 = T_0^{(1)} + T_{II}^{(1)} \tag{3.18}$$

$$T_2 = T_0^{(2)} + T_{II}^{(2)} \tag{3.19}$$

with

$$T_{II}^{(1)} = \frac{\pi D_0}{4\alpha^3 G(1+\nu)}\left[\frac{2}{3}A^2\sigma_m - 3B^2\sigma_m + \frac{2AB}{3}\sigma_e - 3AB\frac{\sigma_m^2}{\sigma_e}\right] \tag{3.20}$$

$$T_{II}^{(2)} = \frac{\pi D_0}{4\alpha^3 G(1+\nu)}\left[3B^2 + 3AB\frac{\sigma_m}{\sigma_e}\right] \tag{3.21}$$

and $T_0^{(1)}$ and $T_0^{(2)}$ are given by Equation 3.14. In the same fashion, the second derivative of $w$ with respect to the stresses provides the compliance tensor (Equation 3.9),

$$\begin{aligned} M_{ijkl} = & -\frac{\nu}{2(1+\nu)G}\delta_{ij}\delta_{kl} + \left[\frac{1}{2G} + 3\eta\left(B^2 + AB\frac{\sigma_m}{\sigma_e}\right)\right]\delta_{ki}\delta_{lj} \\ & + \eta\left[\left(\frac{2}{9}A^2 - B^2\right)\delta_{ij} + AB\frac{\hat{\sigma}_{ij}}{\sigma_e} - \frac{AB}{\sigma_e^2}\left(2\sigma_m\sigma_e\delta_{ij} - \frac{9}{2}\frac{\hat{\sigma}_{ij}}{\sigma_e}\sigma_m^2\right)\right]\delta_{kl} \\ & + \eta\frac{AB}{\sigma_e^2}\left(\sigma_e\delta_{ij} - \frac{9}{2}\frac{\hat{\sigma}_{ij}}{\sigma_e}\sigma_m\right)\sigma_{kl} \end{aligned} \tag{3.22}$$

where

$$\eta = \frac{\pi D_0}{4\alpha^3 G(1+\nu)}$$

Finally, the elasticity tensor is obtained as the inverse of the compliance tensor (Equation 3.10),

$$\mathbb{C}_{ijkl} = M_{ijkl}^{-1}$$

**Regime III.** In this regime, there is a loss of contact between the crack surfaces; thus, the stress intensity factor is

$$K_I = (C^2\sigma_m^2 + F^2\sigma_e^2)^{1/2}\sqrt{\pi a} \tag{3.23}$$

The strain energy density is given by

$$w = w_0 + \frac{\pi D_0}{4\alpha^3 G(1+\nu)}(C^2\sigma_m^2 + F^2\sigma_e^2) \tag{3.24}$$

and the elastic strains are

$$\epsilon_{ij}^{(e)} = \frac{\partial w}{\partial \sigma_{ij}} = T_1\delta_{ij} + T_2\sigma_{ij}$$

where for regime 3, the nonlinear constants are obtained as

$$T_1 = T_0^{(1)} + T_{III}^{(1)} \tag{3.25}$$

$$T_2 = T_0^{(2)} + T_{III}^{(2)} \tag{3.26}$$

with

$$T_{III}^{(1)} = \frac{\pi D_0}{4\alpha^3 G(1+\nu)} \left[\frac{2}{3}C^2 - 3E^2\right] \sigma_m \tag{3.27}$$

$$T_{III}^{(2)} = 3\frac{\pi D_0}{4\alpha^3 G(1+\nu)} F^2 \tag{3.28}$$

and $T_0^{(1)}$ and $T_0^{(2)}$ are given by Equation 3.14 and the compliance tensor (Equation 3.9) is,

$$M_{ijkl} = \left[-\frac{\nu}{2(1+\nu)G} + \eta\left(\frac{2}{9}C^2 - F^2\right)\right]\delta_{ij}\delta_{kl} + \left[\frac{1}{2G} + 3\eta F^2\right]\delta_{ki}\delta_{lj} \tag{3.29}$$

Finally, the elasticity tensor is obtained as the inverse of the compliance tensor (Equation 3.10),

$$\mathbb{C}_{ijkl} = M_{ijkl}^{-1}$$

To summarize, the strain energy density for the DE material model (from now on, *inelastic model*) is given by Equation 3.12, Equation 3.17 and Equation 3.24 depending on the material's behavior regime as discussed in section 3.3,

$$w = \begin{cases} w_0 & \text{Regime I, Equation 3.12} \\ w_0 + \frac{\pi D_0}{4\alpha^3 G(1+\nu)}(A\sigma_m + B\sigma_e)^2 & \text{Regime II, Equation 3.17} \\ w_0 + \frac{\pi D_0}{4\alpha^3 G(1+\nu)}(C^2\sigma_m^2 + F^2\sigma_e^2) & \text{Regime III, Equation 3.24} \end{cases}$$

### 3.4 Discussion - Scope and limitations of the elastic and DE constitutive models

Although the inelastic model defined in section 3.3 provides an enhancement with respect to the elastic model since it accounts for the non-linear behavior of the microstructure upon failure, it has some limitations because of the assumptions made to derive it. One of those assumptions is that the microstructure undergoes a stress state in which $\sigma_3 > \sigma_2 > \sigma_1$, and that $\sigma_2 = (\sigma_1 + \sigma_3)/2$. The first important observation here is that the model does

Table 3.1: Alumina properties.

| Parameter | Description | value |
|---|---|---|
| $E$ | Young's Modulus | 350.4 GPa [34] |
| $\nu$ | Poisson's ratio | 0.2 [34] |
| $\rho$ | Density | 3700 kg/m$^3$ [34] |
| $K_{Ic}$ | Fracture Toughness | 3 MPa m$^{1/2}$ [34] |
| $\sigma_c$ | Fracture strength | 477 MPa |
| $G_c$ | Fracture energy | 0.0247 mJ/mm$^2$ |
| $\delta_{max}$ | Maximum crack opening | $1.034\times10^{-4}$ mm |
| $E_{nn}$ | traction-displ. tangent | $2.5\times10^8$ MPa/mm |

not include shear stresses $\sigma_{12}$ in its derivation. Furthermore, the initial cracks are oriented to a preferred direction that makes the microstructure more compliant to some loading directions than others.

With several numerical experiments, we demonstrate that the inelastic model is not able to reproduce the behavior of a Representative Volume Element (RVE) of a microstructure that exhibits the same characteristics in terms of crack orientation, crack density, *etc*.

*Representative Volume Element of the microstructure*

The microstructure corresponds to Alumina ceramic, where its properties are tabulated in Table 3.1. This material is chosen such that we can use it as a benchmark to compare the behavior of a RVE of the microstructure obtained from a FE analysis and the inelastic constitutive model.

The size of the RVE is selected in order to preserve the crack density ($f = 1000$ 1/mm$^3$) for the material. For the 2D case analyzed in this work, the crack density per unit area is $N_a = 100$ 1/mm$^2$. Therefore, for the RVE size of 376 $\mu$m, as shown in Figure 3.2, 14 cracks of 38 $\mu$m are randomly placed at $\pm45°$ where the size $d$ of the cracks and their orientation are defined as in [34]. In order to simplify the calculations, we allow the cracks to growth following the path of cohesive zones shown in Figure 3.2. That is, each crack tip can grow at $0°, \pm45°, \pm90°, \pm135°, 180°$. The mesh is generated using MicroStructPy [40].

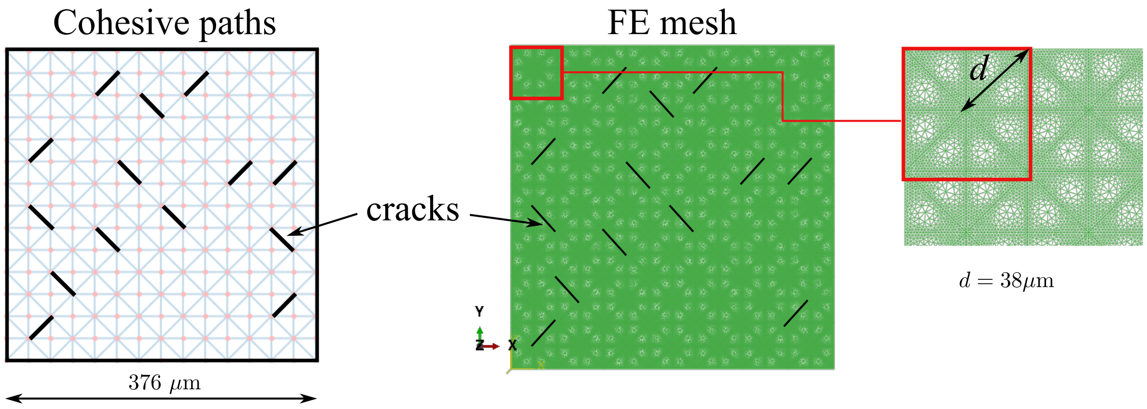

Figure 3.2: RVE of the microstructure with the cohesive element path for crack growth, the cracks location and the FE mesh.

*Cohesive zone modeling for crack evolution*

For the given fracture toughness $K_{Ic}$, the value of the cohesive strength $\sigma_c$ is chosen so that the cohesive zone length $l_c$ is resolved by the mesh [41]. Therefore, $\sigma_c = \sqrt{K_{Ic}^2(1-\nu^2)/l_c}$ where $\nu$ is the Poisson's ratio. In this work, we use a cohesive-zone length in the order of the crack size $l_c = d = 38\mu$m. The element discretization of the cohesive path is such that it allows more than 20 elements per cohesive length $l_e < l_d/20$.

The cohesive path shown in Figure 3.2 is defined using the built-in cohesive elements from the Abaqus library [42]. We use an *intrinsic cohesive zone model* in which the cohesive elements are embedded before the simulation begins [43]. Thus, an initial (artificial) elastic range is required for the constitutive relationship, as shown in Figure 3.3. The unloading condition is assumed linear to the origin upon reaching an opening $\delta > \delta_c$. The maximum opening $\delta_{max}$ is obtained considering the fracture energy given by the area under the TSL curve, $\delta_{max} = 2\frac{G_c}{\sigma_c}$ where $G_c$ is related to the fracture toughness through $G_c = K_{Ic}^2(1-\nu^2)/E$ for a plane strain case [41].

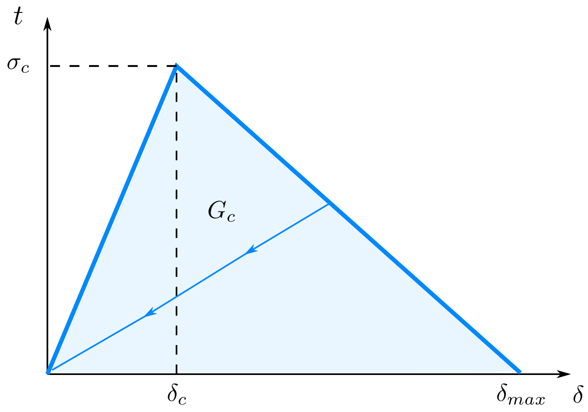

Figure 3.3: Bi-linear traction separation law.

Finally, the critical opening is defined such that the slope $E_{nn} = \sigma_c/\delta_c \to \infty$ without adding numerical instabilities. In practice, we use $E_{nn} = 10\sigma_c/\delta_c^*$ where $\delta_c^*$ is obtained from a typical power law as $\delta_c^* = G_c/(e\sigma_c)$ [41, 44]. The adopted values of $\sigma_c, G_c, \delta_{max}$, and $E_{nn}$ are tabulated in Table 3.1.

*Comparison with the inelastic model*

The RVE of the microstructure is subjected to a series of loading cases in order to characterize its behavior and to assess the capabilities of the inelastic constitutive model (defined in section 3.3). The first case considers a uniaxial stress ($\sigma_{22} \neq 0, \sigma_{ij} = 0$) that closely resembles the assumptions of the inelastic model [34]. As a result, it can be seen in Figure 3.4(a) that the inelastic model is able to capture really well the average (or effective) behavior of the microstructure, reaching the same maximum stress before full damage. In Figure 3.4(b), a uniaxial compressive strain ($\epsilon_{22} \neq 0, \epsilon_{ij} = 0$) is applied, and due to the high confining pressure given by the boundary conditions, there is no damage whatsoever to the microstructure, which is perfectly captured by the inelastic model, and they are both equal to an elastic case. However, under a pure shear case ($\epsilon_{12} \neq 0, \epsilon_{ij} = 0$); the microstructure exhibits several stages of damage (as seen by the jagged curve of Figure 3.4(c)) but it still has some load bearing capacity, whereas the inelastic model, not only shows a premature failure point, but also it lacks any load bearing capacity upon failure. The elastic model overestimates the real behavior of the microstructure as it is expected.

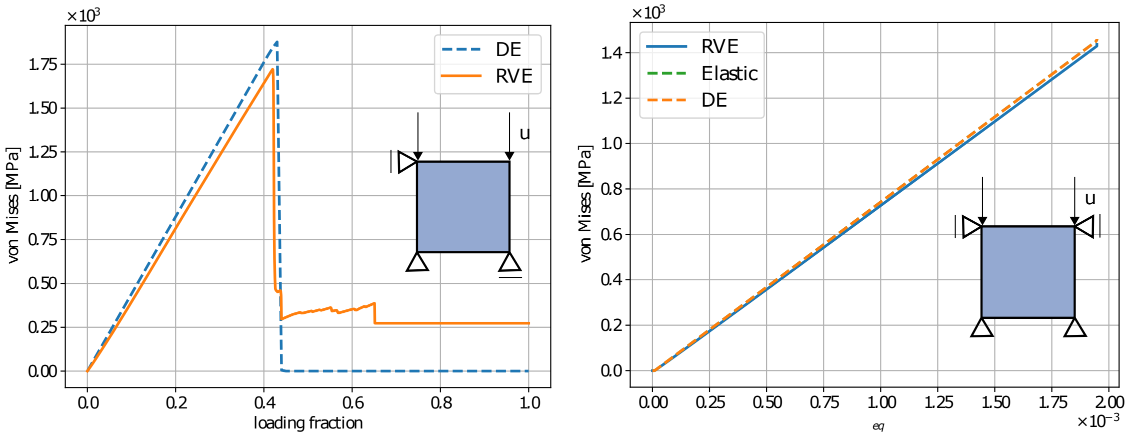

(a) Uniaxial stress

(b) Uniaxial strain

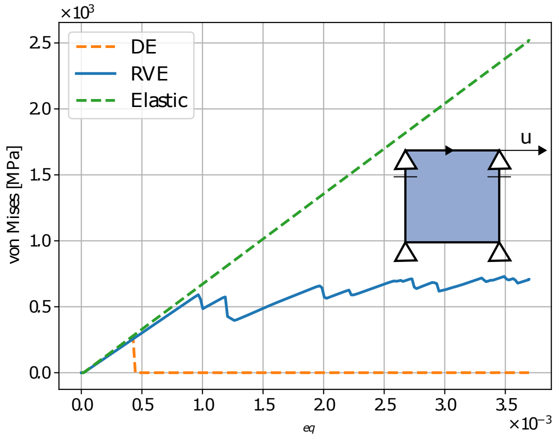

(c) Pure shear

Figure 3.4: Comparison of equivalent stresses from numerical homogenization of the RVE and the inelastic ceramic constitutive law defined in section 3.3 for (a) uniaxial stress case, (b) uniaxial strain case and (c) pure shear case.

A more interesting case is the use of a random load scenario to which the microstructure can be exposed to. In Figure 3.5 we show the behavior of the RVE, an elastic case, and the inelastic model, under one random macro-strain history. We generate a strain history with and without the shear component, as shown in Figure 3.5(a) in order to show how the inelastic model deviates from the behavior of the microstructure when shear strains are present. At the beginning of the loading scenario, all three models reproduce the same behavior (since the microstructure is still under elastic regime), as can be seen from Figure 3.5(b). As the load increment progresses, the inelastic model resembles the behavior of the RVE for the case without shear, although it is still not accurate. This result is worsened if the shear strain is considered (Figure 3.5(b,right)) since the inelastic model is unable to carry more load upon failure. This represents a significant limitation given that the shear strains cannot be neglected in the general case.

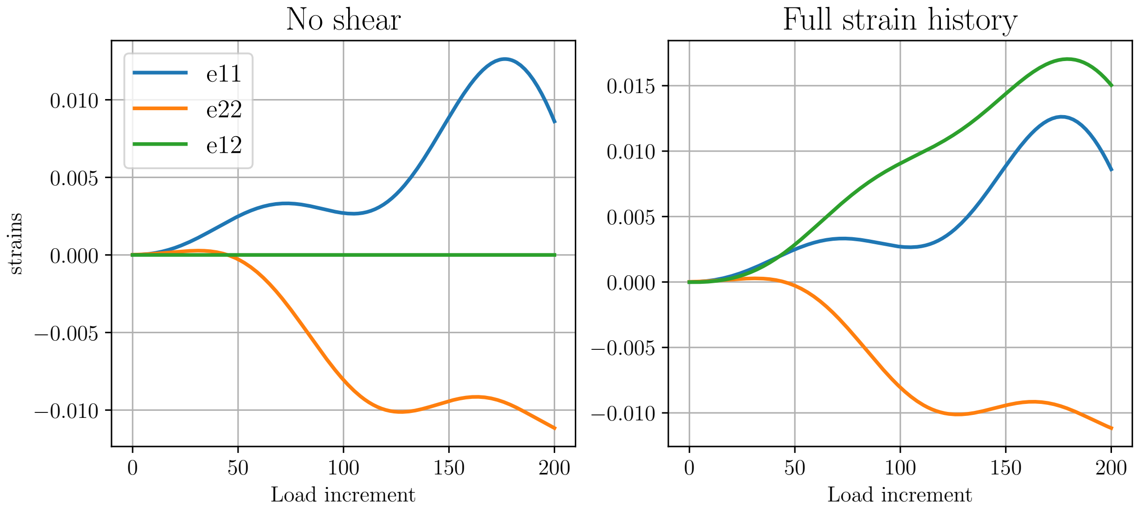

(a) Macro strains

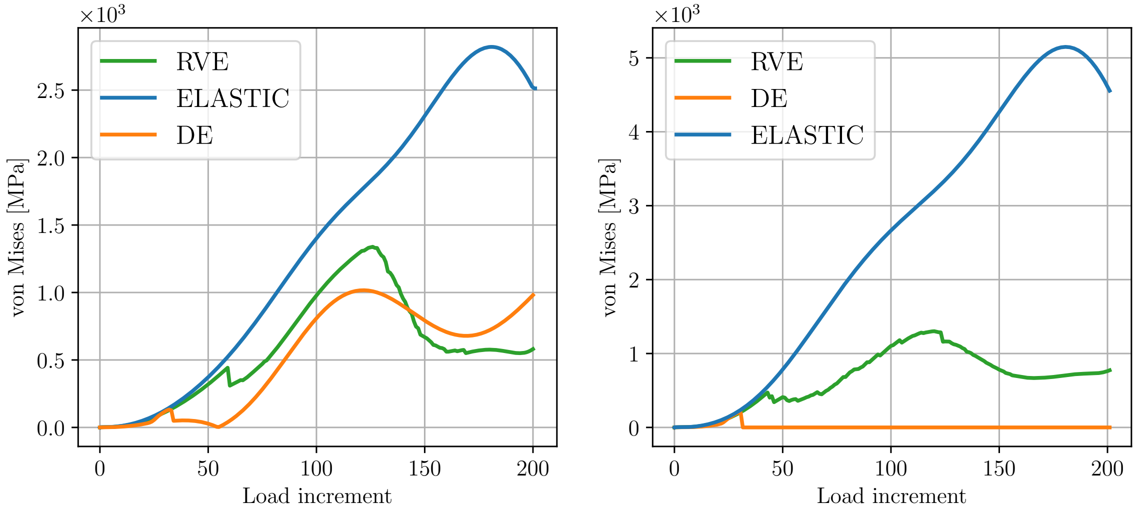

(b) Effective stress

Figure 3.5: (a) Macro-strains for a Gaussian Process. The figure to the left shows a case without shear strain ($\epsilon_{12} = 0$), whereas the full strain history is shown to the right. (b) Effective equivalent stress as a function of the load increment for the no shear case (left) and full history (right). The three models are (1) an elastic material model, (2) the FE of the RVE of the microstructure, and (3) the inelastic constitutive law from section 3.3.

## 3.5 Data-driven material model

This section focuses on the homogenization of inelastic and history-dependent microstructures via machine learning. In this work we extend recently introduced machine-learning enabled *smart finite elements* [45] and formulate *smart constitutive laws* (SCLs) for the homogenization of inelastic microstructures.

Numerical homogenization has gained attention throughout the years as the numerical power of computers greatly increased. In particular, the use of machine learning (ML) to obtain the effective behavior of microstructures is becoming very popular, as described in [28]. In this case, we propose to obtain the effective stresses from Equation 2.50 via machine learning. In this section, the stress tensor given by Equation 2.50 is a nonlinear and history dependent function of the mechanical strains $\epsilon_{kl}^m$ and the internal state variables of the microstructure $\eta$ rather than just a function of the strains through the elasticity tensor $\mathbb{C}_{ijkl}$ as for the elastic or inelastic material models in section 3.2 and section 3.3. The internal state variables $\eta$ are associated with dissipative phenomena, *e.g.*, equivalent plastic strain $\epsilon_P$ or damage $d$.

Because the stiffness matrix $\mathbf{K}$ cannot be formed as in subsection 2.3.2 (since $\mathbb{C}_{ijkl}$ is not defined), the equation of conservation of linear momentum results

$$f_{ext}{}_i^I - f_{int}{}_i^I = 0 \qquad \text{or} \qquad \mathbf{f_{ext}} - \mathbf{f_{int}} = \mathbf{0} \tag{3.30}$$

with internal forces and external forces given by,

$$f_{int}{}_i^I = \int_\Omega \frac{\partial h_I}{\partial x_j} \sigma_{ij} d\Omega \tag{3.31}$$

$$f_{ext}{}_i^I = \int_\Omega h_I \rho b_i d\Omega + \int_{\partial\Omega_t} h_I t_i^* d\partial\Omega_t \tag{3.32}$$

It is clear from the previous discrete equations that a key aspect needed to solve the stress analysis problem is to find an accurate representation of stresses $\sigma_{ij}$, which is usually referred to as the constitutive model. There are plenty of well-established constitutive models for a large variety of material behaviors, *e.g.*, Hooke's Law (as described in section 3.2), J2 plasticity theory [46], porous plasticity [47], microcracks in ceramics [34] (as described in section 3.3) to name a few. However, as mentioned in the introduction, it is very challenging to find efficient and accurate homogenization schemes able to provide such constitutive models for materials with microstructures that result in inelastic responses at this scale. The following section described an approach to homogenize arbitrary microstructures and obtain the corresponding nonlinear and history-dependent constitutive response.

### 3.5.1 Homogenizing inelastic behavior via Machine Learning

First, consider the problem of homogenizing an RVE to obtain its effective constitutive law, represented by Equation 2.50, $\sigma_{ij} = \underline{\underline{\sigma}}\left(\epsilon^m_{km}, \eta\right)$, in the previous chapter. Let us assume that the microstructure of the RVE is such that it might result in an effective inelastic response. The simplest explanation of this approach is that, given an adequate number of experiments (numerical in this work, but the approach is not restricted to this case only) for which the deformation history applied to the RVE and the corresponding stress history are given, a ML technique can be utilized to generate a surrogate model representing the constitutive law, see Figure 3.6. This also requires a new strategy to tackle history-dependent problems. When the RVE is considered, for any given macro strain, the stress distribution in the fine-scale model will depend on the complete history of the deformation, and for any given input strain, multiple equivalent stresses are possible. The solution proposed in this work consists on adopting sequence-to-sequence ML models so that all the immediately available information can be contemplated, which in a mechanical problem is the deformation history. The ML model is then responsible for defining what part of that information is relevant. Note that in this approach, only the strain and stress histories are required, but no other quantities implying a specific material behavior are needed for the input, e.g, plastic strain, damage, *etc*. This surrogate ML-based model is named a *smart constitutive* *law* (SCL).

More specifically, the SCL is built through a process involving two main stages: the first one generates various strain and stress histories for the RVE, as depicted in the upper portion of Figure 3.6. This collection of strain-stress histories represents the training set. Each element of the training set consists of two sequences: one containing the strain history and the other one containing the stress history for the RVE. In the second stage, the training set is utilized for training the SCL, as depicted in the lower portion of Figure 3.6. Since the elements of the training set are pairs of strain-stress histories, the ML method of choice must be able to relate sequences and not just individual values.

The first stage involves the following operations:

1. Generation of a full strain history, given by the evolution of the strain tensor $\epsilon_{ij}$ with time.

2. Finite Element analysis of the RVE under the prescribed strain history generated in the previous point to obtain the full history for the stress tensor $\sigma_{ij}$ and other quantities of interest, *e.g.*, localized indicators of failure at lower scales such as the maximum equivalent plastic strain over the RVE. Note that these quantities of interest are not part of the input, so they do not influence the prediction of stress.

By following the previous points, only generates one data point of the training set, that is, one strain sequence and its corresponding stress sequence. Note that each entry in the input (strain) and output (stress) sequences are full tensors. This process must be repeated as many times as necessary to build a *training set* that corresponds to the inputs (strains) and outputs (stresses plus localized information) that will be used to train the model.

The second stage involves the following operations:

1. Definition of the *SCL model architecture*, which in this work case consists of a RNN with time-history prediction capability. RNNs are chosen because of their ability to relate sequences.

2. Training the RNN to finally produce the SCL.

In this work, the model is trained using the Keras module for Python [48], by combining the *training set* and the *SCL model architecture*. Training involves an iterative process in which the internal parameters of the network are adjusted or *trained* to minimize a *loss function*, which represents, for a given input sequence, the error between the output sequence generated by the RNN and the true output sequence in the training set. It is key in this stage to find the best set of internal parameters of the RNN, which can be achieved via different optimization techniques. In general, the process is repeated over several iterations (*epochs*), to reduce the loss function until after an acceptable value is obtained, as shown in the "training statistics" of Figure 3.6.

In the next section, we provide more details about the generation of training cases and the process to define and train the SCL, respectively.

### *Generation of input strain sequences via Gaussian Processes*

The input space consists of strain sequences representing loading histories applied to the RVE. One approach prevalent in the literature is to utilize selected canonical loading scenarios, *e.g.*, uniaxial strain, pure shear, volumetric deformation, etc. However, this approach requires a priori knowledge about the material response, *e.g.*, assuming that any loading path outside the training set will be an interpolation of those canonical cases. This defeats the purpose of the application, since the goal is to be able to generate an SCL in the most systematic manner without making any assumptions about the material response.

This approach uses the fact that every possible loading scenario applied to the RVE can be described in terms of the invariants of the strain tensor. Hence, the principal strains $\epsilon_1$, $\epsilon_2$ and the orientation corresponding to the largest principal strain $\theta$ are used as a basis of three independent quantities to create the input sequences of the training cases $(\epsilon_1(t), \epsilon_2(t), \theta(t)) = \{(\epsilon_1, \epsilon_2) \in \mathbb{R}^2, \theta \in \mathbb{R} \quad | \quad \epsilon_{min} < \epsilon_1, \epsilon_2 < \epsilon_{max}, \theta_{min} < \theta < \theta_{max}\}$. Moreover, because in a physical loading scenario the sequence of strains should be contin-

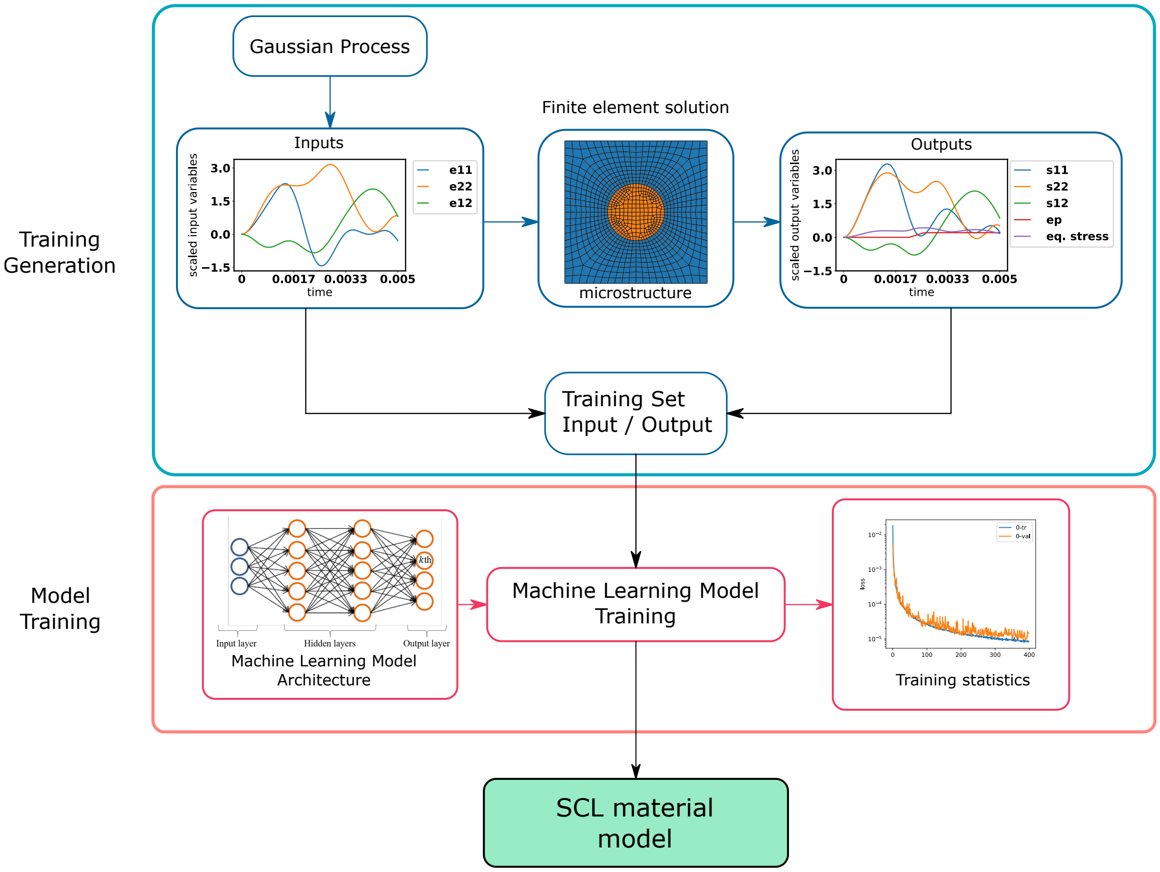
Training Generation
Gaussian Process
Inputs
scaled input variables
3.0
1.5
0.0
−1.5
0
0.0017
0.0033
0.005
time
e11
e22
e12
Finite element solution
microstructure
Outputs
scaled output variables
3.0
1.5
0.0
−1.5
0
0.0017
0.0033
0.005
time
s11
s22
s12
ep
eq. stress
Training Set
Input / Output
Model Training
Input layer
Hidden layers
Output layer
Machine Learning Model
Architecture
Machine Learning Model
Training
loss
0-tr
0-val
0
100
200
300
400
Training statistics
SCL material
model

Figure 3.6: Overview of the proposed approach to build a generic data-driven material model.

uous and smooth, Gaussian Processes(GP) are employed to generate them [49]. Gaussian Processes are a *collection of random variables, with a joint Gaussian distribution*[50] that can be specified by their mean function, $m(z)$, and covariance function *kernel*, $\kappa(z, z')$

$$f(z) \sim GP\left(m(z), \kappa(z, z')\right)$$

Thus, the smoothness of the generated sequence can be controlled by specifying the mean and kernel. The mean is defined as zero, and also it is assumed that the specimen has no residual stresses or strains at the beginning of the process, *i.e.*, $\epsilon_{ij} = 0$ at $t = 0$. Next, the kernel needs to be specified. For this purpose, the requirement that the process is continuous and differentiable at each point (smooth) is enforced. For the problem considered here, the Radial Basis Function (RBF) described by Equation 3.33 is used. For this function, two data points of variable $z$, $z_k$ and $z_l$, are correlated only through the distance that separates them in the sequence [50],

$$k(z_k, z_l) = s^2 \text{exp}\left(-\frac{|z_k - z_l|^2}{2l_s^2}\right) \tag{3.33}$$

where $l_s$ corresponds to the characteristic length of the process and $s$ is the overall variance or amplitude. The covariance matrix is then defined as

$$\Sigma_{kl} = k(z_k, z_l) \tag{3.34}$$

Then the sequences are generated for each variable of interest from a random multivariate Gaussian distribution $\mathcal{N}(\mathbf{0}, \mathbf{\Sigma})$ using this covariance matrix with a defined sequence length [50]. More precisely, we use the kernel to create the three independent variables of the training set: the principal strains $\epsilon_1, \epsilon_2$, and the orientation with respect to the Cartesian axis, $\theta$. This work contemplates (1) the amplitude for principal strains within $0 < s_\epsilon < s_{\epsilon M}$, (2) the angle range for principal directions within $0 < s_\theta < s_{\theta M}$, (3) the characteristic length within $T/10 < t < T/2$ with $T$ being the length of the loading sequence, and (4) the initial principal direction within $-\pi < \theta_0 < \pi$.

As a result, sequences of principal strains $\epsilon_1(t)$, $\epsilon_2(t)$, and the orientation angle $\theta(t)$ are generated. Figure 3.7(a) shows two sequences of principal strains $\epsilon_1(t)$ and $\epsilon_2(t)$, which evolve following a Gaussian Process. Figure 3.7(b) shows the same sequences but is now in the plane of principal strains. Here we can visualize the loading path in such a plane. Note that this path represents just one realization (one entry in the training set) where each pair of principal strains at time $t$ corresponds to one point in the plane of principal strains. It is worth noting that, even though we call $t$ time, it just represents a counter of the loading process. As it can be seen from the figure, the generated variables are random with different characteristic lengths and amplitudes yet smooth as one would expect on an arbitrary loading scenario. Figure 3.7(c) depicts ten realizations of such evolution of principal strains $\epsilon_1$ and $\epsilon_2$. Finally, Figure 3.7(d) shows the evolution of the corresponding orientation angle $\theta$ for each realization.

For this work, 10,000 loading sequences are generated [28]. The distribution of principal strains for all sequences combined can be seen in Figure 3.8. In this plot, the histogram shows how many times the pairs $(\epsilon_1, \epsilon_2)$ are included in the dataset from all the generated sequences, giving us an idea of how well the invariant space is covered. As it can be seen, the joint distribution covers the plane of principal strains with the desired interval $\epsilon_1, \epsilon_2 \in (-0.03, 0.03)$, slightly favoring cases for which $|\epsilon_{max}/\epsilon_{min}| > 1$. In other words, our sampling is slightly biased towards deviatoric cases rather than volumetric ones (where $|\epsilon_{max}/\epsilon_{min}| \to 1$).

Since the outputs of the training cases (stresses and localized information) are obtained with the FE analysis of the RVE, the strain components need to be rewritten in the Cartesian coordinate system. The transformation is performed by a rotation from the strains in the principal directions to the Cartesian components, $\epsilon_{11}, \epsilon_{22}, \epsilon_{12}$ using Equation 3.35,

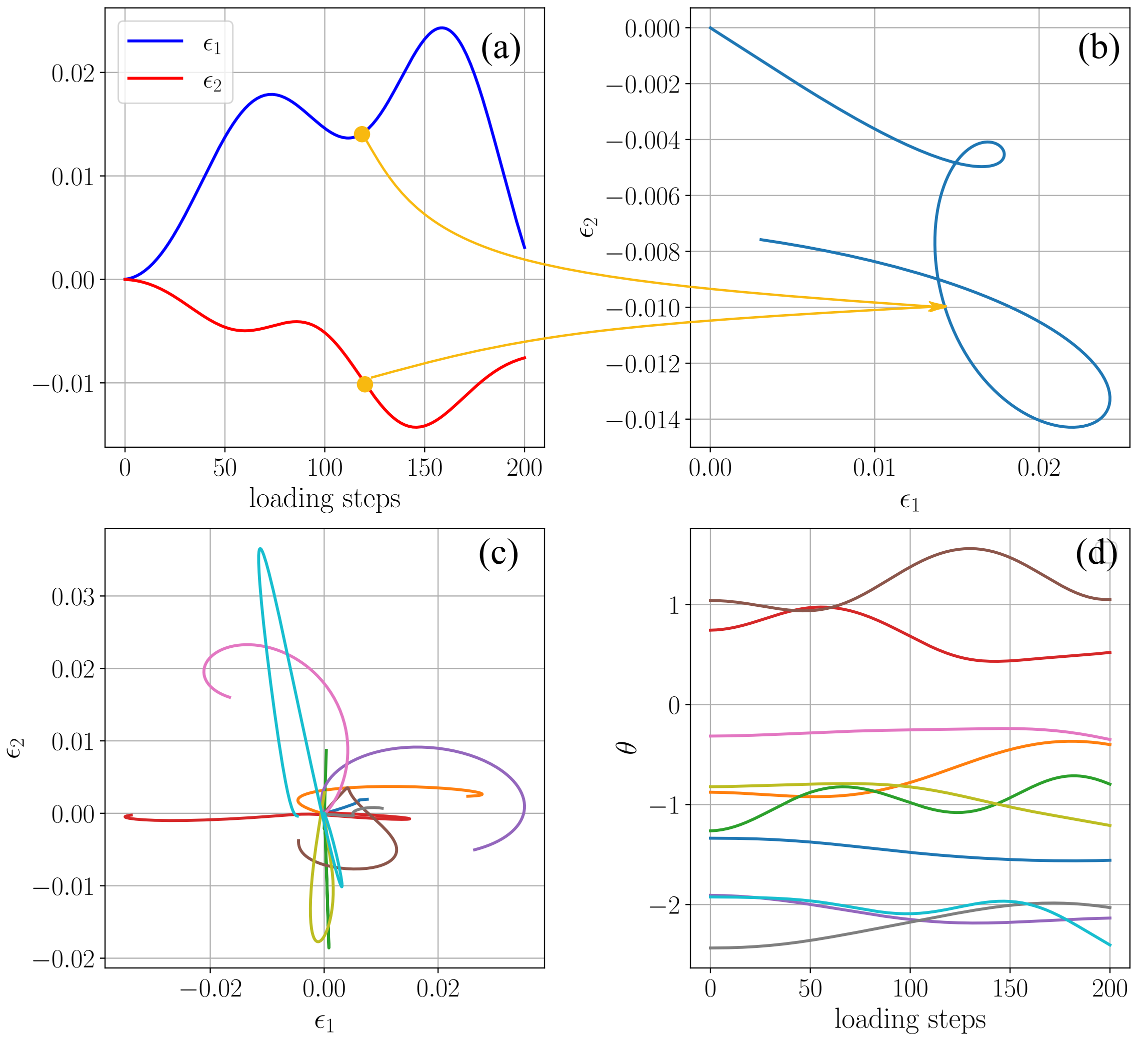

Figure 3.7: Generation of strain histories (sequences) for the training set.

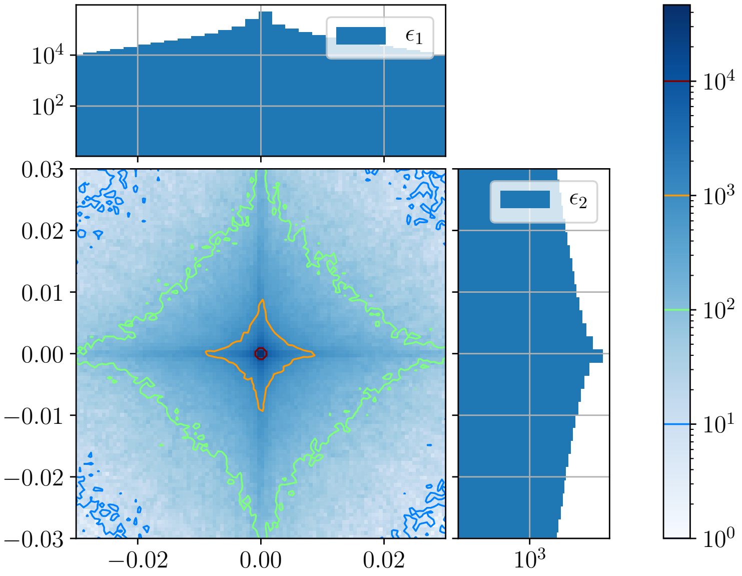

Figure 3.8: Joint distribution for principal strains, as in [28].

$$
\begin{aligned}
\epsilon_{11} &= (\epsilon_1 - \epsilon_2)\cos^2\theta + \epsilon_2 \\
\epsilon_{22} &= (\epsilon_2 - \epsilon_1)\cos^2\theta + \epsilon_1 \\
\epsilon_{12} &= (\epsilon_1 - \epsilon_2)\sin\theta\cos\theta
\end{aligned}
\tag{3.35}
$$

*Generation of output variables from the homogenized response of the RVE*

For each of these input sequences (strain histories), the corresponding output of sequence $\mathbf{y}(t)$ is obtained by solving the boundary value problem for the microstructure and extracting the average stresses over the domain and any other quantity of interest, *e.g.*, localized information.

To obtain the output variables needed for the training set, a FE simulation on the RVE of the microstructure is performed for a total of $n = 10,000$ observations of strains inputs $\epsilon_{ij}(t)$ generated with Gaussian Processes as explained in subsubsection 3.5.1. That is, the inputs of our training set consist of 10,000 sequences of strains, each sequence having 200 loading steps. The strains are used to impose affine displacement boundary conditions in

$\partial\Omega_u$ following Equation 3.36,

$$u_i^J = \begin{bmatrix} \epsilon_{11}(t) & \epsilon_{12}(t) \\ \epsilon_{12}(t) & \epsilon_{22}(t) \end{bmatrix} \begin{bmatrix} x_1^J \\ x_2^J \end{bmatrix} \tag{3.36}$$

where $x_i^J$ corresponds to the i-$th$ coordinate component of the J-$th$ node of the boundary.

A total of 10,000 FE simulations are performed in order to solve the boundary value problem of the microstructure for each of the 10,000 strain sequences. This consists of solving the same equations defined in subsection 2.3.2 for the RVE, assigning each subdomain of the microstructure the corresponding constitutive law, for example, if the RVE is composed of different material behaviors. From each simulation, the full field solution is recovered. From this, the average stress of the microstructure can be extracted as,

$$\bar{\sigma}_{ij}(t) = \frac{1}{\sum_e^{N_e^{(\text{RVE})}} \det J^{(e)}} \sum_e^{N_e^{(\text{RVE})}} \sigma_{ij}^{(e)}(t) \det J^{(e)} \tag{3.37}$$

where $e$ indicates the element, $\det J^{(e)}$ the Jacobian of each element of the microstructure; $\bar{\sigma}_{ij}(t)$ the average of each stress component. Also, $\sigma_{ij}^{(e)}(t)$ represent the stress components of each element on the microstructure.

In summary, at this point, we have a training set $\mathcal{D}$ of $n$ observations,

$$\mathcal{D} = (\epsilon(t)_i, \mathbf{y}(t)_i) \quad i = 1, 2, ..., n \tag{3.38}$$

where

$$\epsilon(t) = \{\epsilon_{11}(t), \epsilon_{22}(t), \epsilon_{12}(t)\}$$

denotes the input vector of strains as a function of loading step $t$ and

$$\mathbf{y}(t) = \{\bar{\sigma}_{11}(t), \bar{\sigma}_{22}(t), \bar{\sigma}_{12}(t)\}$$

denotes the output vector of averaged stresses as a function of loading obtained from the detailed FE analysis of the RVE. For the purposes of this work, a training set consisting of 10,000 input-output pairs is created, each of which contains information pertaining to 200 loading steps.

### 3.5.2 Training the machine learning model

To be able to address any possible path-dependency, RNN is used as shown schematically in Figure 3.9. In particular, this work focuses on one of the many possible variations of the RNN called *Long Short-Term Memory* (LSTM) developed to handle sequence-to-sequence data and to address the vanishing gradient effect present in long sequences [51]. LSTM networks have a dedicated memory cell whose information is controlled by a number of gates. Those gates have weights that allow the model to learn how to control the flow of information in and out of the memory. Training an RNN is similar to feed-forward neural networks, except that each sample consists of a sequence of vectors for the input and output. In this particular configuration, the information at previous times of the sequence $t_n, n = 0, 1, \ldots, j-1$ is retained to be weighted for the inputs at time $t_j$. This work uses the version of the model implemented in the Python module *Keras* [48], and a mean squared error to define the loss function $E_{\text{MSE}}$ of the model during training,

$$E_{\text{MSE}} = \frac{1}{n} \sum_{d \in \mathcal{D}} (\hat{\mathbf{y}}_d^* - \mathbf{y}_d^*)^2 \tag{3.39}$$

where $\hat{\mathbf{y}}_d^*$ and $\mathbf{y}_d^*$ correspond to the predicted value of the network and the targeted output of the current training case $d$, respectively and $n$ is the total amount of training cases. It should be noted here that, before being utilized for training, each feature of the data is normalized

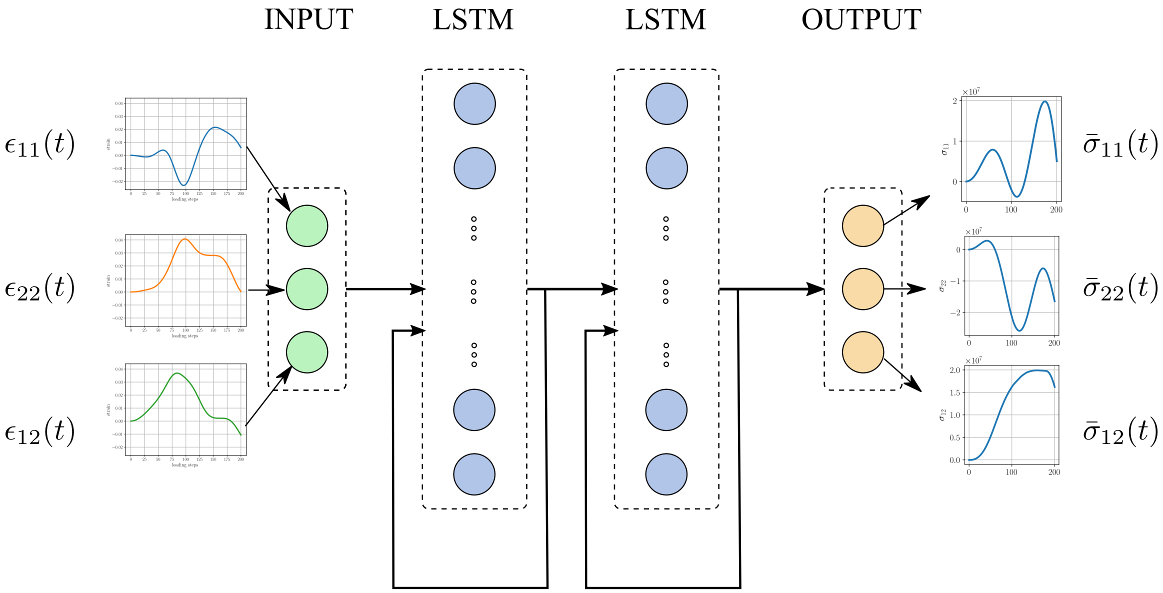

Figure 3.9: Machine learning model schematics. The input layer corresponds to three nodes, one for each strain component, $\epsilon_{11}, \epsilon_{22}, \epsilon_{12}$; the hidden layers are LSTM layers, and the output layer has three units, one for each stress output, $\sigma_{11}, \sigma_{22}, \sigma_{12}$.

with the corresponding standard deviation (inputs $\epsilon(t)$, and outputs $\mathbf{y}$) as follows[1],

$$\epsilon_k^*(t) = \frac{\epsilon_k(t)}{s_k^{(inputs)}} \tag{3.40}$$

$$y_i^*(t) = \frac{y_i(t)}{s_i^{(outputs)}} \tag{3.41}$$

where $\epsilon_k(t)$, $y_i(t)$ are the input and output sets respectively, and $s_k^{(inputs)}$, $s_i^{(outputs)}$ the corresponding standard deviation per feature of inputs ($k = \epsilon_{11}, \epsilon_{22}, \epsilon_{12}$) and outputs ($i = \sigma_{11}, \sigma_{22}, \sigma_{12}, \epsilon_p^*, \sigma_{vm}^*$). The initialization of the RNN parameters is set as default. The loss $E_{\text{MSE}}$ is minimized with the back-propagation algorithm through time (BPTT) [52] to modify the internal parameters of the network which produce the mapping function that best fit the given normalized data. The BPTT algorithm relies on the unrolling of the network, in which a copy is generated for each time increment allowing to the use of a traditional back-propagation algorithm on the unrolled network.

During training, the generated cases are split in two: one portion, called *training split*, is used to train the model, while the other portion, called *validation split*, is used to validate the current state of the net. In this work, 80% of the cases are used to train and 20% to validate. The number of training cases as well as the architecture are obtained with a sensitivity analysis as discussed in [28].

---

[1] No summation performed here

In order to reduce oscillations while predicting the stress tensor, we use a *transfer learning* approach that is widely used in other fields such as text comprehension and translation, image classification, health screening, among many others [53, 54, 55]. In this approach, (1) we first train **all the hyperparameters** linking the Input, LSTMs, and Output layers of the SCL using the regular mean squared error,

$$MSE = \frac{1}{N_s} \sum_{s}^{N_s} \left[ \frac{1}{N} \sum_{i}^{N} (\hat{y}_i^s - y_i^s)^2 \right] \tag{3.42}$$

where $N_s$ is the number of samples (10,000), $N$ total number of load increment (200), and $\hat{y}_i^s, y_i^s$ are the predicted and true value of the output at increment $i$ of sample $s$[2] as depicted in Figure 3.10(a). After the first training process concludes, (2) we define a new loss function that accounts for the tangent stiffness of the system to reduce the oscillations of the predictions in order to make the solution more stable,

$$KMSE = \frac{1}{N_s} \sum_{s}^{N_s} \left[ \frac{1}{N} \sum_{i}^{N} \underbrace{\left\| \left( \frac{\Delta\hat{\sigma}_{jk}}{\Delta\epsilon_{lm}} - \frac{\Delta\sigma_{jk}}{\Delta\epsilon_{lm}} \right) \right\|_2}_{||\Delta K||_2} \right] \tag{3.43}$$

with

$$||\Delta K||_2 = \left[ \sum_{p} \sum_{q} \left( \hat{K}_{pq} - K_{pq} \right)^2 \right]^{\frac{1}{2}} \tag{3.44}$$

---

[2] As before, $\hat{y}_i^s$ and $y_i^s$ are the normalized output using Equation 3.41.

and

$$K_{pq} = \frac{\Delta\sigma_{jk}}{\Delta\epsilon_{lm}} = \begin{bmatrix} \frac{\Delta\sigma_{11}}{\epsilon_{11}} & \frac{\Delta\sigma_{11}}{\epsilon_{22}} & \frac{\Delta\sigma_{11}}{\epsilon_{12}} & \frac{\Delta\sigma_{11}}{\epsilon_{21}} \\ \frac{\Delta\sigma_{22}}{\epsilon_{11}} & \frac{\Delta\sigma_{22}}{\epsilon_{22}} & \frac{\Delta\sigma_{22}}{\epsilon_{12}} & \frac{\Delta\sigma_{22}}{\epsilon_{21}} \\ \frac{\Delta\sigma_{12}}{\epsilon_{11}} & \frac{\Delta\sigma_{12}}{\epsilon_{22}} & \frac{\Delta\sigma_{12}}{\epsilon_{12}} & \frac{\Delta\sigma_{12}}{\epsilon_{21}} \\ \frac{\Delta\sigma_{21}}{\epsilon_{11}} & \frac{\Delta\sigma_{21}}{\epsilon_{22}} & \frac{\Delta\sigma_{21}}{\epsilon_{12}} & \frac{\Delta\sigma_{21}}{\epsilon_{21}} \end{bmatrix} \tag{3.45}$$

where Equation 3.45 is calculated for both the predicted $\hat{K}_{pq}$ and the real values $K_{pq}$ in Equation 3.44. Equation 3.43 is then applied to only the hyperparameters that link the last LSTM with the output as shown in Figure 3.10(b) using a weighted loss,

$$\eta = \alpha MSE + (1-\alpha)KMSE \tag{3.46}$$

where typical values of the weighting parameter $\alpha$ lie within the range $0.9 < \alpha < 0.9999$.

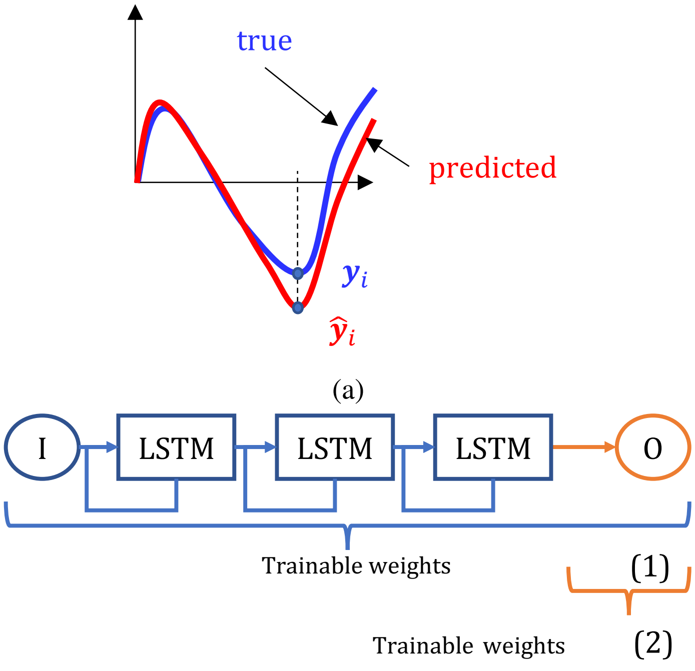

(a)

(b)

Figure 3.10: Transfer learning concept. (a) Schematics for the MSE calculation, (b) Trainable parameters (1) using only MSE, (2) using the combined loss.

The error on predicting new strain histories (not used during training), as it will be used in a FE solver, is less than 2% for the stress tensor and less than 9% for the localized data as shown in [28].

### 3.5.3 SCL implementation into a FE solver

The SCL is implemented considering that there is an essential difference between how the ML model is trained to produce the SCL and how it predicts while performing the FE simulations. In the former, the model receives the entire strain history as input and provides the entire stress history as output. In the latter, this is not the case. At any given point in the simulation, only the strain history up to that point is known. In other words, at the point where the SCL is ready to advance to the next loading step, it only has available the information of the previous steps. That is, the current solution should be calculated considering (1) the current strains and (2) the history of the loading path. For this reason, the SCL is *stateful*, which means it stores the current state $\mathcal{S}_t$, and then uses this information for the new prediction, in a way very similar to the role of state variables in traditional constitutive laws. This becomes particularly challenging when using iterative solvers since after each trial, the SCL automatically updates its state. The following paragraph explains how this obstacle is addressed.

Let us assume that the solution has converged to point $a$, and the solver attempts to obtain the new equilibrium position. As the conjugate gradient solver iterates, it might produce several intermediate solutions, *e.g.*, $b$ and $c$, until it reaches an equilibrium point $d$ in which the solution is converged as shown schematically in Figure 3.11. For each iteration $k$, *e.g.*, from previous solution point $a$ to $b$, a naïve implementation of the SCL model would update its state (given by the solution at $b$), $\mathcal{S}_t \leftarrow \mathcal{S}^{(k)}$, which would now be used to predict a new point $c$. This would be erroneous because $b$ does not correspond to the equilibrium point of the loading path. Thus, this behavior would find a solution corresponding to a different (fictitious) loading path which would consider the trial solution as part of the previous history.

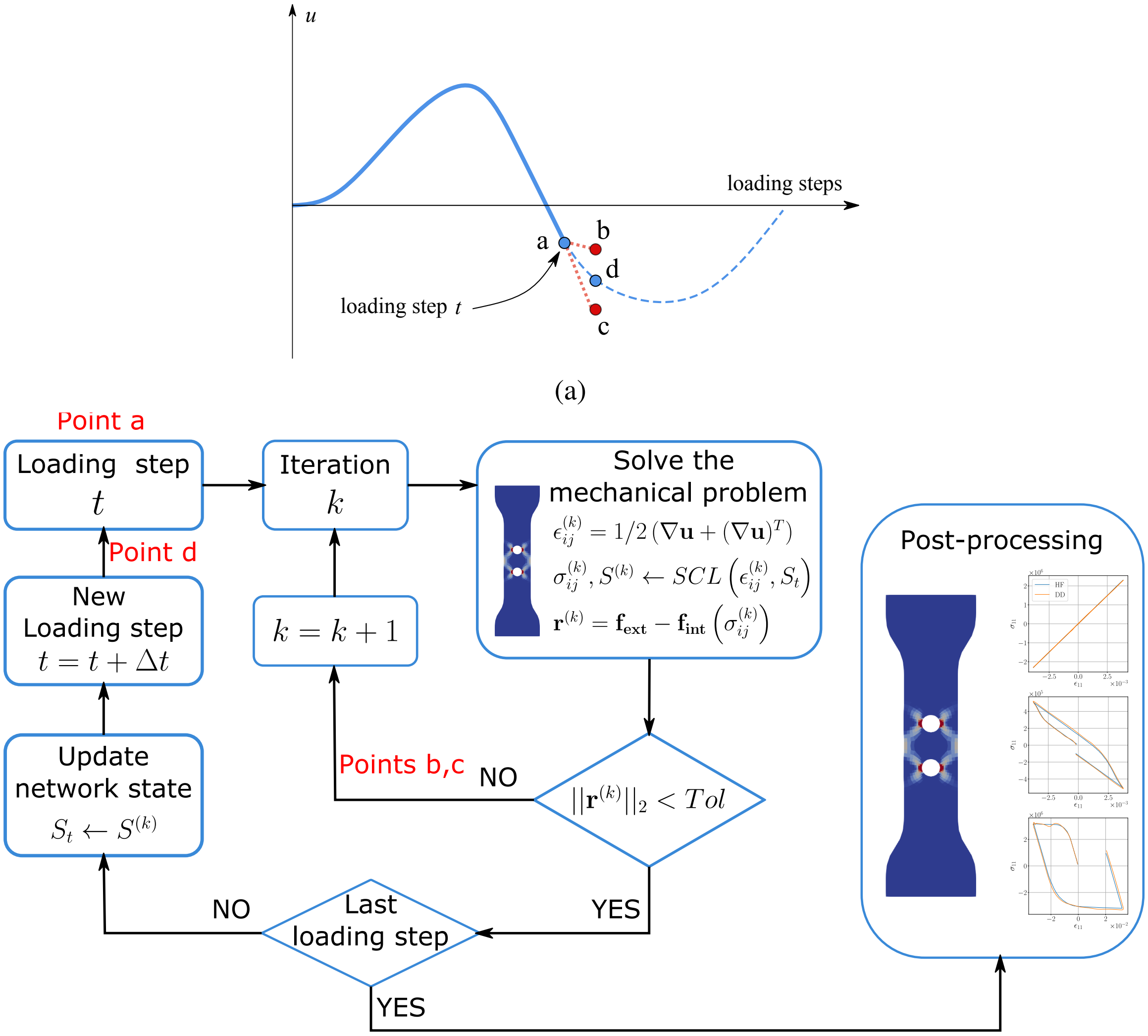

$u$
loading steps
a
b
d
c
loading step $t$
(a)
Point a
Loading step
$t$
Iteration
$k$
Solve the mechanical problem
$\epsilon_{ij}^{(k)} = 1/2\left(\nabla \mathbf{u} + (\nabla \mathbf{u})^T\right)$
$\sigma_{ij}^{(k)}, S^{(k)} \leftarrow SCL\left(\epsilon_{ij}^{(k)}, S_t\right)$
$\mathbf{r}^{(k)} = \mathbf{f}_{\text{ext}} - \mathbf{f}_{\text{int}}\left(\sigma_{ij}^{(k)}\right)$
Point d
New Loading step
$t = t + \Delta t$
$k = k + 1$
Post-processing
HF
DD
Update network state
$S_t \leftarrow S^{(k)}$
Points b,c
NO
$||\mathbf{r}^{(k)}||_2 < Tol$
NO
Last loading step
YES
YES

(b)

Figure 3.11: SCL implementation in a quasi-static boundary value problem. (a) diagram of possible solutions during the iterative process, (b) flowchart of the overall solution scheme with SCL implementation.

To overcome this problem, the state of the SCL to the previously converged point *a* is *reseted*, at the beginning of **each** iteration of the conjugate gradient, $\mathcal{S}_t \leftarrow$ reset, as depicted with the flowchart of Figure 3.11b. In this way, it is ensured that during the iterations, the SCL state corresponds to that of the previous converged solution *a* and it is not updated at the trial points *b* and *c*. Only after the equilibrium solution is found, *d*, the state $\mathcal{S}_t \leftarrow \mathcal{S}^{(k)}$ is updated. This is equivalent to *elastic-predictor plastic-corrector* in the radial return algorithm for plasticity [46] where the state of the material (described by the accumulated plastic strain) is not updated until the algorithm converges.

### 3.5.4 Summary of the homogenization technique with ML

In this work, we showed that the SCL not only can homogenize the behavior microstructure, but also can capture the aforementioned localized measures, *e.g.*, maximum damage and von Mises stress at the lower scale. A thorough analysis of the performance and validation of the method can be found in [28] where we show a comparison between the solution of an engineering-scale problem using the SCL as a material behavior and a concurrent multiscale analysis.

# CHAPTER 4

# RESULTS

The primary goal of the model is to predict the anomalous erosion ridges and how are they affected by different heat fluxes (power to the wall from the ions). Several parameters are included in this chapter in order to demonstrate how the erosion ridges develop throughout the simulation.

Firstly, section 4.1 provides a validation of the method using boron nitride since it is widely used in HET devices, and therefore, there are several publications with estimated erosion rates, temperatures, and power deposited to the walls. In this case, three model behaviors are analyzed, (i) using a pure sputtering model and no material contribution, (ii) sputtering model and elastic material behavior, and (iii) sputtering model and inelastic material behavior (which accounts for microcracks). For these three models, we first show how the erosion profiles evolve with time, second, we show how the erosion rates and surface parameters (such as roughness and peak to peak values) evolve with time, and finally, we present a statistical study on how these quantities vary with the input power.

Secondly, in section 4.2, the plasma-wall interaction model is applied to fused silica. In this case, we use a sputtering model and data-driven material behavior obtained using the approach defined in section 3.5 since the elastic and inelastic material models have limitations (section 3.4). The results are presented for several power depositions.

## 4.1 Application to boron nitride

This section shows a preliminary case study, the results, and the conclusions that can be obtained from it.

### 4.1.1 Setup

Consider a rectangular specimen of width 50 mm and a height of 7 mm. Figure 4.1[1] shows schematically the specimen as well as the boundary conditions for both the thermal and mechanical models used in this work. On the one hand, the thermal boundary conditions correspond to the heat flux exerted by the ions defined in section 2.2, and the radiation to the environment by defining a reference temperature, $T_{ref}$. On the other hand, the mechanical boundary conditions correspond to displacement constraints in the horizontal axis for the sides of the specimen and the vertical axis for the bottom of the specimen. The parameters used in this work for the erosion process simulations are tabulated in Table 4.1.

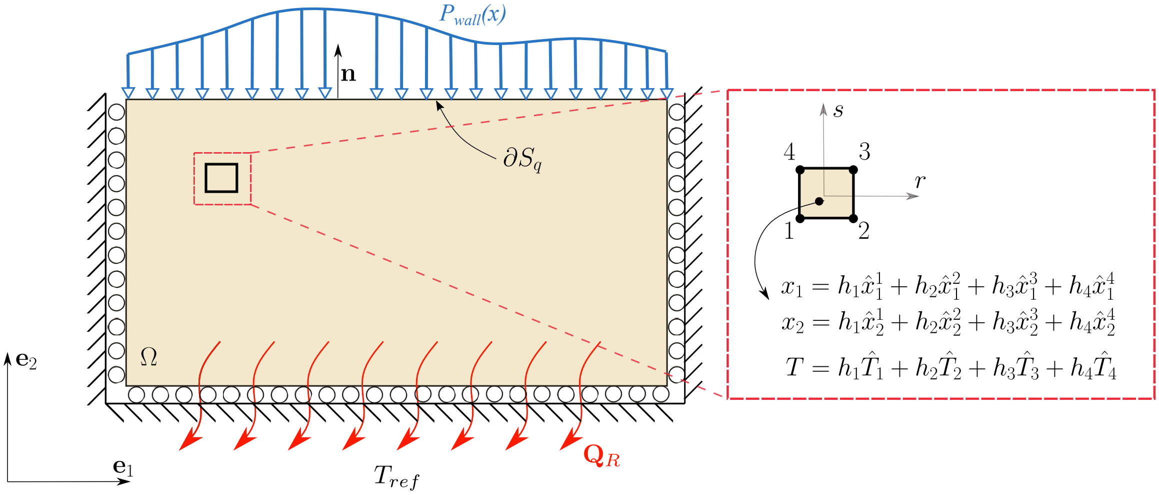
$P_{wall}(x)$
$\mathbf{n}$
$\partial S_q$
$\Omega$
$\mathbf{e}_2$
$\mathbf{e}_1$
$T_{ref}$
$\mathbf{Q}_R$
$s$
$r$
4
3
1
2
$x_1 = h_1\hat{x}_1^1 + h_2\hat{x}_1^2 + h_3\hat{x}_1^3 + h_4\hat{x}_1^4$
$x_2 = h_1\hat{x}_2^1 + h_2\hat{x}_2^2 + h_3\hat{x}_2^3 + h_4\hat{x}_2^4$
$T = h_1\hat{T}_1 + h_2\hat{T}_2 + h_3\hat{T}_3 + h_4\hat{T}_4$

Figure 4.1: Schematics for the thermal and mechanical boundary conditions of the thermo-elastic model.

*Material failure criteria*

As mentioned in the previous section, the material state is defined as $w/w_{\max} = 1$, where $w_{\max}$ is the strain energy density when the material meets the failure criteria defined by

---

[1] This is Figure 2.14 reproduced here for clarification.

Table 4.1: General parameters for the erosion process simulation.

<table>
<tr><th>Parameter</th><th>Description</th><th colspan="3">value</th></tr>
<tr><td>$E$</td><td>Young's Modulus</td><td colspan="3">40000 MPa [23, 56]</td></tr>
<tr><td>$\nu$</td><td>Poisson's ratio</td><td colspan="3">0.2</td></tr>
<tr><td>$\rho$</td><td>Density</td><td colspan="3">$2{\times}10^{-9}$ Tn/mm$^3$ [56]</td></tr>
<tr><td>$K$</td><td>Thermal conductivity</td><td colspan="3">29 mW/mm K [19]</td></tr>
<tr><td>$\varepsilon$</td><td>Emissivity</td><td colspan="3">0.9 [19, 57]</td></tr>
<tr><td>$C_p$</td><td>Specific Heat</td><td colspan="3">$0.81{\times}10^9$ mJ/Tn K [56]</td></tr>
<tr><td>$T_{ref}$</td><td>Reference temp. for radiation</td><td colspan="3">298 K</td></tr>
<tr><td rowspan="5">$\alpha$</td><td rowspan="5">Thermal expansion coeff.</td><td>Temp K</td><td>value</td><td rowspan="5">[56]</td></tr>
<tr><td>298</td><td>$0.6{\times}10^{-6}$</td></tr>
<tr><td>673</td><td>$1.1{\times}10^{-6}$</td></tr>
<tr><td>1073</td><td>$1.5{\times}10^{-6}$</td></tr>
<tr><td>1473</td><td>$2.8{\times}10^{-6}$</td></tr>
</table>

Equation 2.28 and for the boundary conditions shown in Figure 4.1,

$$w_{\text{max}} = \frac{\lambda + 2\mu}{2\mu\,(3\lambda + 2\mu)}\sigma_C^2 \tag{4.1}$$

where $\lambda$ and $\mu$ are the Lame constants obtained from the elastic constants shown in Table 4.1. The derivation of Equation 4.1 can be found in Appendix A.

*Element size*

The main features of interest are the spatial period of the anomalous ridges that are of the order of $l = 1$ mm (spatial frequency $f = 1$ 1/mm) [16]. Consequently, according to the Nyquist sampling theorem, the sampling frequency should be $f_s \geq 2f = 2$ 1/mm or the sampling interval $x_s \leq 0.5$ mm. Thus, an element size of 0.5 mm or smaller would suffice to capture the ridges. On the other hand, for BN and BN-SiO$_2$ the microcracks formed in the microstructure are in the order of 1.5 or less $\mu$m [22], and the grain size of silica is around 20 $\mu$m [21]. Thus, an element size of $> 50$ $\mu$m (0.05 mm) is deemed enough to represent the RVE of the microstructure. Therefore, the element size should be within 0.05 and 0.5 mm. In order to capture not only the anomalous ridges but the features of the order of up to 10 1/mm found in [23], an element size of 62.5 $\mu$m (0.0625 mm) is chosen in this work.

The total mesh is composed of 89600 square coupled temperature-displacement plane strain elements from the Abaqus library, and the material model defined in section 3.3 is implemented with UMAT user material subroutine from Abaqus [42].

*Ion energy distribution*

Figure 4.2 shows the ion energy distribution for the simulation to represent typical values of mean energy of around 130 eV at the front $E_F$ (original flat surface) of a laboratory setup [23]. In order to simulate different operation conditions, the ion current density $j_{\text{ion}}$ varies from 0.05 to 0.25 mA/mm$^2$ (5 to 25 mA/cm$^2$). A representative value for a laboratory setup is approximately 0.1 mA/mm$^2$ (10 mA/cm$^2$) [23], and it is accounted. According to the minimum and maximum values of ion energy, $\approx 100$ to $\approx 225$ eV, respectively, as shown in Figure 4.2, the expected power to wall $P_{wall}$ will be within 5 to 57 mW/mm$^2$ (5000 to 57000 W/m$^2$). This range of heat flux lies within characteristic values for a thruster [19].

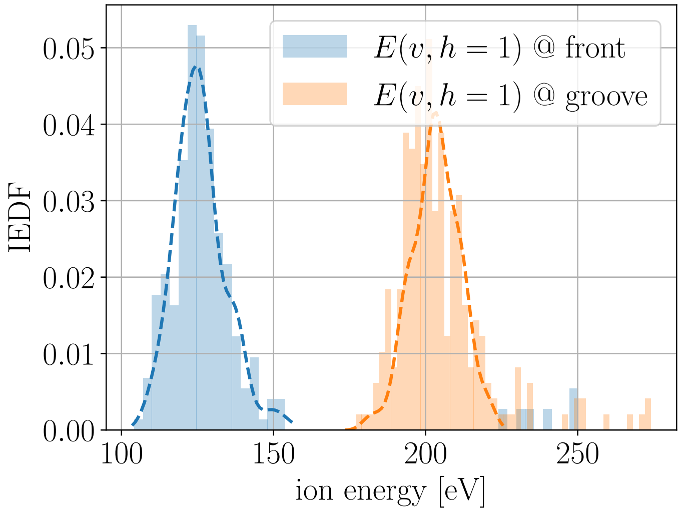

Figure 4.2: Ion energy distribution $E_F$ and $E_G$ for reference bounds to use in the erosion process simulation.

*Time increment and number of simulations*

The time increment bounds are determined considering the maximum and minimum probabilities that could be attained, according to Equation 2.26. The minimum probability is given when (in average) only one element is removed from the surface $k = 1$, thus, Equation 2.26 becomes, $J_0(P) = \frac{1}{N}$ and combining with Equation 2.27, it leads to

$$\Delta t_{\text{min}}(P) = \frac{y_e}{\dot{y}_{\text{sy}}(P)N} \tag{4.2}$$

and the maximum probability is obtained when all elements are removed from the surface $k = N$, which leads to

$$\Delta t_{\text{max}}(P) = \frac{y_e}{\dot{y}_{\text{sy}}(P)} \tag{4.3}$$

As it can be seen, the time increment bounds also depend on the heat flux range, as shown in Figure 4.3.

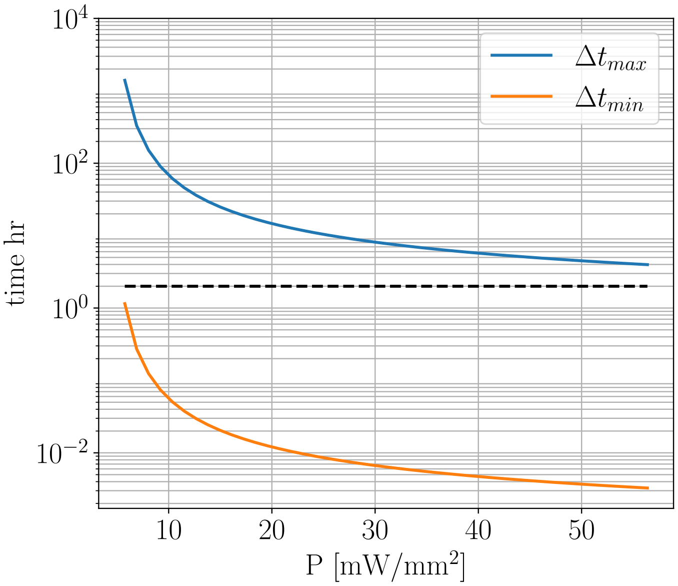

Figure 4.3: Time increment bounds for the probabilistic approach.

In this case study, the time increment is selected as $\Delta t = 2$ h as it can be seen from the figure with dashed lines. This selection is chosen such that it can be maintained constant throughout the simulation. Nevertheless, the implementation of the solver allows choosing a different time increment that is automatically adjusted upon reaching the thresholds.

For each operation condition, 10 simulations are performed in order to obtain statistical values of certain parameters.

Finally, Figure 4.4 shows the resulting joint probability distribution $J(P, D)$ to be used in the analysis from the aforementioned simulation conditions.

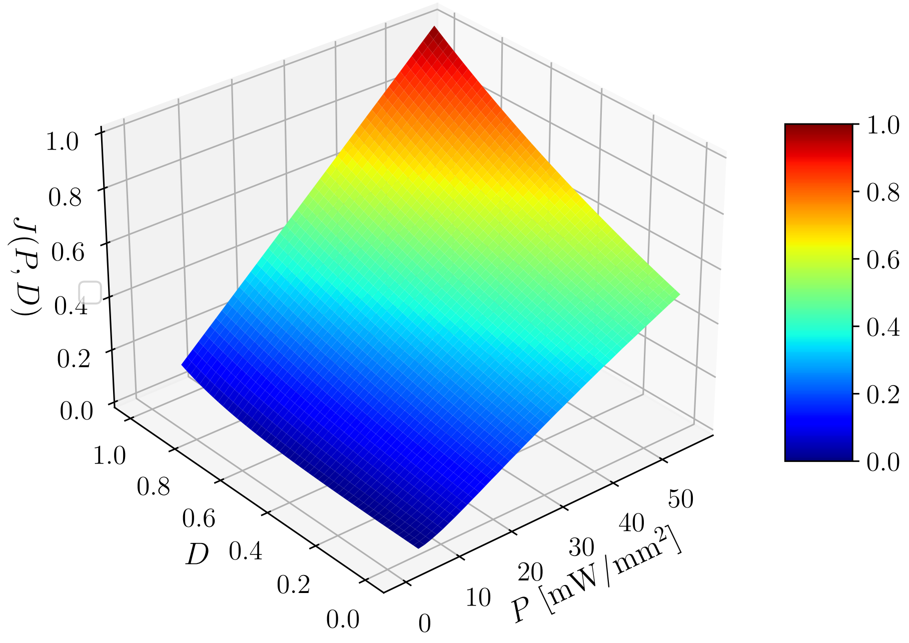

Figure 4.4: Joint probability distribution for the case study.

### 4.1.2 Results of the erosion process simulations

For the problem described in subsection 4.1.1 three models are used and compared. The first model corresponds to a simulation in which only sputtering yield is accounted for the erosion process (*sputtering model*), the second model corresponds to a model that considers a combination of sputtering and elastic behavior (*elastic model*), and the third one, corresponds to the model that considers a combination of sputtering and the DE material model behavior (microstructure cracks and damage, *inelastic model*). For each model, seven different power levels were applied in the range described in subsubsection 4.1.1 and for each level, ten simulations were performed. In total, 70 simulations are analyzed per model. Figure 4.5 qualitatively shows the evolution of the surface for the three models considered in this work at three different power levels. In each subfigure, the sputtering model is in the top, the elastic model in the middle and the inelastic one in the bottom. Several observations can be made from the figures. First, in each case, the (mean) erosion rate is similar (as discussed in the next subsection) in all three models since the recession of the wall is similar at times shown in the figure. Secondly, as the power to wall increases in (b) and (c); the formation of features becomes more evident in the elastic and inelastic models whereas they do not form in the sputtering model.

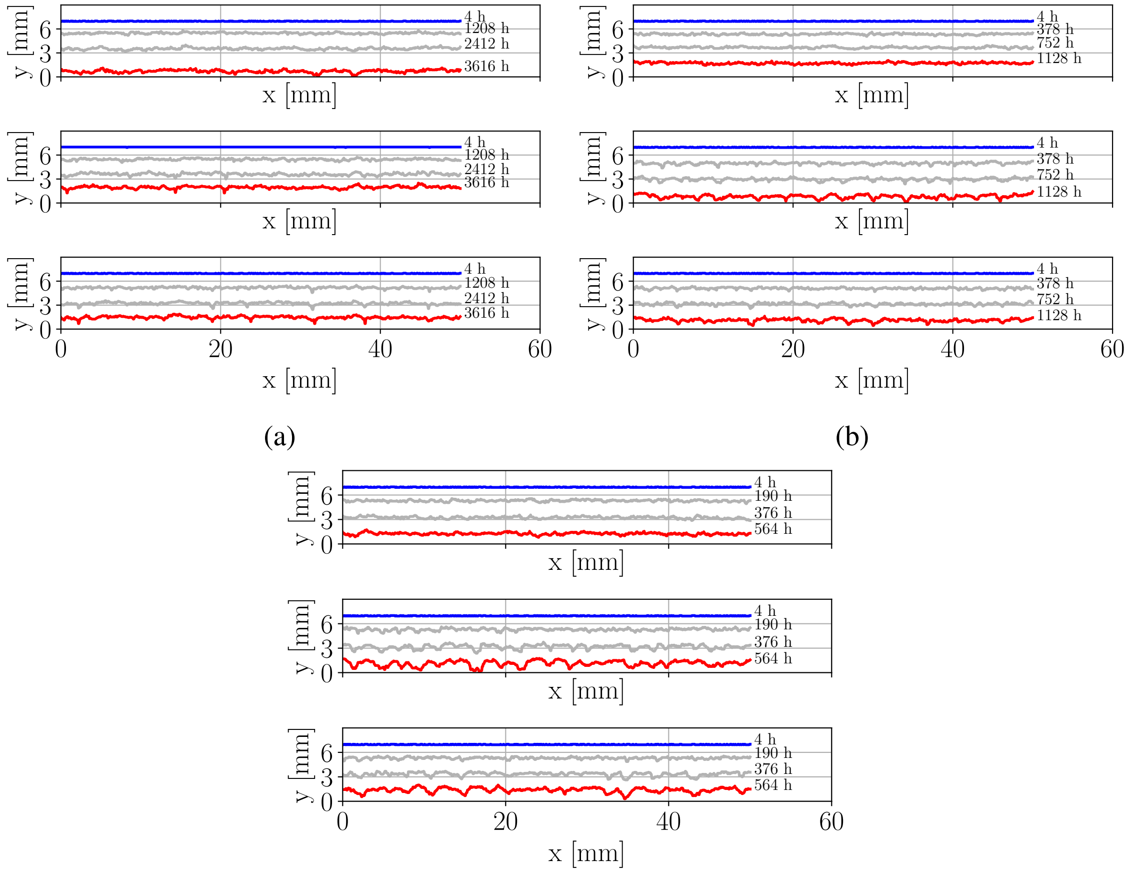

(a)

(b)

(c)

Figure 4.5: Surface evolution for the sputtering (top), the elastic (center) and the inelastic (bottom) models at (a) approx. 20 mW/mm$^2$, (b) 35 mW/mm$^2$ and (c) 50 mW/mm$^2$

Figure 4.6 shows the variables that can be used to quantify the evolution of the surface features for one randomly selected realization at the same three different power levels. As it can be seen, in the first case, (a) ion current at 0.1 mA/mm$^2$, the wavelength remains approximately constant throughout the simulation regardless of the model; the same applies to the roughness and peak-to-valley. However, as the power level increases (subfigures b and c), there is a remarkable difference in how the elastic and inelastic models can reproduce the features in contrast to the sputtering model. Firstly, it can be seen how the wavelength decreases in the material-based models. This suggests that the models in which the material is considered, the features can be captured whereas the state-of-the-art sputtering model cannot. In addition, the roughness and peak-to-peak increase through time as well. This is in agreement with previous research in which it has been shown that sputtering-based models cannot capture the anomalous ridges.

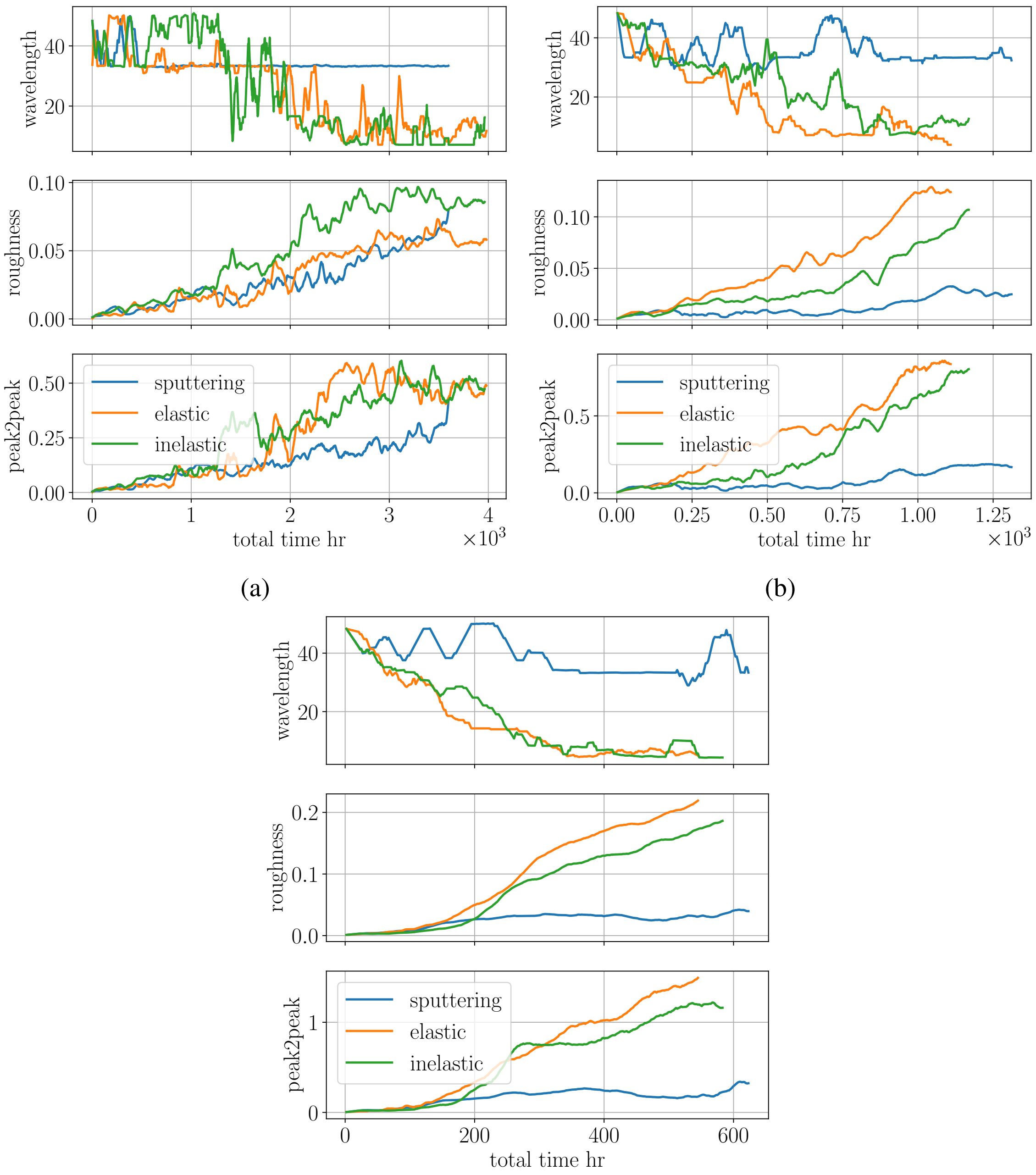

(a)

(b)

(c)

Figure 4.6: Wavelength, roughness and peak-to-peak at (a) approx. 20 mW/mm$^2$, (b) 35 mW/mm$^2$ and (c) 50 mW/mm$^2$

In the following section, a comprehensive statistical analysis is provided in order to further characterize and compare the different models.

*Statistics of erosion process for a range of powers for boron nitride*

This section shows the statistical analysis of the results. In each case, the values of the parameters are taken at the end of the simulation, *i.e.*, when the erosion recession cannot go further than the height of the specimen (see subsection 4.1.1) unless otherwise noticed. In each plot, the dots represent the mean values and the bars the standard deviations in each axis for each of the operation conditions.

Figure 4.7 shows the relationship between the erosion rate and the power applied to the wall for the *sputtering* (blue circles), the *elastic* (orange triangles), and the *inelastic* (green squares) models. Although not enough data is reported about the erosion rates in experiments, the typical range of erosion rate is 2.5 to 9 $\mu$m/h [15, 58, 59] depending on the operation conditions and device. For the power to the wall, the range goes from 1000 W/m$^2$ up to 60,000 W/m$^2$ (1 - 60 mW/mm$^2$) [60, 19] considering the operation condition for which typical erosion rates are reported. The uncertainty of data is shown with the shaded areas in the figure. As it can be seen, the calculated values of erosion rates from the simulations lie within the measured values. Figure 4.8 shows the stress and temperatures as a function of the power to the wall. These relations are of great interest for engineers since it can help to determine which material is suitable for given operation conditions considering that the power to the wall is associated to the discharge power of the thruster [19]. As it can be seen from the figure, the stresses from the inelastic model (green squares) are lower than the ones from the elastic and sputtering models. This could indicate a stress release mechanisms upon material damage.

The materials used in HET, such as boron nitride, have very high melting points [61, 62], and the temperatures in a HET can range from 600 to 1000 K depending on operation conditions, geometry, and location [19, 59, 63]. Figure 4.8(b) shows that for the particular case of the specimen analyzed in this work, the temperatures are within a reasonable range. However, the comparison with a model of a HET channel is not straightforward because of the differences in boundary conditions and geometry, *i.e.* in a HET channel, the temperatures are distributed along the entire thruster, and the heat flux is applied only to a portion of it [19], whereas in our case, the specimen is entirely exposed to the heat flux with a geometry that does not favor heat dissipation. Nevertheless, the verification of the heat transfer solver is done considering the geometry and operation conditions as in [19].

In order to quantify the surface features, Figure 4.9(a) and (b) shows the roughness of obtained from each model and the peak-to-valley values also as a function of the power to the wall, respectively. As discussed in the previous section, even though the erosion rate is fairly similar in the three cases, the difference in the roughness and peak-to-valley suggests that the *elastic* and *inelastic* models can capture the creation of anomalous ridges, whereas the *sputtering* model cannot. This is the first time, to our best knowledge, that a wall erosion model can reproduce the erosion ridges in this length-scale (recall that several models can reproduce some ridges in the nanoscale in etching process by ion bombardment, [9, 25, 26, 27]).

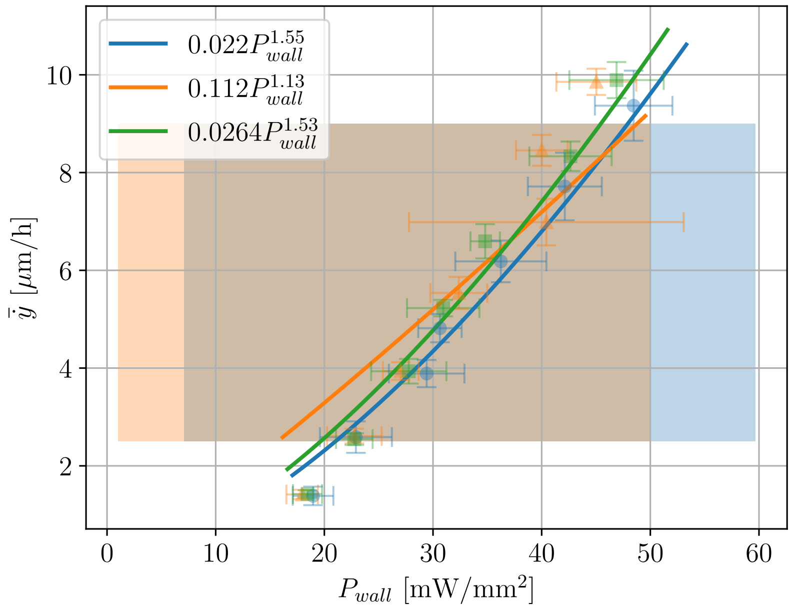

Figure 4.7: Estimated erosion rate for boron nitride as a function of the heat flow to the wall at each power level.

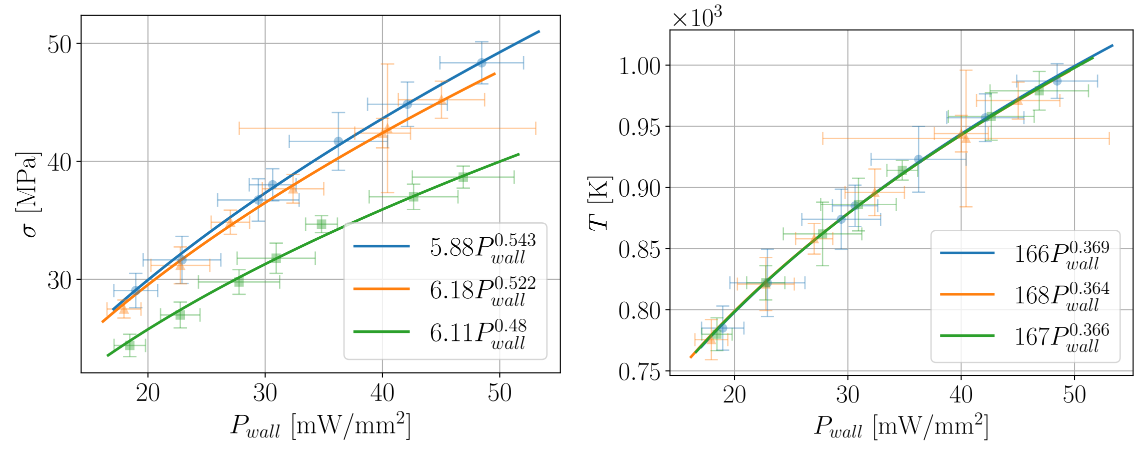

(a) (b)

Figure 4.8: Estimated (a) stresses and (b) temperatures as a function of the heat flow to the wall at each power level.

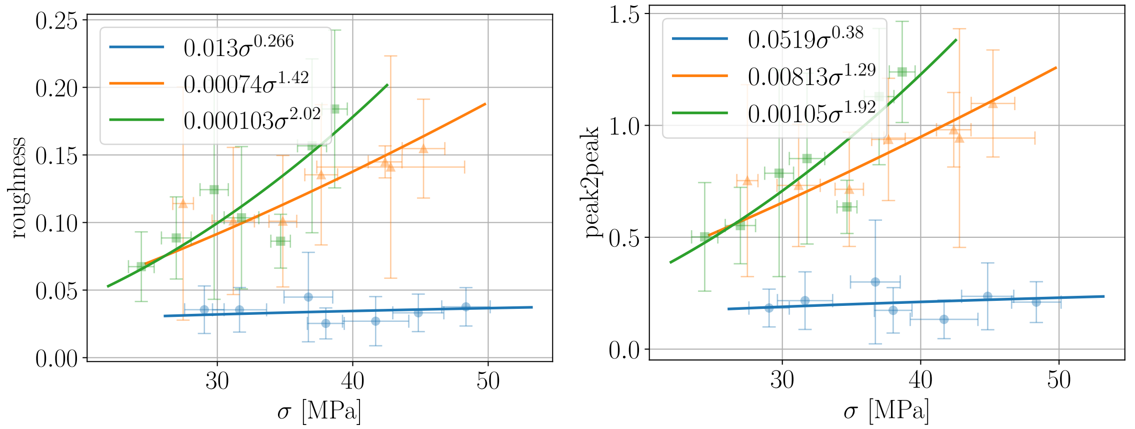

(a) (b)

Figure 4.9: (a) Roughness and (b) peak to valley values, as a function of the resulting mean stress of the specimen $\sigma$ for the sputtering (blue circles), the elastic (orange triangles), and inelastic (green squares) models.

As it can be seen, at the same power level, the stress obtained in the *inelastic* model is lower than the *sputtering* and *elastic* ones. This is because the inelastic model accounts for crack growth, and therefore, stress is relieved, leading to lower stress levels.

It is also of interest to find a relationship between the features' wavelength and the stress of the specimen. The hypothesis is that the anomalous erosion ridges are a result of an instability driven by the release of mechanical strain energy in the material [63].

In his work, the author found that the wavelength of the ridges was in the order of the mechanical stress $l \approx \mathcal{O}(\sigma^{-2})$. However, experimental results did not back up such a relationship, presumably because the experiments were conducted for a very short period of time and in a very small domain (a few hundreds of microns). Figure 4.10 shows the result of the erosion ridges at the end of erosion recession. The power-law indicates that the wavelength can be related to the stress with approximately a power of -2 in the *elastic* and *inelastic* models. Again, the *sputtering* model is unable to capture the erosion ridges as the wavelength appears insensitive to the stress to the wall. Furthermore, the *inelastic* models predict higher spatial frequencies (or lower wavelengths) at the same stress level indicating that the addition of inelastic behavior due to crack release energy could potentially help explain the formation of such ridges.

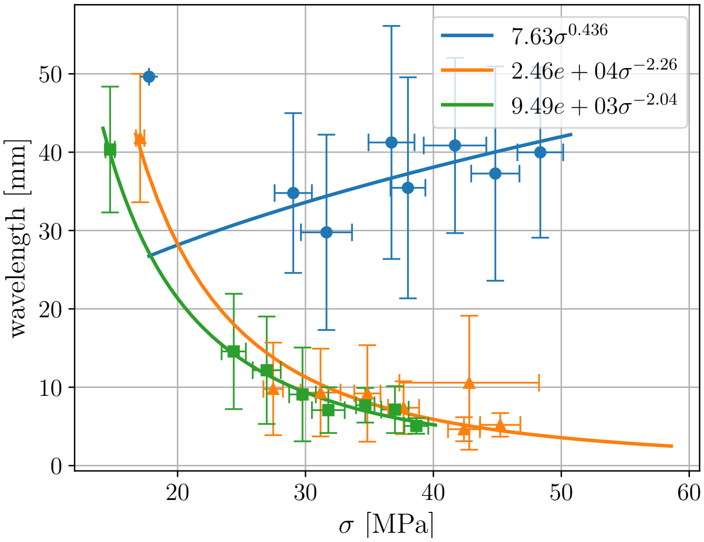

Figure 4.10: Surface features as a function of the mean stress of the specimen, $\sigma$.

## 4.2 Application to fused silica

In this section, we use the SCL in the plasma-wall interaction model to simulate the erosion process of a material that exhibits softening behavior and brittle fracture, such as fused silica.

### 4.2.1 Setup

The SCL model described in subsubsection 4.2.1 is implemented into the Plasma-Wall interaction model defined in chapter 2 to obtain the erosion of the material exposed to ion bombardment.

Consider a rectangular section of 100 mm width and 15 mm of height with the thermo-mechanical boundary conditions depicted in Figure 4.1 and described in subsection 4.1.1. For this section, we use fused silica in order to define a benchmark to be used for comparison with test data obtained from ion bombardment experiments on this material. The thermo-elastic parameters for fused silica and the constants for the sputtering model given by Equation 2.20 are tabulated in Table 4.3 and Table 4.2, respectively. In this section, we use the same material failure criteria as the one derived in subsubsection 4.1.1 and the element size is chosen to be equal to the size of the RVE of the fused silica microstructure, $l_e = 170\mu$m. The ion energy distribution for the simulation is shown in Figure 4.2 and the time increment is $\Delta t = 2$ hours as defined in Figure 4.3.

Table 4.2: Sputtering yield constants used for fused silica in this chapter, [21, 12].

| Parameter | Value |
|---|---:|
| $E_{th}$, eV | 18.3 |
| $B_0$ | 9.14E-01 |
| $B_1$ | 5.34E-02 |
| $B_2$ | -6.98E-04 |
| $B_3$ | 3.33E-06 |
| $k$ | 3.5E-03 |

*Representative Volume Element of the fused silica microstructure*

Fused silica ceramic has been previously used to understand the erosion mechanism in electric propulsion devices under mechanical stresses [23]. The material properties are

Table 4.3: Fused silica properties [65, 66].

| Parameter | Description | value |
|---|---|---|
| $E$ | Young's Modulus | 74000 MPa |
| $\nu$ | Poisson's ratio | 0.16 |
| $\rho$ | Density | $2.2\times10^{-9}$ Tn/mm$^3$ |
| $K_{Ic}$ | Fracture Toughness | 0.66 MPa m$^{1/2}$ |
| $\sigma_c$ | Fracture strength | 170 MPa |
| $G_c$ | Fracture energy | 0.006 mJ/mm$^2$ |
| $\delta_{max}$ | Maximum crack opening | $6.8\times10^{-5}$ mm |
| $E_{nn}$ | Traction-displ. tangent | $1.35\times10^{8}$ MPa/mm |
| $K$ | Thermal conductivity | 1.4 mW/mm K |
| $C_p$ | Specific Heat | $670\times10^{6}$ mJ/Tn K |
| $T_{ref}$ | Reference temp. for radiation | 298 K |
| $\alpha$ | Thermal expansion coeff. | $5\times10^{-7}$ |

summarized in Table 4.3. In this chapter, the crack length is assumed to be $d = 15\mu$m according to typical values of finishes and subsurface damage correlation [64, 23]. The crack density is obtained as [34],

$$f \approx \left[\frac{1}{3d}\right]^3 \tag{4.4}$$

and the 2-dimensional density as,

$$N_a = f^{2/3} \tag{4.5}$$

The size of the RVE of the microstructure is 170 $\mu$m and the crack density leads to a total of 14 cracks that are randomly placed at $0°, \pm45°, 90°$ to provide a more realistic crack distribution as depicted in Figure 4.11. As it is defined in subsubsection 3.4, the cracks can grow following the cohesive path shown in the figure. The fracture strength $\sigma_c$, maximum crack opening $\delta_{max}$, fracture energy $G_c$ and critical opening $\delta_c$ are defined following the guidelines of subsubsection 3.4 and are tabulated in Table 4.3.

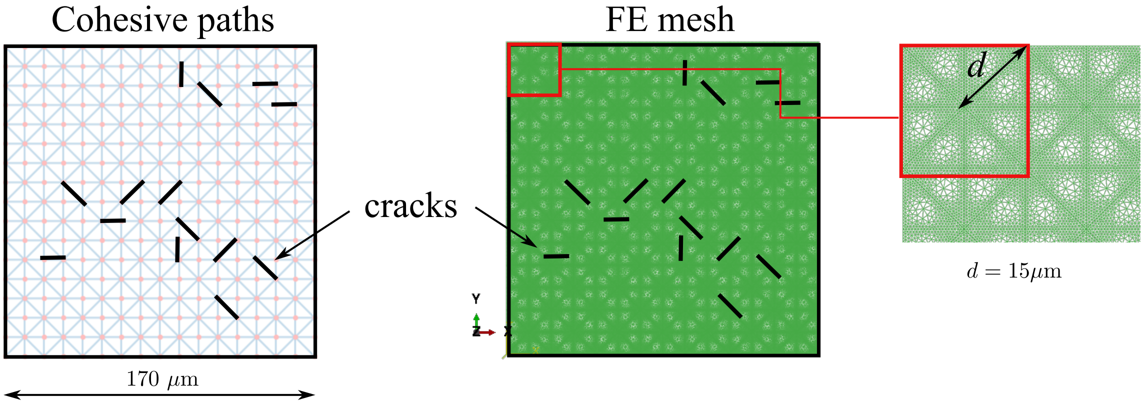

Figure 4.11: RVE of the fused silica microstructure with the cohesive element path for crack growth, the cracks location and the FE mesh.

*SCL and training*

For the microstructure shown in Figure 4.11, we use $s_{\epsilon M} = 0.01$ and $s_{\theta M} = \pi/6$ to obtain the kernel function provided in Equation 3.33. Also, a loading sequence length $T = 200$ is adopted. The overall (joint) distribution of principal strains is depicted in Figure 4.12. Using the same approach defined in subsubsection 3.5.1, we expose the RVE shown in Figure 4.11 to 10,000 input strain cases to obtain the average stresses (Equation 3.37) that will be used as the output of the SCL.

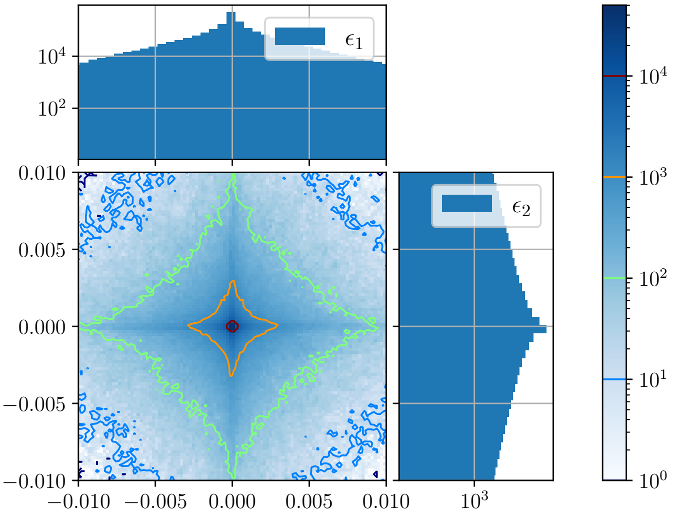

Figure 4.12: Distribution of principal strains for the fused silica RVE.

Figure 4.13 shows the evaluation with test (unseen) cases for three different architectures (1,2, and 3 LSTMs layers) with 100 units each. As it can be seen from the figure, the error in the stresses is less than 0.25% in all cases. Following the results, we select the architecture with three layers and 100 units per layer RNN considering that it provides the best performance ($< 0.2\%$ error) among the tested architectures with a parameter $\alpha = 0.99$ for the combined loss.

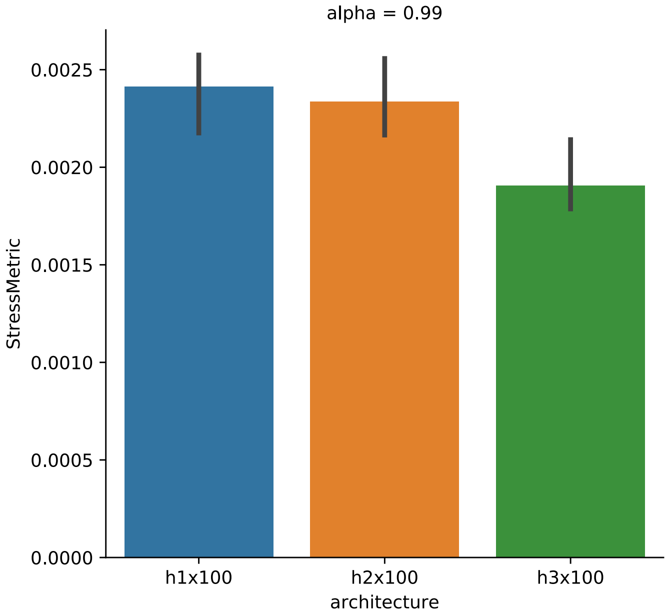

Figure 4.13: Evaluation of several architectures with unseen cases.

From Figure 4.14 through Figure 4.17 we show a comparison of the predicted softening behavior using the SCL (orange) with the real behavior obtained from the FE analysis of the RVE (blue) for four randomly selected strain histories. In each case, we show to the left the initial cracks in black and the crack propagation in red, and to the right, the equivalent stress vs. equivalent strain where the black dots indicate the current stress value. As it can be seen from the results, the SCL is able to capture the softening behavior of the microstructure for completely different loading scenarios without imposing any kind of assumptions of constraints. The sub-figures depict the load increments at 25% (a, b), 50% (c, d), 75% (e, f), and 100% (g, h).

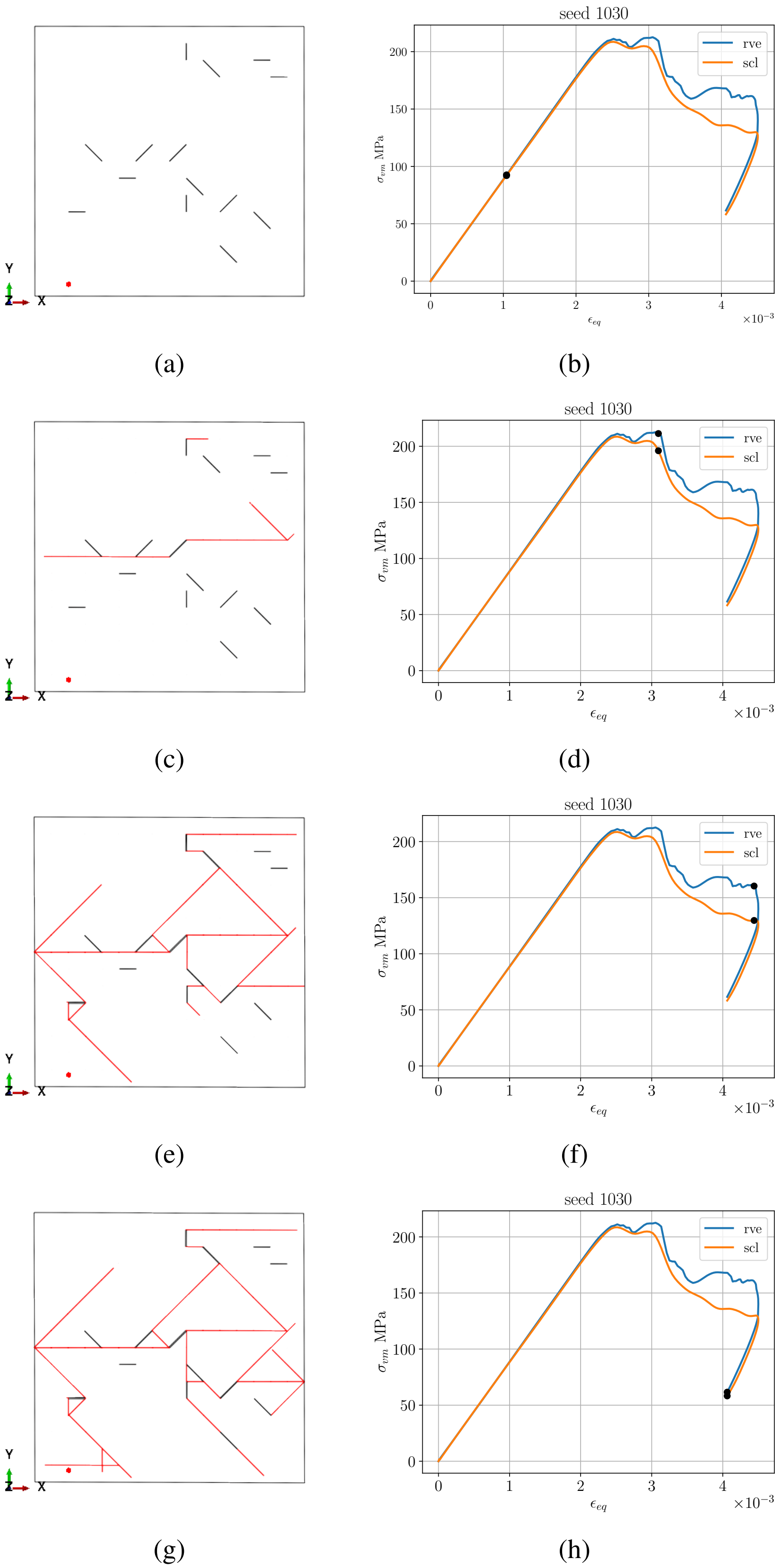

(a) (b)

(c) (d)

(e) (f)

(g) (h)

Figure 4.14: Comparison between real (blue) and predicted (orange) behavior of the microstructure for test (unseen) cases for strain history labeled 1030.

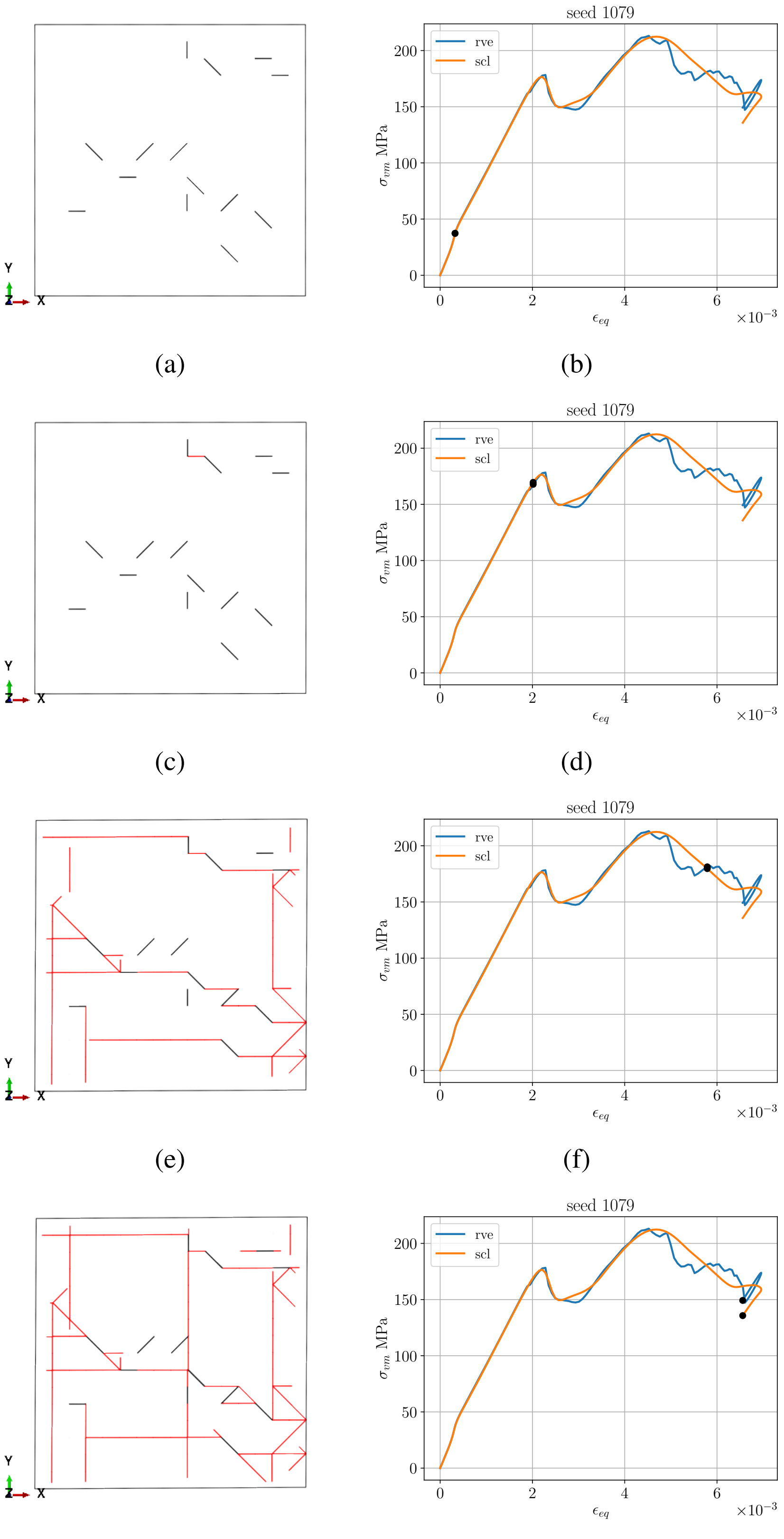

(a) (b)

(c) (d)

(e) (f)

(g) (h)

Figure 4.15: Comparison between real (blue) and predicted (orange) behavior of the microstructure for test (unseen) cases for strain history labeled 1079.

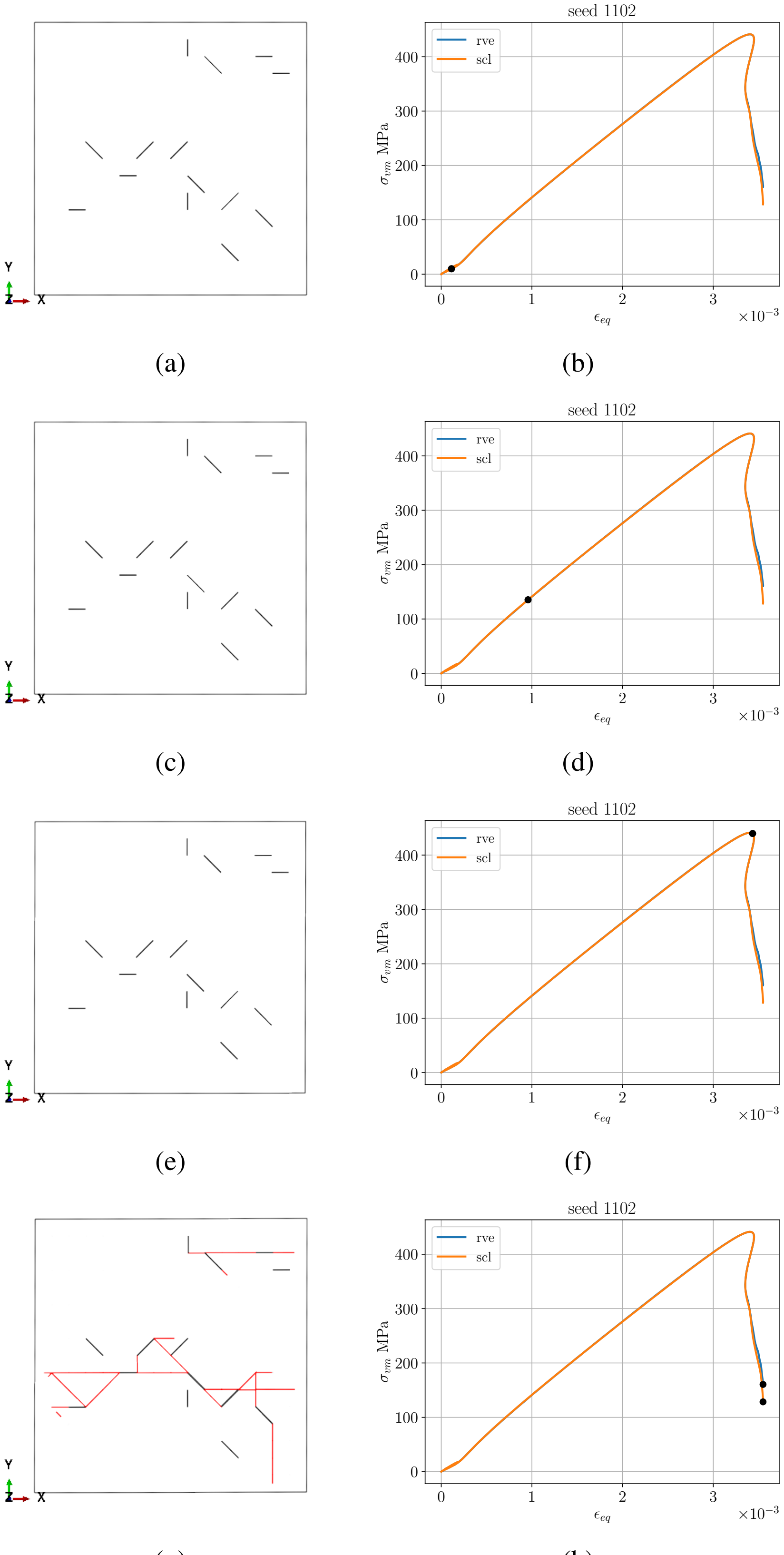

(a) (b)

(c) (d)

(e) (f)

(g) (h)

Figure 4.16: Comparison between real (blue) and predicted (orange) behavior of the microstructure for test (unseen) cases for strain history labeled 1102.

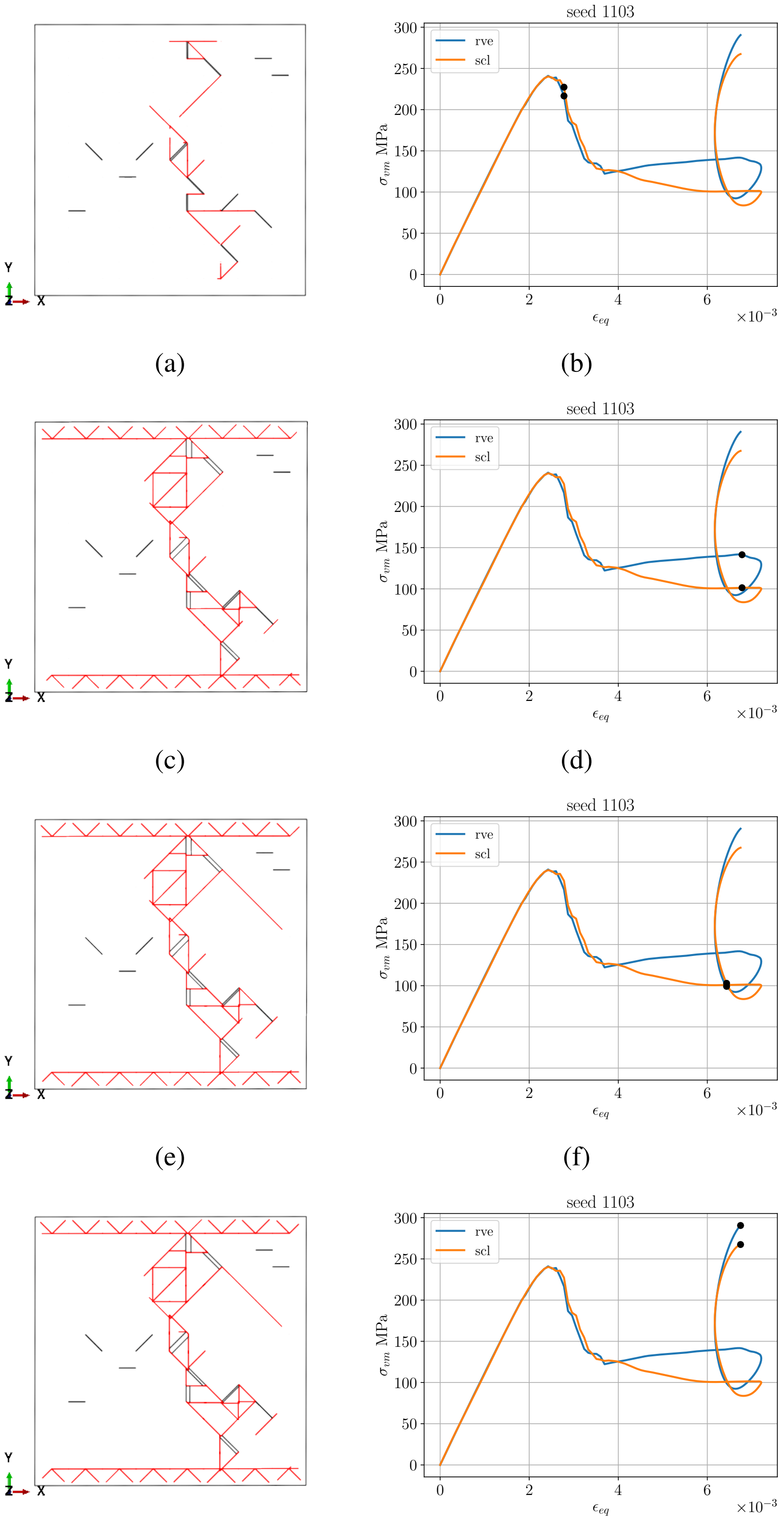

(a) (b)

(c) (d)

(e) (f)

(g) (h)

Figure 4.17: Comparison between real (blue) and predicted (orange) behavior of the microstructure for test (unseen) cases for strain history labeled 1103

### 4.2.2 Results of the erosion process simulations

In this section we show the results of the plasma-wall interaction model for fused silica using the sputtering and material model with SCL described in section 4.2. The first part shows the temperatures and stress fields at several snapshots for different power inputs. Secondly, a range of heat fluxes is analyzed to provide a statistical measure of several parameters of interest such as typical erosion rates, roughness, peak-to-valley values, and the relationships to the applied heat. These statistics are also compared against other model behavior such as (i) pure sputtering, and (ii) sputtering with elastic material behavior. The goal is to show the capabilities of predicting the anomalous erosion ridges by combining the sputtering yield and a homogenized material behavior at different input power levels.

Figure 4.18 through Figure 4.20[2] depict the solution at three different power levels ranging from approximately 36 mW/mm$^2$ to 90 mW/mm$^2$ (36 kW/m$^2$ - 90 kW/m$^2$), respectively. It can be seen in all three cases, that the erosion process begins homogeneous throughout the length of the specimen. However, the erosion ridges start forming at earlier times for higher powers. It is worth noticing that the stress distribution forms a periodic distribution of lobes around the points where erosion valleys begin to develop, for example at around 1300 hr. in Figure 4.18(b), at 370 hr. in Figure 4.19 and 168 hr. in Figure 4.20. These lobes have a wavelength between 2 and 6 mm, which are in the order of the Debye length of the plasma. The stress distribution indicates concentration points that ultimately lead to a developing of more prominent valleys observed as time evolves.

#### *Statistics of erosion process for a range of powers for fused silica*

A set of heat fluxes are applied to the specimen in order to find relations with several parameters of interest. Ten simulations are performed for each power level ranging from 20 to around 80 mW/mm$^2$ (20-80 kW/m$^2$). The case with power levels of around 90 kW/m$^2$

---

[2] It should be noted that in this case, the simulation is terminated earlier due to some points exceeding the temperature of softening point for fused silica, 1900 K [65].

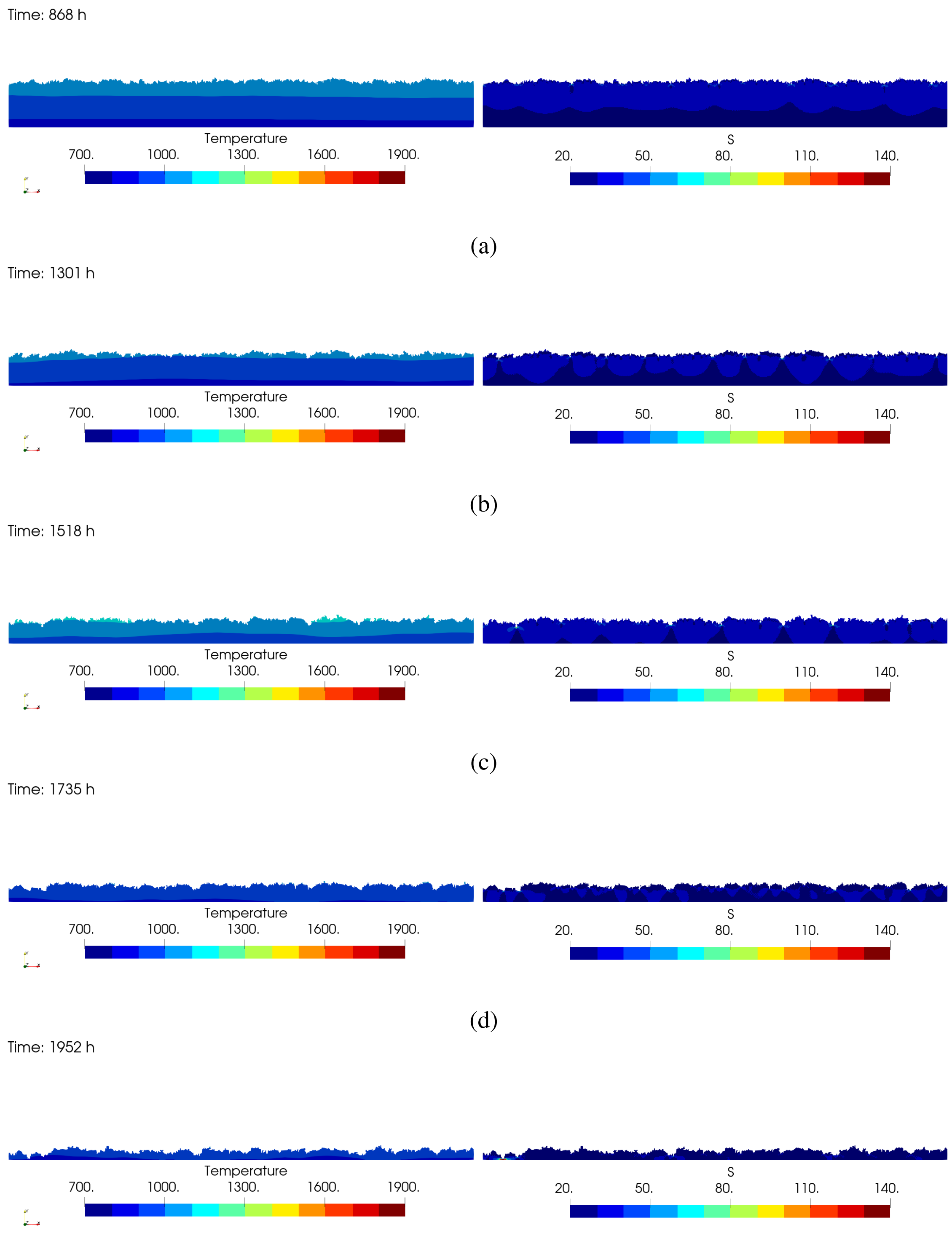

(a)

(b)

(c)

(d)

(e)

Figure 4.18: Temperature (K) and stress (S, MPa) fields for the erosion process at approximately 36 mW/mm$^2$.

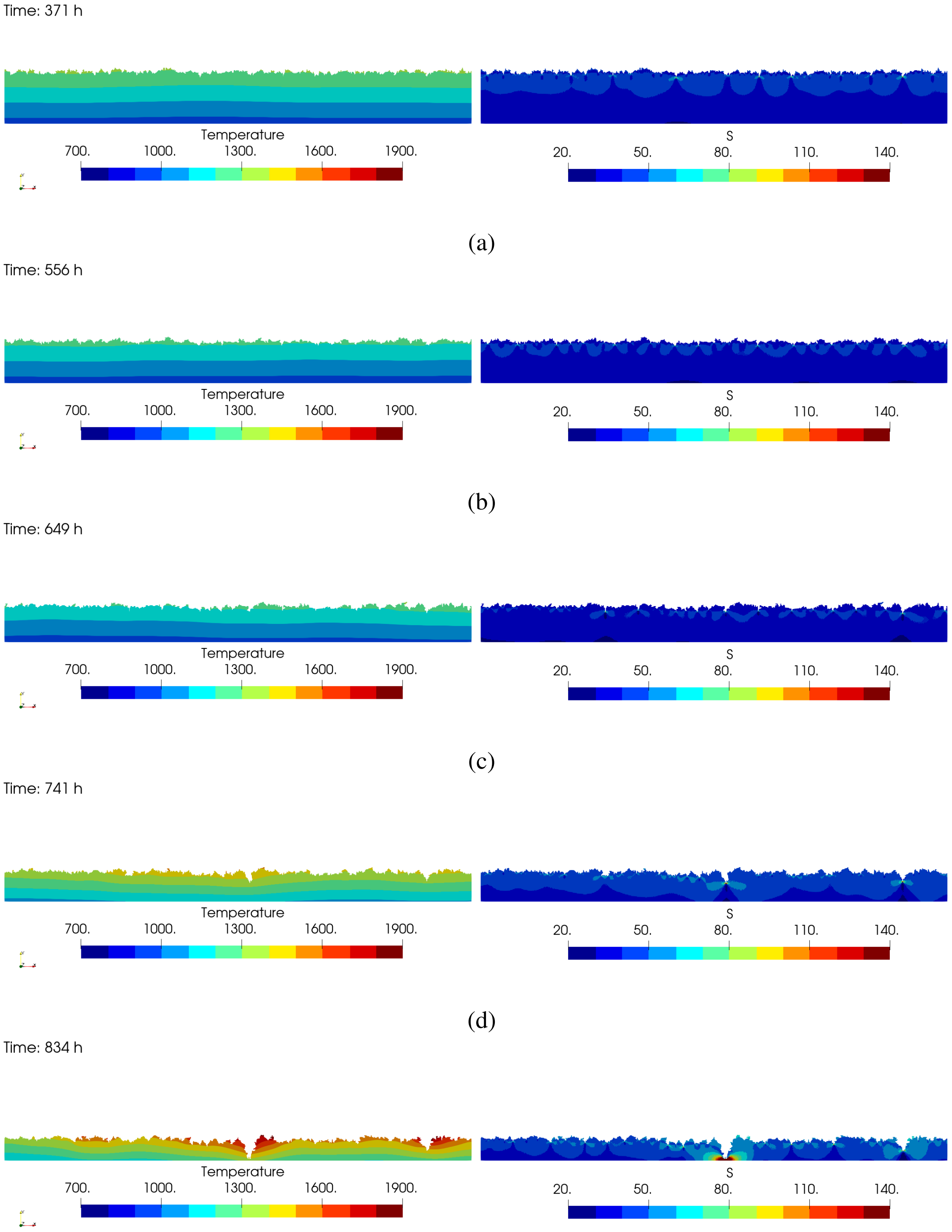

(a)

(b)

(c)

(d)

(e)

Figure 4.19: Temperature (K) and stress (S, MPa) fields for the erosion process at approximately 50 mW/mm$^2$.

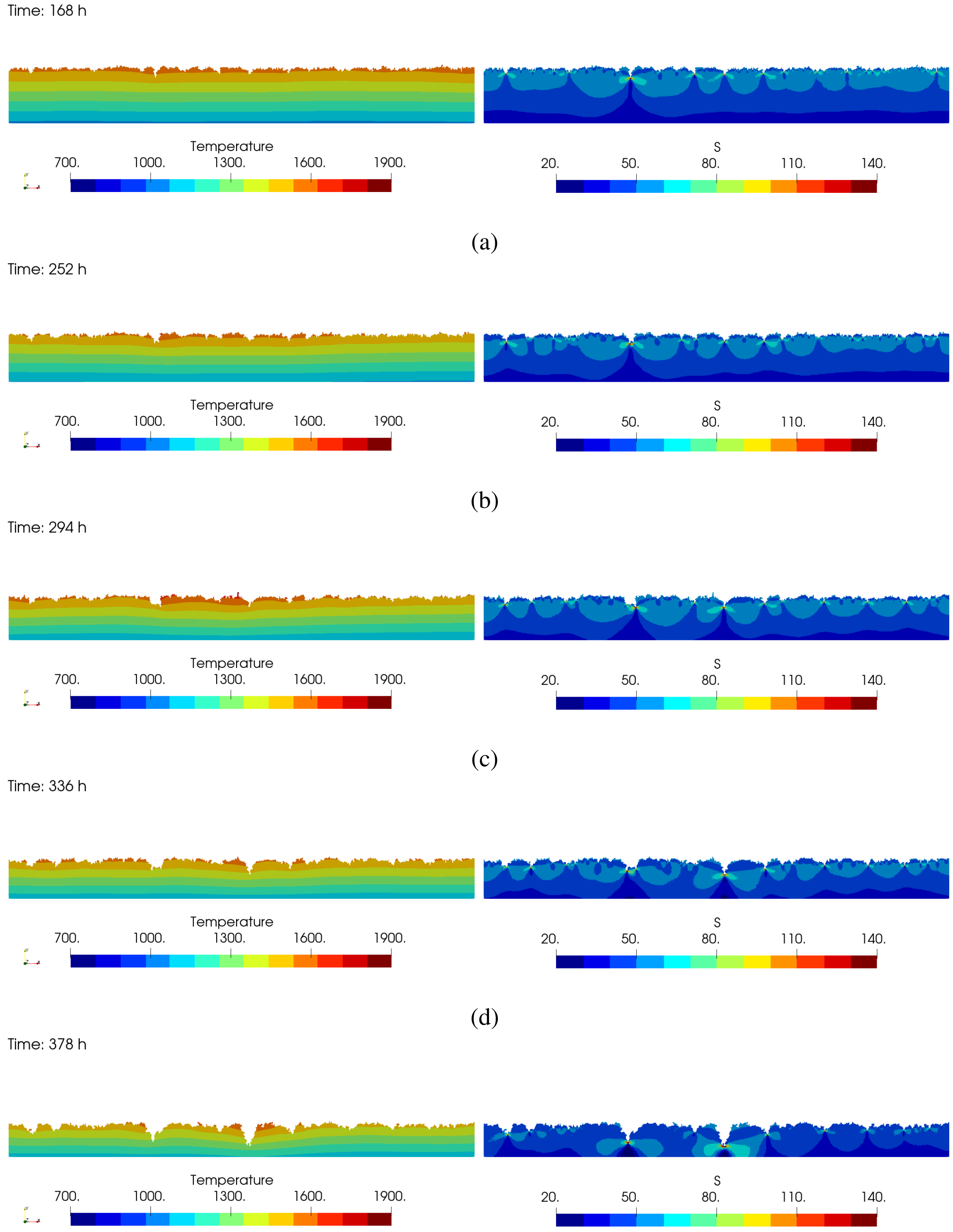

(a)

(b)

(c)

(d)

(e)

Figure 4.20: Temperature (K) and stress (S, MPa) fields for the erosion process at approximately 90 mW/mm$^2$.

are not included in this analysis because some surface points exceed the softening point temperature, and the simulations were terminated earlier. As with the case of boron nitride, we also show the comparison with two models, (i) the pure sputtering model and (ii) the sputtering with elastic material behavior.

Figure 4.21 shows the erosion rates for this range of heat flux which are in agreement with typical erosion rates for this material [23]. In this plot, we provide a linear fit model to show the trend of how the erosion rate is affected by the input power. Figure 4.22 shows typical values of stresses and temperature that are attained for this particular boundary value problem. However, as these variables depend on the geometry and boundary conditions (among others), they only provide an estimate of how the power to wall affects them. Finally, Figure 4.23 provides an assessment of how the surface features, characterized here in terms of the surface roughness and peak to valley values, are affected by the input power. It is worth noting that even though the behavior of the material seems to play a little role in the overall temperature trends and erosion rates, as shown in Figure 4.21 and Figure 4.22, it is clear that it plays a significant part in the development of features as seen that the data-driven model is bounded by the results of pure sputtering (blue) and elastic material (orange). It is then inferred that the elastic material tends to overestimate provided that there is no limiting stress values, whereas the sputtering model tends to underestimate considering the lack of material behavior. By using a homogenized material behavior with the SCL in the data-driven model (green) we are capturing the softening behavior of the material upon brittle fracture.

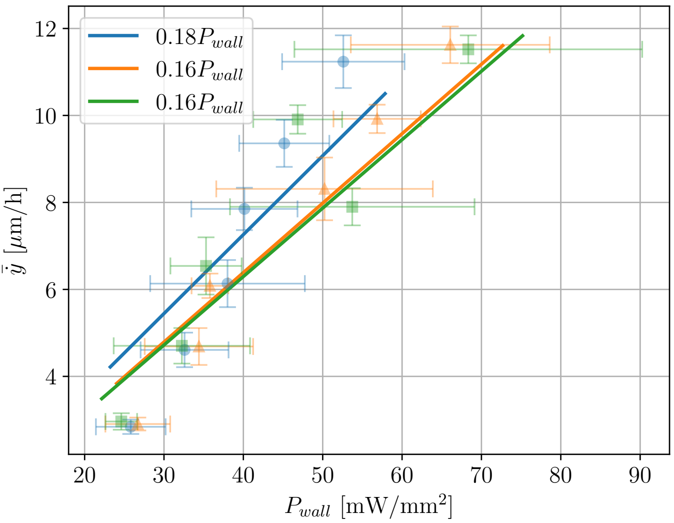

Figure 4.21: Erosion rate for fused silica as a function of applied power.

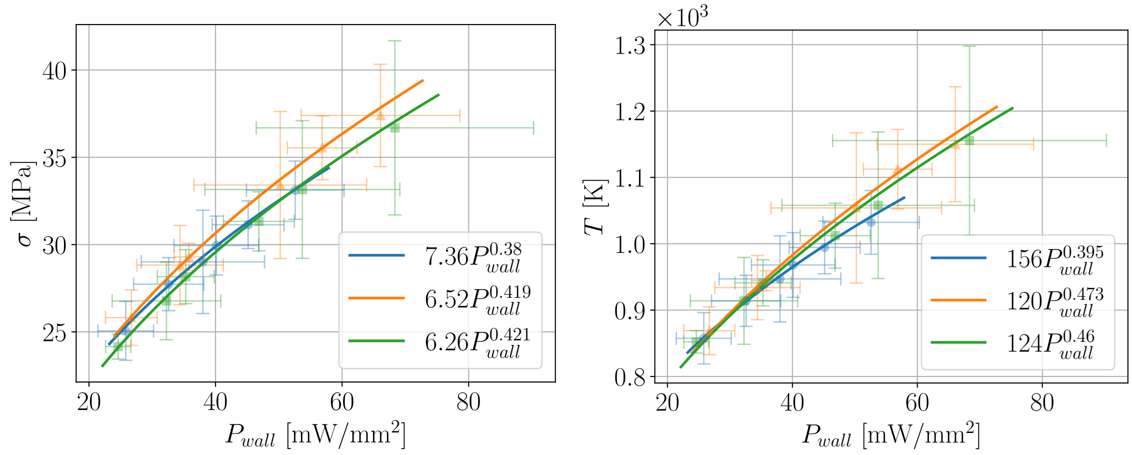

(a)

(b)

Figure 4.22: Estimated (a) stresses and (b) temperatures as a function of the heat flow to the wall at each power level for fused silica.

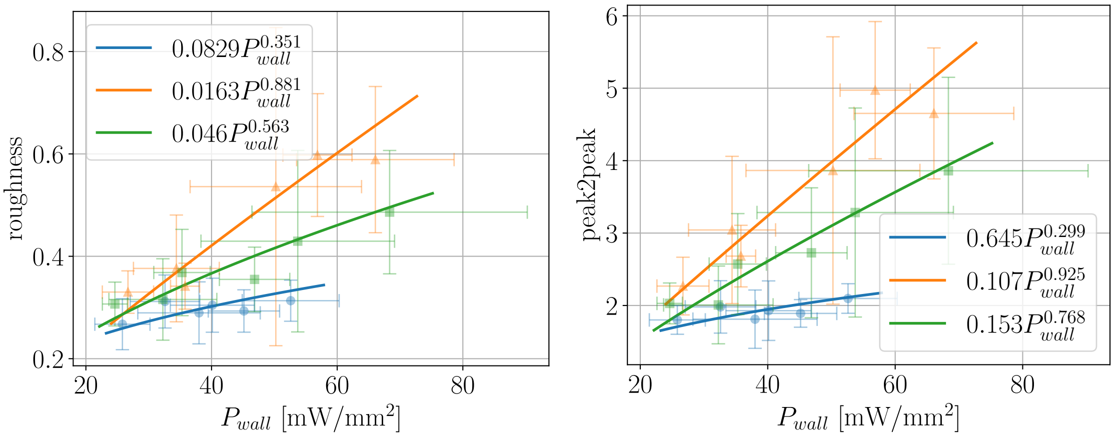

(a)

(b)

Figure 4.23: (a) Roughness and (b) peak-to-valley values, as a function of the heat flow to the wall at each power level for fused silica.

*Discussion*

Figure 4.24 shows the evolution of the roughness (a) and strain energy density (b) for qualitatively low, medium, and high power using the three different behaviors: (i) pure sputtering in blue, (ii) elastic material in orange and (iii) data-driven material in green. For each power level, ten simulations are performed (considering the probabilistic approach). Therefore, we show the statistic mean value at each time represented with solid lines and the standard deviation shown with the shaded area. It should be noted here that the elastic and data-driven material model also includes the sputtering model. From the picture, it can be inferred that when there is not enough power to the wall (ion energy) to produce significant strain energy density in the surface, the addition of a material behavior does not provide any advantage to reproduce the anomalous ridges as it can be seen in the first column of the picture. However, when the power to the wall is enough to produce higher strain energies, an unstable process is triggered. This process could be explained as follows. First, the power to the wall is enough to produce higher strain energies at some points of the surface, which become more susceptible to erosion. Once these points are eroded, generating a deeper valley, it increases the size factor (since it depends on the surface features), which in turn, it will increase the ion energy deposition to the wall; in other words, it will induce more heat flux to the wall in those areas. Naturally, this increase in the heat flux generates higher temperature gradient, thus, higher induced thermal stresses that ultimately leads to higher strain energy densities. At this point, the process becomes “unstable”, and valleys would erode faster, which can be quantified by an increase in the roughness of the surface (or equivalently from the peak-to-valley) as depicted in Figure 4.25. It can also be seen that for the data-driven model, the evolution of the roughness is bounded between the sputtering model and the elastic one, where the former tends to underestimate the formation of ridges and the latter tends to overestimate their formation. This is presumably because the data-driven model is able to capture the non-linear softening behavior of the fused silica microstructure upon brittle cracking.

### 4.3 Summary of results

As expressed in this chapter, the addition of an inelastic constitutive model that includes ceramic behavior helps explain the creation and development of surface instabilities like the anomalous ridges for long exposure operations. However, the *inelastic* model presented in section 3.3 has several limitations. For example, the orientation of cracks is unique and constant, and it does not account for shear behavior, to name a few. Because of these limitations, the DE model (*inelastic model*) fails to provide accurate representation of the microstructure under several load scenarios as it is demonstrated in section 3.4. More importantly, it restricts the predicting capabilities when there are several phenomena that happen in the microstructure level, such as ion diffusion or implantation, as it has been shown to affect the mechanical behavior, for example in other materials [41].

Therefore, in the second part of the chapter, we present a new methodology that leverages state-of-the-art machine learning techniques to homogenize the non-linear behavior of fused silica. Using the homogenized material, called Smart Constitutive Law (SCL), provides the capabilities to account for the physics that govern the microstructural behavior in

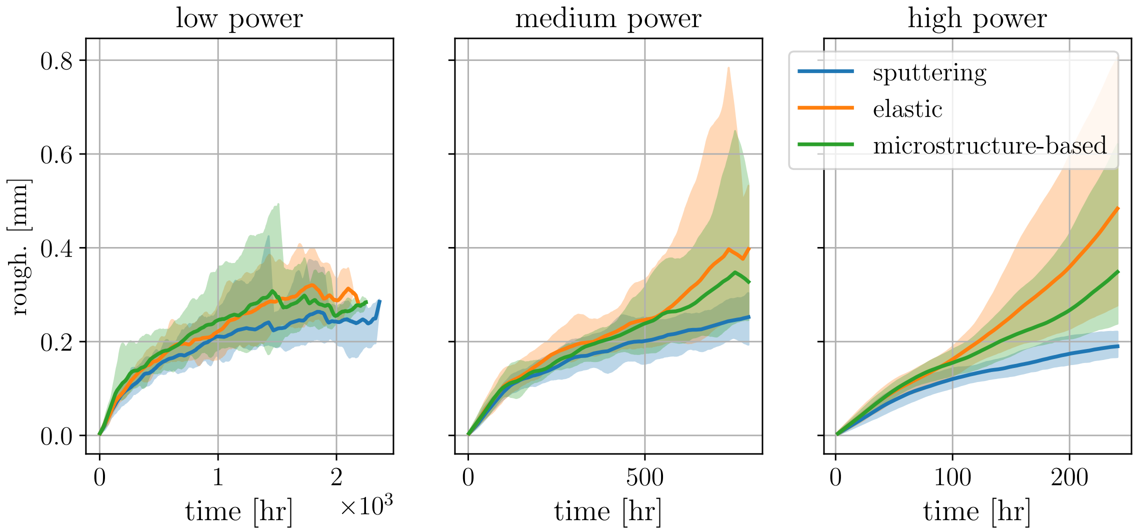

(a) Roughness

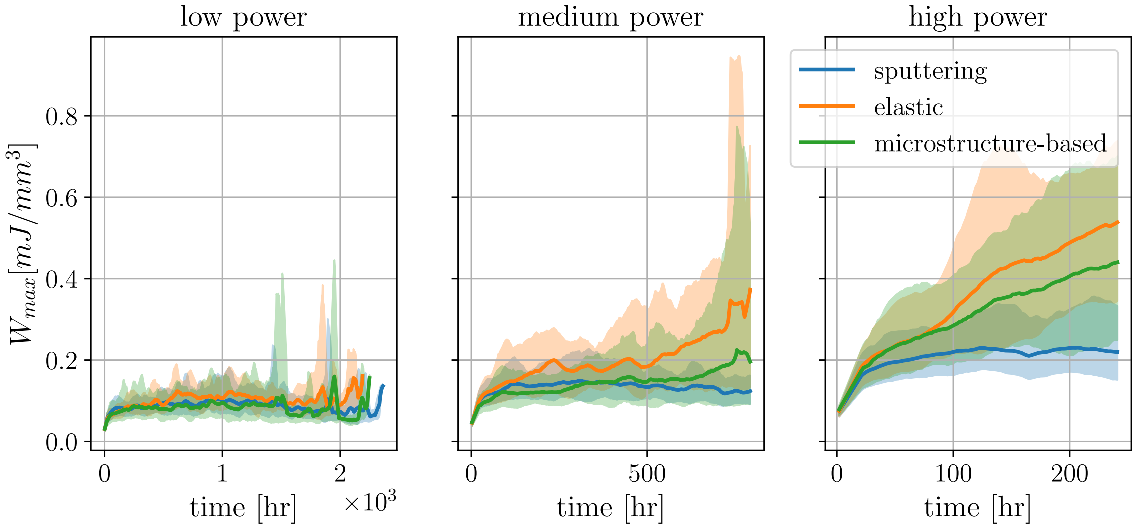

(b) Strain energy density

Figure 4.24: Roughness and strain energy density evolution for the sputtering, elastic, and data-driven model for three power levels.

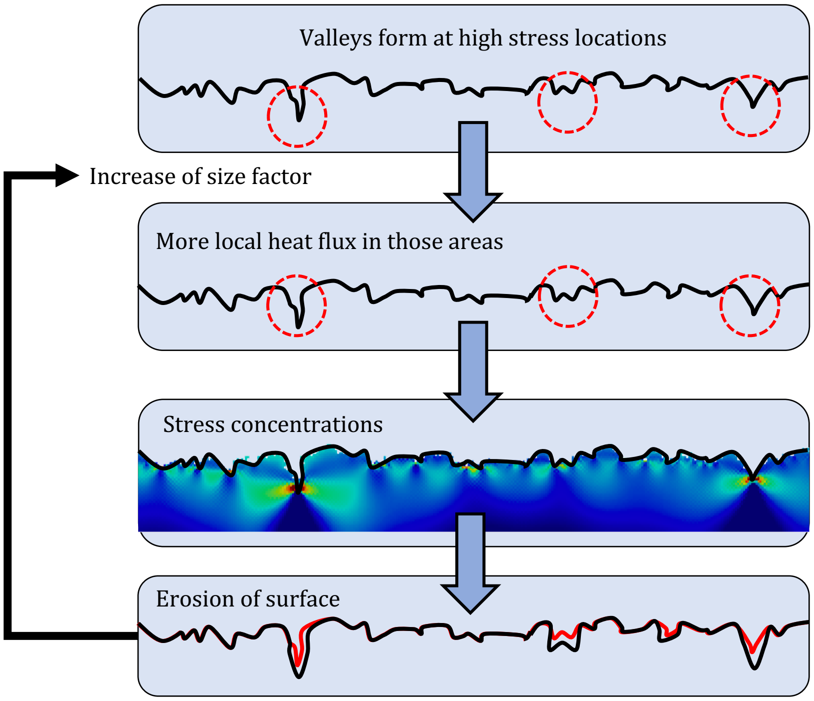
Valleys form at high stress locations
Increase of size factor
More local heat flux in those areas
Stress concentrations
Erosion of surface

Figure 4.25: Schematics of the unstable erosion process.

a macroscopic model without losing generality. It is shown how the SCL is implemented into a plasma-wall interaction model and how its behavior affects the formation of anomalous erosion ridges.

We have shown in this chapter that the material model becomes more relevant as the power incident to the wall increases. This implies that this type of plasma-materials interactions (in particular the effect on the material damage) will become critical for predicting the life of upcoming high-density electric propulsion devices. In particular, the capability to reproduce the formation and evolution of erosion ridges is relevant since the lifetime of devices is limited by the maximum recession where these valleys form, and not necessarily by the mean erosion rate as shown in Figure 4.26 for the case reproducing the mean erosion rate (sputtering model, blue) and where a microstructure-based material is accounted for (orange). As it can be seen, the effect of the erosion ridges is more important for higher power deposition to wall.

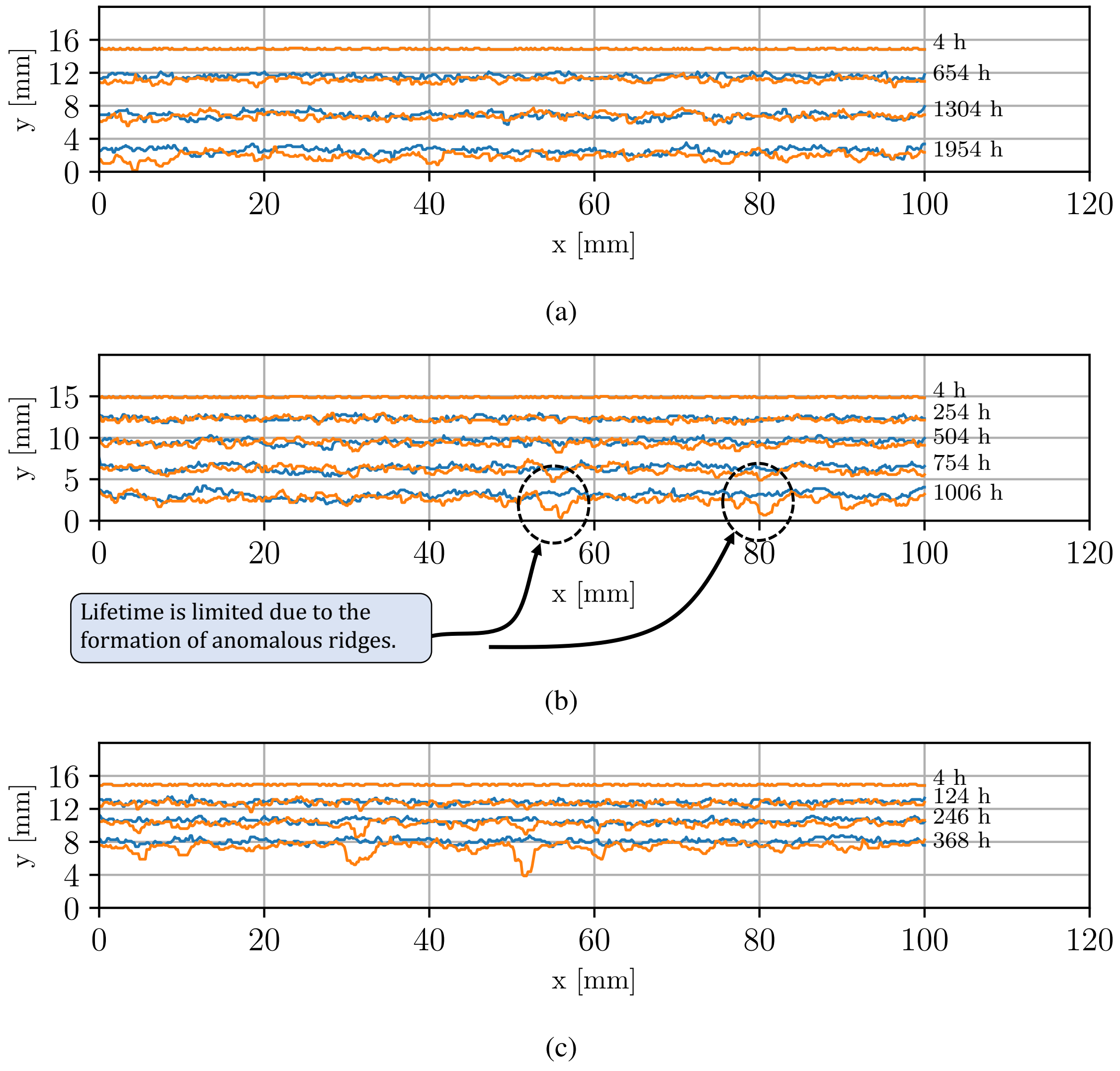

(a)

(b)

Lifetime is limited due to the formation of anomalous ridges.

(c)

Figure 4.26: Evolution and comparison of the recession of the wall for the sputtering case (blue) and the microstructure-based material (orange) where the erosion ridges would limit the lifetime of a device for (a) low, (b) medium, and (c) high powers.

# CHAPTER 5

# CONCLUSIONS

## 5.1 Summary and conclusions

This work establishes a model to better understand the erosion process of materials due to ion bombardment at the macro-scale and for a long time exposure. In chapter 2, an original interaction model between the ionized gas and the material behavior is presented. The proposed model comprises data from plasma dynamics simulations and FE analysis of the material. The coupling between the two phenomena is carried out by the definition of four novel parameters and functions: (1) a *visibility factor* that accounts for ion orientation and shadowing effects, (2) a *size factor* that accounts for the relative shape and size of the surface features with respect to a plasma parameter and a reference geometry, (3) an *energy interpolation function* to define the point-wise ion energy deposited to the walls and (4) a *probability erosion function* to quantify the susceptibility of each surface point to be eroded based on the energy deposited and the material state (damage). Furthermore, the state-of-the-art sputtering yield model is also incorporated in the calculation of erosion.

In chapter 3 we provide a description of several material models that are used in the plasma-wall interaction model. In particular, we present a novel method of homogenization using machine learning (ML) with the objective to develop a general framework able to reproduce the effective nonlinear and history-dependent behavior of complex microstructures. The method only needs strain and stress histories on an RVE to create a surrogate constitutive law named *Smart Constitutive Law* (SCL) without any extra assumptions regarding the underlying or emergent material response at the microstructure or homogenized scales, respectively. These material models are then used to calculate the stresses in the thermo-mechanical part of the plasma-wall interaction.

The plasma-wall interaction model is then evaluated for two different ceramics. In the first part of chapter 4 we provide the results of the erosion process for boron nitride. In order to demonstrate how the material behavior affects the erosion process, we study three different cases. The first one only uses sputtering yield to calculate the erosion (*sputtering model*). The second one combines the sputtering model with an elastic material (*elastic model*) and the third one, in which the material model is enhanced to account for microstructure mechanics (DE material model or *inelastic model*). It is shown that in the models in which the material is accounted for (elastic and inelastic models) the overall solution can reproduce the anomalous ridges that appear after long exposure, whereas the model of pure sputtering only provides a good estimation of the mean erosion. This represents a great improvement in the erosion process calculation capabilities. In addition, a statistical analysis of several simulations at different input power levels suggests that the material behavior plays a fundamental role in the formation and evolution of such unstable features.

In the second part of chapter 4 we use the SCL derived in section 3.5 to analyze the behavior of fused silica since it can represent the effective softening behavior of the microstructure upon brittle fracture and since it enables the addition of physics phenomena that developed in the microscale. As in boron nitride, we demonstrate how the SCL is able to reproduce erosion ridges which ultimately would help in the prediction capabilities of future devices. Based on the results, we observe that when the power deposition to the wall is sufficient to produce high strain energies at some points on the surface, these points become more susceptible to erosion. Upon being eroded, deeper valleys can form, which increases the size factor, which in turn increases the ion energy deposition to the wall. In other words, it will induce more heat flux in those areas. This higher heat flux increases the local temperature and therefore, the thermal stresses and strain energies. This process becomes “unstable”, and valleys would erode faster leading to the development of anomalous erosion. Therefore, we conclude that the formation and development of anomalous erosion ridges is driven primarily by the material behavior. This represents a very important contribution since this is the first time to our knowledge that a model is able to reproduce this erosion mechanism.

We also conclude that the material model becomes more relevant as the power incident to the wall increases. This implies that this type of plasma-materials interactions (in particular the effect on the material damage) will become critical for predicting the life of upcoming high-density electric propulsion devices.

## 5.2 Contributions

The research presented in this work provides the following contributions to the state of the art.

1. A novel plasma-wall interaction model that predicts the erosion features at the macro-scale that appear in the material after long exposure to plasma environments. This has not been addressed by any model up to date and represents an improvement in the erosion process predicting capabilities. The model comprises several original characteristics:

    - A *visibility factor*, accounts for shadowing effects and ion orientation (described in subsection 2.2.2).
    - A *size factor*, that accounts for the relationship between the surface features and geometric and plasma parameters (described in subsection 2.2.2).
    - The *ion energy interpolation scheme* to determine the ion energy deposition at each point of the surface considering data from a plasma dynamics simulation (described in subsection 2.2.2).
    - The *probabilistic model of erosion* presented in subsection 2.2.4 combines the sputtering model and the material behavior to determine the susceptibility of each surface point of being eroded and,

  - A continuum thermo-elastic model is described in section 2.3.

2. Considering the underlying physics that develop at the microscale, this work also develops a novel methodology to obtain the effective properties of complex microstructures that exhibit non-linear and path-dependent behavior through machine learning as presented in chapter 3. This new technique is shown to be very efficient without losing accuracy in comparison with concurrent multiscale modeling. This contribution also includes,

    - Development of an in-house FE solver that is able to solve static and dynamic problems.
    - Implementation of the SCL into the FE solver.

3. A mechanism that helps explain the formation of anomalous ridges and how the material behavior plays a fundamental role in the formation of such erosion patterns. More importantly, it demonstrates how the lifetime is limited by the maximum recession at the points where these erosion ridges form, and not necessarily by the mean erosion rate.

### 5.3 Future work

There are several lines of future work that could enhance the erosion process prediction capabilities. From the numerical point of view, the study of the ion beam orientation with respect to the specimen could lead to approximating the solution of the erosion process and patterns that form in an operating HET. Once this is investigated, the model could be adjusted to a 2D geometry of a HET channel to predict the lifetime. Furthermore, another enhancement could be obtained by coupling a “real-time” plasma dynamics, therefore, reducing the need for tuning geometric parameters. Secondly, an extension to 3D domain is a very interesting line of research since in this work, we focused on a 2D plane strain problem due to the limitations of computer capabilities. The addition of a third dimension would allow us to investigate the preferred orientation of ripples as seen in HETs.

From the material homogenization point of view, a natural extension of this work is the study of the effect of considering ion implantation and diffusion in the microstructure since that will affect the overall non-linear behavior of the homogenized material. In this same line of investigation, another study could be carried out to account for how the distribution of microcracks, as well as their density, affects the overall behavior of the microstructure. Moreover, a different damage parameter (other than the strain energy density) could be investigated that could reflect the local state of the microstructure, for example, a damage parameter indicating the degradation of the cohesive response.

From the experimental point of view, it would be beneficial to contrast the plasma-wall interaction model with the SCL material used for fused silica with experimental data for samples exposed to plasma for long periods of time. This will enable a fine tune of the parameters that govern the erosion process.

# Appendices

# APPENDIX A

# STRAIN ENERGY DENSITY AT FAILURE

The strain energy at failure $w_{\text{max}}$, defined in subsubsection 4.1.1 using the boundary conditions Figure 4.1 is obtained as follows.

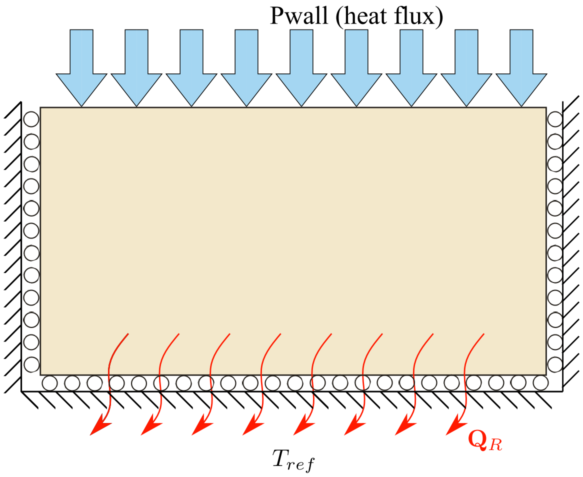

Figure A.1: Schematics for the thermal and mechanical boundary conditions of the thermo-elastic model.

First consider the thermal strains given by,

$$\epsilon_{ij}^{t} = \alpha \Delta T \tag{A.1}$$

where $\Delta T = T - T_{ref}$ is the difference between the specimen temperature and a reference temperature and $\alpha$ a thermal expansion coefficient. The mechanical strains then follow,

$$\epsilon_{ij}^{m} = \epsilon_{ij} - \epsilon_{ij}^{t} \tag{A.2}$$

Given the boundary conditions as illustrated in Figure 4.1, $\epsilon_{11} = \epsilon_{33} = 0$. The component $\epsilon_{11}$ due to the boundary conditions, and $\epsilon_{33} = 0$ due the plane strain condition of the problem. The mechanical strain tensor is then,

$$\begin{aligned}\epsilon_{11}^{m} &= -\alpha\Delta T\\ \epsilon_{22}^{m} &= \epsilon_{22} - \alpha\Delta T\\ \epsilon_{33}^{m} &= -\alpha\Delta T\end{aligned} \tag{A.3}$$

and the volumetric strain is

$$\epsilon_{vol}^{m} = \epsilon_{11}^{m} + \epsilon_{22}^{m} + \epsilon_{33}^{m} = \epsilon_{22} - 3\alpha\Delta T \tag{A.4}$$

The stress tensor in linear elasticity is given by,

$$\sigma_{ij} = \lambda\epsilon_{vol}^{m}\delta_{ij} + 2\mu\epsilon_{ij}^{m} \tag{A.5}$$

where $\lambda$ and $\mu$ are the Lame constants, and $\delta_{ij}$ is the Kronecker delta operator. Thus, the stress tensor is

$$\begin{aligned}\sigma_{11} &= \lambda\epsilon_{vol}^{m} + 2\mu\epsilon_{11}^{m}\\ \sigma_{22} &= \lambda\epsilon_{vol}^{m} + 2\mu\epsilon_{22}^{m}\\ \sigma_{33} &= \lambda\epsilon_{vol}^{m} + 2\mu\epsilon_{33}^{m}\end{aligned} \tag{A.6}$$

and the shear components are all zero, $\sigma_{12} = \sigma_{23} = \sigma_{31} = 0$ (and their corresponding symmetric parts). Equation A.6 can be re-written by plugging Equation A.3 and Equation A.4,

$$\begin{aligned}\sigma_{11} &= \lambda\epsilon_{22}^{m} - (3\lambda + 2\mu)\alpha\Delta T\\ \sigma_{22} &= (\lambda + 2\mu)\epsilon_{22}^{m} - (3\lambda + 2\mu)\alpha\Delta T\\ \sigma_{33} &= \lambda\epsilon_{22}^{m} - (3\lambda + 2\mu)\alpha\Delta T\end{aligned} \tag{A.7}$$

As it can be seen from the figure, the specimen can freely expand in the vertical direction, thus $\sigma_{22} = 0$, using this condition, the mechanical strain in the vertical direction can be found from Equation A.7,

$$\epsilon_{22} = \frac{3\lambda + 2\mu}{\lambda + 2\mu}\alpha\Delta T \tag{A.8}$$

Replacing Equation A.8 into Equation A.7 we obtain the components on the horizontal axis $\sigma_{11}$ and out of plane $\sigma_{33}$, which are equal,

$$\begin{aligned}\sigma_{11} = \sigma_{33} &= -\frac{2\mu}{\lambda + 2\mu}(3\lambda + 2\mu)\alpha\Delta T \\ &= \epsilon_{Th}\alpha\Delta T\end{aligned} \tag{A.9}$$

where $\epsilon_{Th} = -\frac{2\mu}{\lambda+2\mu}(3\lambda + 2\mu)$ for simplicity. Therefore, the change in temperature to produce failure due to the maximum stress failure criteria $\sigma_{11} = \sigma_C$ (note that $\sigma_{11}$ is compressive and $\sigma_C$ is the compressive strength of the material). For simplicity,

$$\Delta T = \frac{\sigma_C}{\alpha\epsilon_{Th}} \tag{A.10}$$

The strain energy density is[1],

$$\begin{aligned}w = \frac{1}{2}\sigma_{ij}\epsilon_{ij} &= \frac{1}{2}(\sigma_{11}\epsilon^m_{11} + \sigma_{22}\epsilon^m_{22} + \sigma_{33}\epsilon^m_{33}) \\ &= \sigma_{11}\epsilon^m_{11}\end{aligned} \tag{A.11}$$

Finally, the strain energy density when the material reaches the failure criteria is obtained by using Equation A.9 and Equation A.10 in Equation A.11.

---

[1] Note: we follow Einstein notation in which repeated indices represent a summation

$$\begin{aligned} w_{\text{max}} &= \epsilon_{Th}\alpha\Delta T(-\alpha\Delta T) \\ &= \frac{\sigma_C^2}{-\epsilon_{Th}} \\ &= \frac{\lambda + 2\mu}{2\mu\,(3\lambda + 2\mu)}\sigma_C^2 \end{aligned} \tag{A.12}$$

# APPENDIX B

# MICROCRACKS COEFFICIENTS

The nonlinear functions of the damage $D$ and friction $\mu$ used in section 3.3 are;

$$A = c_1(c_2A_3 - c_2A_1 + c_3) \tag{B.1}$$

$$B = \frac{c_1}{\sqrt{3}}(c_2A_3 + c_2A_1 + c_3) \tag{B.2}$$

$$C = A + \gamma\sqrt{\alpha\left(\frac{D}{D_0}\right)^{1/3}} \tag{B.3}$$

$$F = \sqrt{\left(\frac{B^2C^2}{C^2 - A^2}\right)} \tag{B.4}$$

with

$$c_1 = \frac{1}{\pi^2\alpha^{3/2}\left[(D/D_0)^{1/3} - 1 + (\beta/\alpha)\right]^{3/2}} \tag{B.5}$$

$$c_2 = 1 + 2\left[\left(\frac{D}{D_0}\right)^{1/3} - 1\right]^2\left(\frac{D_0^{2/3}}{1 - D^{2/3}}\right) \tag{B.6}$$

$$c_3 = 2\alpha^2\pi^2\left[\left(\frac{D}{D_0}\right)^{1/3} - 1\right]^2 \tag{B.7}$$

and

$$A_1 = \pi\sqrt{\frac{\beta}{3}}\left[(1 + \mu^2)^{1/2} - \mu\right] \tag{B.8}$$

$$A_3 = A_1\left[\frac{(1 + \mu^2)^{1/2} + \mu}{(1 + \mu^2)^{1/2} - \mu}\right] \tag{B.9}$$

where $\beta = 0.1$ is a parameter to convert the two-dimensional solution into a three-dimensional employed in [35, 34, 36], and $\gamma$ is used to match the tensile data.

# REFERENCES

[1] D. M. Goebel and I. Katz, *Fundamentals of Electric Propulsion: Ion and Hall Thrusters*. 2008, ISBN: 9780470429273.

[2] N. P. Brown and M. L. Walker, *Review of plasma-induced hall thruster erosion*, 2020.

[3] N. Gascon, M. Dudeck, and S. Barral, “Wall material effects in stationary plasma thrusters. I. Parametric studies of an SPT-100,” *Physics of Plasmas*, 2003.

[4] C. E. Garner, J. R. Brophy, J. E. Polk, and L. C. Pless, “A 5,730-Hr cyclic endurance test of the SPT-100,” in *31st Joint Propulsion Conference and Exhibit*, 1995, ISBN: 9780000000002.

[5] M. Lyszyk, E. Klinger, O. Sécheresse, J. P. Bugeat, D. Valentian, A. Cadiou, T. Beltan, and C. Gelas, “Qualification status of the pps 1350 plasma thruster,” in *35th Joint Propulsion Conference and Exhibit*, 1999.

[6] K. De Grys, A. Mathers, B. Welander, and V. Khayms, “Demonstration of 10,400 hours of operation on a 4.5 kW qualification model Hall thruster,” in *46th AIAA/ASME/SAE/ASEE Joint Propulsion Conference and Exhibit*, 2010.

[7] S. Zurbach, O. B. Duchemin, V. Vial, F. Marchandise, N. Cornu, and N. Arcis, “Qualification of the pps-1350 hall thruster at 2.5 kw,” in *49th AIAA/ASME/SAE/ASEE Joint Propulsion Conference*, 2013, ISBN: 9781624102226.

[8] P. Sigmund, “A mechanism of surface micro-roughening by ion bombardment,” *Journal of Materials Science*, 1973.

[9] R. M. Bradley and J. M. E. Harper, “Theory of ripple topography induced by ion bombardment,” *Journal of Vacuum Science & Technology A: Vacuum, Surfaces, and Films*, 1988.

[10] Y. Yamamura and H. Tawara, “Energy dependence of ion-induced sputtering yields from monatomic solids at normal incidence,” *Atomic Data and Nuclear Data Tables*, 1996.

[11] Y. Garnier, V. Viel, J.-F. Roussel, and J. Bernard, “Low-energy xenon ion sputtering of ceramics investigated for stationary plasma thrusters,” *Journal of Vacuum Science & Technology A: Vacuum, Surfaces, and Films*, 1999.

[12] A. P. Yalin, B. Rubin, S. R. Domingue, Z. Glueckert, and J. D. Williams, “Differential sputter yields of boron nitride, quartz, and kapton due to low energy Xe+ bom-

bardment," in *Collection of Technical Papers - 43rd AIAA/ASME/SAE/ASEE Joint Propulsion Conference*, 2007, ISBN: 1563479036.

[13] P. Y. Peterson and D. H. Manzella, "Investigation of the erosion characteristics of a laboratory Hall thruster," in *39th AIAA/ASME/SAE/ASEE Joint Propulsion Conference and Exhibit*, 2003, ISBN: 9781624100987.

[14] J. M. Fife and M. Martinez-Sanchez, *Hybric-PIC Modeling and Electrostatic Probe Survey of Hall Thrusters*, 1998.

[15] M. Gamero-castaño and I. Katz, "Estimation of Hall Thruster Erosion Using HPHall," in *Proceedings of the International Electric Propulsion Conference 2005 (IEPC05)*, 2005.

[16] S. Mazouffre, F. Duhois, L. Albarède, D. Pagnon, M. Touzeau, and M. Dudeck, "Plasma induced erosion phenomena in a hall thruster," in *RAST 2003 - Proceedings of International Conference on Recent Advances in Space Technologies*, 2003, ISBN: 0780381424.

[17] V. Kim, "Main physical features and processes determining the performance of stationary plasma thrusters," *Journal of Propulsion and Power*, 1998.

[18] S. Mazouffre, K. Dannenmayer, and J. Pérez-Luna, "Examination of plasma-wall interactions in Hall effect thrusters by means of calibrated thermal imaging," *Journal of Applied Physics*, 2007.

[19] R. A. Martinez, H. Dao, and M. L. R. Walker, "Power Deposition into the Discharge Channel of a Hall Effect Thruster," *Journal of Propulsion and Power*, 2013.

[20] T. Burton, A. M. Schinder, G. Capuano, J. J. Rimoli, M. L. Walker, and G. B. Thompson, "Plasma-induced erosion on ceramic wall structures in hall-effect thrusters," *Journal of Propulsion and Power*, 2014.

[21] A. M. Schinder, M. Walker, and J. J. Rimoli, "Three-dimensional model for erosion of a hall-effect thruster discharge channel wall," in *Journal of Propulsion and Power*, 2014.

[22] N. P. Brown, C. B. Whittaker, J. J. Rimoli, W. J. Ready, and M. L. Walker, "Formation and impact of microcracks in plasma erosion of m26 boron nitride," *Journal of Propulsion and Power*, 2021.

[23] A. M. Schinder, J. J. Rimoli, and M. L. Walker, "Investigation of plasma material erosion under mechanical stress," in *Journal of Propulsion and Power*, 2017.

[24] K. S. Kim, J. A. Hurtado, and H. Tan, “Evolution of a surface-roughness spectrum caused by stress in nanometer-scale chemical etching,” *Physical Review Letters*, 1999.

[25] R. Cuerno and A. L. Barabási, “Dynamic scaling of ion-sputtered surfaces,” *Physical Review Letters*, 1995.

[26] P. F. Alkemade, “Propulsion of ripples on glass by ion bombardment,” *Physical Review Letters*, 2006.

[27] W. L. Chan and E. Chason, “Making waves: Kinetic processes controlling surface evolution during low energy ion sputtering,” *Journal of Applied Physics*, 2007.

[28] H. J. Logarzo, G. Capuano, and J. J. Rimoli, “Smart constitutive laws: Inelastic homogenization through machine learning,” *Computer Methods in Applied Mechanics and Engineering*, 2021.

[29] I. Schweigert, T. S. Burton, G. B. Thompson, S. Langendorf, M. L. Walker, and M. Keidar, “Plasma interaction with emmissive surface with Debye-scale grooves,” *Plasma Sources Science and Technology*, 2018.

[30] P. Virtanen, R. Gommers, T. E. Oliphant, M. Haberland, T. Reddy, D. Cournapeau, E. Burovski, P. Peterson, W. Weckesser, J. Bright, S. J. van der Walt, M. Brett, J. Wilson, K. J. Millman, N. Mayorov, A. R. J. Nelson, E. Jones, R. Kern, E. Larson, C. J. Carey, İ. Polat, Y. Feng, E. W. Moore, J. VanderPlas, D. Laxalde, J. Perktold, R. Cimrman, I. Henriksen, E. A. Quintero, C. R. Harris, A. M. Archibald, A. H. Ribeiro, F. Pedregosa, and P. van Mulbregt, “SciPy 1.0: fundamental algorithms for scientific computing in Python,” *Nature Methods*, vol. 17, no. 3, pp. 261–272, Mar. 2020.

[31] L. Devroye and L. Devroye, “General Principles in Random Variate Generation,” in *Non-Uniform Random Variate Generation*, 1986.

[32] Richard J. Rossi, *Mathematical Statistics: An Introduction to Likelihood Based Inference*. Wiley, 2018, ISBN: 978-1-118-77104-4.

[33] K. Bathe, *Finite Element Procedures*, 2014. arXiv: arXiv:1011.1669v3.

[34] V. S. Deshpande and A. G. Evans, “Inelastic deformation and energy dissipation in ceramics: A mechanism-based constitutive model,” *Journal of the Mechanics and Physics of Solids*, 2008.

[35] M. F. Ashby and C. G. Sammis, “The damage mechanics of brittle solids in compression,” *Pure and Applied Geophysics PAGEOPH*, 1990.

[36] V. S. Deshpande, E. A. N. Gamble, B. G. Compton, R. M. McMeeking, A. G. Evans, and F. W. Zok, "A constitutive description of the inelastic response of ceramics," *Journal of the American Ceramic Society*, 2011.

[37] H. S. Bhat, A. J. Rosakis, and C. G. Sammis, "A Micromechanics Based Constitutive Model for Brittle Failure at High Strain Rates," *Journal of Applied Mechanics*, 2012.

[38] R. Hill and J. R. Rice, "Elastic Potentials and the Structure of Inelastic Constitutive Laws," *SIAM Journal on Applied Mathematics*, 1973.

[39] J. Rice, "Continuum mechanics and thermodynamics of plasticity in relation to microscale deformation mechanisms," *Constitutive Equations in Plasticity. Massachusetts Institute of Technology Press, Cambridge. 1975, 23-79*, 1975.

[40] K. A. Hart and J. J. Rimoli, "MicroStructPy: A statistical microstructure mesh generator in Python," *SoftwareX*, vol. 12, 2020.

[41] J. J. Rimoli and M. Ortiz, "A three-dimensional multiscale model of intergranular hydrogen-assisted cracking," *Philosophical Magazine*, vol. 90, no. 21, 2010.

[42] Dassault Systèmes Simulia, A. Fallis, and D. Techniques, "ABAQUS documentation," *Abaqus 6.12*, 2013. arXiv: arXiv:1011.1669v3.

[43] K. Park and G. H. Paulino, "Cohesive zone models: A critical review of traction-separation relationships across fracture surfaces," *Applied Mechanics Reviews*, vol. 64, no. 6, 2011.

[44] M. Ortiz and A. Pandolfi, "Finite-deformation irreversible cohesive elements for three-dimensional crack-propagation analysis," *International Journal for Numerical Methods in Engineering*, vol. 44, no. 9, 1999.

[45] G. Capuano and J. J. Rimoli, "Smart finite elements: A novel machine learning application," *Computer Methods in Applied Mechanics and Engineering*, 2019.

[46] T. J. Hughes, G. R. Feijóo, L. Mazzei, and J. B. Quincy, "The variational multiscale method - A paradigm for computational mechanics," *Computer Methods in Applied Mechanics and Engineering*, 1998.

[47] A. L. Gurson, "Continuum Theory of Ductile Rupture by Void Nucleation and Growth: Part I—Yield Criteria and Flow Rules for Porous Ductile Media," *Journal of Engineering Materials and Technology*, 1977.

[48] F. Chollet *et al.* (2015). "Keras."

[49] G. Capuano, “Smart Finite Elements: An application of Machine Learning to reduced-order modeling of multi-scale problems,” Ph.D. dissertation, Georgia Institute of Technology, 2019.

[50] C. E. Rasmussen, *Gaussian processes for machine learning.* 2006, ISBN: 978-0-262-18253-9. arXiv: 026218253X.

[51] S. Hochreiter and J. Schmidhuber, “Long Short-Term Memory,” *Neural Computation*, 1997.

[52] M. C. Mozer, “A Focused Backpropagation Algorithm for Temporal Pattern Recognition,” *Complex Systems*, 1989.

[53] S. J. Pan and Q. Yang, *A survey on transfer learning*, 2010.

[54] K. Weiss, T. M. Khoshgoftaar, and D. D. Wang, “A survey of transfer learning,” *Journal of Big Data*, vol. 3, no. 1, 2016.

[55] F. Zhuang, Z. Qi, K. Duan, D. Xi, Y. Zhu, H. Zhu, H. Xiong, and Q. He, *A Comprehensive Survey on Transfer Learning*, 2021.

[56] St. Gobain Ceramic Materials, *COMBAT Boron Nitride Solids Products Datasheet*.

[57] M. Stéphane, L. Jaime Pérez, G. Damien, E. Patrick, and D. Michel, “an Infrared Thermography Study on the Thermal Load Experienced By a High Power Hall Thruster,” *29th International Electric Propulsion Conference*, 2005.

[58] S. Cheng, “Modeling of Hall thruster lifetime and erosion mechanisms,” Ph.D. dissertation, Massachusetts Institute of Technology, 2007.

[59] J. T. Yim and I. D. Boyd, “Computational Modeling of Hall Thruster Channel Wall Erosion,” Ph.D. dissertation, 2008.

[60] S. Mazouffre, K. Dannenmayer, and C. Blank, “Impact of discharge voltage on wall-losses in a Hall thruster,” *Physics of Plasmas*, vol. 18, no. 6, 2011.

[61] A. Lipp, K. A. Schwetz, and K. Hunold, “Hexagonal boron nitride: Fabrication, properties and applications,” *Journal of the European Ceramic Society*, vol. 5, no. 1, 1989.

[62] L. Vel, G. Demazeau, and J. Etourneau, “Cubic boron nitride: synthesis, physicochemical properties and applications,” *Materials Science and Engineering B*, vol. 10, no. 2, 1991.

[63] A. M. Schinder, “Investigation of Hall Effect Thruster channel wall erosion mechanisms,” Ph.D. dissertation, Georgia Institute of Technology, 2016, p. 175.

[64] P. E. Miller, T. I. Suratwala, L. L. Wong, M. D. Feit, J. A. Menapace, P. J. Davis, and R. A. Steele, “The distribution of subsurface damage in fused silica,” in *Laser-Induced Damage in Optical Materials: 2005*, vol. 5991, 2005.

[65] Technical Glass, *Fused Silica data sheet*.

[66] Azo Materials, *Fused Silica data sheet*.